Design, Analysis and Experiments on Micro-switches for Optical Applications

Jun Li

A Thesis

in

The Department

of

Electrical and Computer Engineering

Presented in Partial Fulfillment of the Requirements
for the Degree of Master of Applied Science at
Concordia University
Montreal, Quebec, Canada

December 2003

@ Jun Li, 2003

National Library
of Canada

Acquisitions and
Bibliographic Services

395 Wellington Street
Ottawa ON K1A 0N4
Canada

Bibliothèque nationale
du Canada

Acquisisitons et
services bibliographiques

395, rue Wellington
Ottawa ON K1A 0N4
Canada

Your file Votre référence
ISBN: 0-612-91064-4
Our file Notre référence
ISBN: 0-612-91064-4

The author has granted a non-exclusive licence allowing the National Library of Canada to reproduce, loan, distribute or sell copies of this thesis in microform, paper or electronic formats.

L'auteur a accordé une licence non exclusive permettant à la Bibliothèque nationale du Canada de reproduire, prêter, distribuer ou vendre des copies de cette thèse sous la forme de microfiche/film, de reproduction sur papier ou sur format électronique.

The author retains ownership of the copyright in this thesis. Neither the thesis nor substantial extracts from it may be printed or otherwise reproduced without the author's permission.

L'auteur conserve la propriété du droit d'auteur qui protège cette thèse. Ni la thèse ni des extraits substantiels de celle-ci ne doivent être imprimés ou aturement reproduits sans son autorisation.

In compliance with the Canadian Privacy Act some supporting forms may have been removed from this dissertation.

Conformément à la loi canadienne sur la protection de la vie privée, quelques formulaires secondaires ont été enlevés de ce manuscrit.

While these forms may be included in the document page count, their removal does not represent any loss of content from the dissertation.

Bien que ces formulaires aient inclus dans la pagination, il n'y aura aucun contenu manquant.

Canada

ABSTRACT

Design, Analysis and Experiments on Micro-Switches for Optical Applications

Jun Li

Micro electro mechanical system (MEMS) technology has shown its bright future in many fields, especially in optical communication fields. Because of its inherent advantages such as batch fabrication technique and small size, MEMS is becoming the dominant technology in optical crossconnect switches.

This thesis demonstrated the in-plane electro-thermally actuated uni-directional and novel bi-directional micro-switch prototypes. The novel bi-directional switches, which take the advantage of the features of CMOS technology, with the ability to bend in two opposite directions and to integrate with control circuits, have been fabricated by commercial CMOS technology. These uni-directional micro-switches have been realized by both MUMPs® technology and CMOS technology to characterize the devices performances.

Analytical models based on the specific technologies and finite element model (FEM) analysis were carried out to predict performances of switches with geometry design variations and compared with experimental results. Some interesting polysilicon material properties related phenomena, such as back bending and polysilicon resistance variation during heating and cooling cycles, have been found during experiments. This fundamental study about polysilicon material properties at high temperature in this work provides a reference and guidance for design and operation of these thermally actuated polysilicon devices.

ACKNOWLEDGMENTS

I would like to sincerely thank my supervisors, Dr. Mojtaba Kahrizi and Dr. Leslie M. Landsberger, for all they have done for me. Their support, knowledge, advice, patience and troubleshooting skills made my research achievement possible.

Many thanks, also, to all the people in our research lab, both past and present. Their friendship, support and encouragement made my life at Concordia more colorful and enjoyable.

I would like to express my deepest appreciation to my family, to my parents and parents-in-law, for their unwavering love and support. To my wife and my lovely daughter for sticking with me, and for their love. Their endless support and encouragement made all of this possible.

Thanks to the Almighty God Who is light to my path, and always.

TABLE OF CONTENTS

LIST OF FIGURES

LIST OF TABLES

Chapter 1

Introduction

1.1 Motivation

The explosive growth of data traffic such as Internet has produced a pressing need for large capacity communication networks. Over the past several years, great strides have been made in bringing the research areas of fiber optics and MEMS to the forefront of emerging technologies. More recently, there has been a push towards the integration of these two technologies, namely optical-MEMS or MOEMS. This, with continuing trends towards miniaturization, has contributed towards significant technological advancements in a wide range of industries including optoelectronics, medical devices and military applications.

The creation of functionally reliable optical switches and their required components has emerged as a leading motivator for realistic adaptation of micro-optical interconnects and the use of MEMS-technologies in optical systems and subsystems. However, in order for such efforts to be realized on a system level, the MEMS based components for these switches must be fully identified and subsequently characterized. In order to characterize these components, several key issues must be identified, modeled, and MEMS structures must be designed, fabricated and tested in order to quantify these issues.

1.2 Literature Review

The first impressive review of the application of silicon as mechanical material, more than electronic material, was published by Kurt Petersen in 1982 [1]. Almost at the same

time, Howe [2] first proved the evolution of a very useful method to build micromechanical elements using technologies that were developed first to build microelectronic devices for integrated circuits in seminal work done in 1982. Howe demonstrated techniques to fabricate micro-beams from polycrystalline silicon (polysilicon) films. With the encouragement of this demonstration, Howe built the first prototype polysilicon MEMS, a chemical vapor sensor which was a fully integrated micromechanical and microelectronic system [3]. With the development of micromachining techniques, many complex devices have been produced and some of them are already commercialized. An impressive example of commercial MEMS that makes use of surface micromachining to build a fully integrated accelerometer is the AD-XL50 microaccelerometer produced by Analog Devices Inc. for use in automobile airbag deployment systems [4].

The impact of MEMS is very wide and deep. MEMS technology has also received great attention from the optical communication industry because of its advantages, such as low cost, higher performance, reduced size and weight, and increased reliability. A tremendous research effort has focused on the development of MEMS based components in the optical communication technology area. The optical micro-switch is one of the most important and active branches in the area of applying MEMS technology to fiber optical communication system. Among these actuation mechanisms for micro-switch, electrostatic and electro-thermal mechanisms are becoming two very important actuation mechanisms in recent years.

In the category of electrostatic actuating mechanisms, optical micro-switches can take two forms: parallel plate and interdigitated (or comb-drive). In the parallel plate approach,

one plate is suspended at a certain distance from another plate by suspension springs, and this distance is varied in response to the electrostatic force between the plates induced by an applied voltage [5]. Instead of parallel plate style devices, researchers have designed, fabricated and experimentally tested interdigitated "comb" structure devices [6].

Optical micro-switches can also be built using an electro-thermal actuating mechanism. Compared with electrostatic micro-switches, switches actuated by thermal actuators have several advantages: such as lower driving voltages, avoiding the static charges collecting on the plates.

Also, compared with widely used electrostatic forces, thermal expansion can provide larger forces. However, a single-material actuator based solely on the thermal expansion of a beam would have a small deflection relative to the size of the actuator. Differential expansion of a laminate made of two materials of unequal thermal expansion coefficients, the bimetallic or bimorph [7], can be used to amplify deflection. Horizontal thermal actuators, one of the most famous thermal actuators designed by John H. Comtois and Victor M. Bright, takes advantage of the shape to create a "bimetallic" effect using a single material [8]. The current passes through the entire structure when the thermal actuator is activated. Internal Joule heating causes elastic structures to expand and generate deflection when the structures are mechanically constrained. Such actuators were also reported in [9-11].

Modeling of the thermal actuator began with the horizontal thermal actuator in [9]. Finite element method (FEM) also has been employed to analysis the horizontal thermal actuators in [11,12]. The analytical model of the thermal actuator was presented by Qing-An Huang and Neville Ka Shek Lee in [10,13]. In the electro thermal analysis, they

simplified the thermal analysis of the horizontal thermal actuator as a one-dimensional problem. Then, the force method and virtual work have been used to solve the thermal mechanical problem. The analytical result is in good agreement with the experimental results at low temperatures.

Most thermal actuators have been fabricated by surface micromachining using polysilicon as structural material [8,9]. But the generated out-of-plane deflection is an undesirable effect for the in-plane thermal actuators. Thermal actuators fabricated on Silicon-on-insulator (SOI) wafer have been reported in [11] by using single-crystalline silicon layer as thick structural material which overcomes this out-of-plane deflection. In this thesis, we have developed electro-thermal micro-switches based on CMOS-compatible bulk-micromachining as well as standard surface micromachining (MUMPs) to investigate the device performances.

1.3 Thesis Outline

This thesis focuses on the development of MEMS-based optical switches components. This work mainly highlights the micro-switches based on electro-thermal actuation mechanisms (we presented uni-directional micro-switches and novel bi-directional micro-switches). These devices are fabricated by two micromachining techniques: MUMPs and CMOS-compatible micromachining.

The definition of optical MEMS is given in Chapter 2. This chapter also introduces the micromachining techniques and their features, followed by a discussion of different optical micro-switches structures and actuation mechanisms. Also, MUMPs and CMOS

techniques are introduced in Chapter 2 because all of the devices in this thesis are fabricated using MUMPs or CMOS compatible micromachining.

Chapter 3 introduces uni-directional micro-switches designs for both MUMPs technology and CMOS-compatible technology, and also documents the FEM analysis for device performances and analytical solution of the uni-directional thermally actuated micro-switches. A novel bi-directional micro-switch uniquely designed for CMOS technology is also first presented in this chapter. The difference of the new bi-directional thermally actuated micro-switch from the traditional thermally actuated uni-directional micro-switch is that the new micro-switch can be bent in two directions. By applying a similar FEM approach as that in uni-directional micro-switch, the FEM model for the bi-directional micro-switch is used to explore the device behaviors.

The standard MUMPs and CMOS technologies were used to fabricate these two kinds of micro-swtiches. In order to release the micro devices from CMOS technology, the post-processing experiments and effort with pad passivation are described in Chapter 4.

After the devices fabricated from both of MUMPs and CMOS technologies are released, the displacement measurements for these different devices are summarized in Chapter 5. During these experiments, some special phenomena were found and discussed in this chapter. Chapter 6 concludes the thesis. The key findings are highlighted and recommendations for the future work are presented.

Besides the electro-thermally actuated micro-switches, a new electrostatic actuated micro-switches design is also included in Appendix of this thesis. This electrostatic switch includes interdigitated "comb" structure and parallel plates in one device.

Chapter 2

Backgrounds

2.1 Introduction of MEMS for Optical Application

Over the last several years, great strides have been made in bringing the research areas of fiber optics and micro-electro-mechanical systems (MEMS) to the forefront of emerging technologies. MEMS is positioned to become the dominant technology in optical cross-connect switches. MEMS optical switches with complex movable 3D mechanical structures, micro-actuators, and micro-optics can be monolithically integrated on the same substrate by using the mature fabrication processes of the integrated circuit industry. In this chapter, we introduce various popular actuating mechanisms and switch architectures of MEMS optical switches. The basics of surface micromachining and bulk micromachining techniques used to fabricate MEMS devices will be reviewed. Examples of 2D and 3D approaches to MEMS optical switches will be described. The pros and cons of the two approaches are analyzed.

One of the most promising applications of MEMS technology is in optical communication in general and optical cross-connect (OXC) switches in particular. The OXC switches in today's network rely on electronic cores. As port count and data rates increase, it becomes increasingly difficult for the electronic switch fabrics to meet future demands. It is widely acknowledged that electronic switch fabrics are the bottleneck in tomorrow's communication networks. This bottleneck has stimulated intensive research in developing new all-optical switching technologies to replace the electronic cores. All-optical networks offer many advantages compared to conventional optical-to-electronic and electronic-to-optical networks, including cost-effectiveness, immunity from

electromagnetic interference, bit rate/protocol transparency, and ability to implement wavelength-division multiplexing (WDM) with relative ease. Therefore, it is desirable to manipulate the data network at the optical level with optical switches. The optical switches are used to reconfigure/restore the network, increase its reliability, and/or act as the optical add/drop multiplexer (OADM). There are, indeed, many technologies competing to replace the current electronic switch fabrics. A successful optical switching technology will have to demonstrate superiority in the areas of scalability, insertion loss, polarization-dependent loss (PDL), wavelength dependency, small size, low cost, crosstalk, switching speed, manufacturability, serviceability, and long-term reliability. Conventional mechanical switches, which are based on macroscopic bulk optics, utilize the advantages of free-space optics; however, they suffer from large size, large mass, and slow switching time. On the other hand, guided-wave solid-state switches have yet to show great potential because their high losses and high crosstalk limit their scalability. The recent development of free-space optical MEMS technology has shown superior performance for this application. MEMS optical switches not only retained their conventional counterparts' advantages of free-space optics such as low losses and low crosstalk, but also included additional ones such as small size and small mass. Furthermore, MEMS fabrication techniques allow integration of micro-optics, micro-actuators, complex micromechanical structures, and possibly microelectronics on the same substrate to realize integrated Microsystems [14].

2.2 Micromachining Techniques

MEMS fabrication techniques utilize the mature fabrication technology of IC industry. The fact that silicon is the primary substrate material used in the IC circuitry and that it also exhibits excellent mechanical properties make it the most popular micromachining material. The micromechanical structures used in MEMS optical switching can be fabricated using the popular micromachining technologies, such as, bulk micromachining and surface micromachining.

2.2.1 Bulk Micromachining

This is the most mature and simple micromachining technology. Bulk micromachining is sometimes called the etching/subtraction process. It involves the removal of silicon from the bulk silicon substrate by etchants. There are two types of chemical etchants, anisotropic and isotropic. Anisotropic etchants etch different silicon orientation planes at different rates. Figure 2-1(a) shows the silicon planes exposed by using anisotropic etchants. Figure 2-1(b) shows a 3D mechanical structure that was fabricated using anisotropic etching.

Isotropic etchants, on the other hand, etch the silicon evenly in all directions. Figure 2-1 (c) shows the effect of isotropic etches on silicon substrate. Note that the mechanical structure that can be created by bulk micromachining is not very complex.

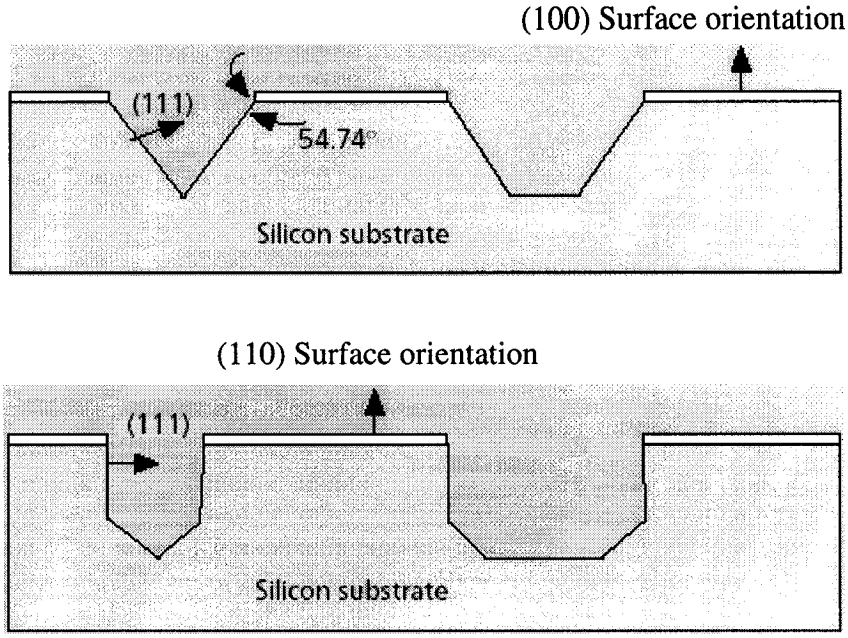

Figure 2-1. (a) Anisotropic wet etching of (100) and (110) silicon substrate
(b) Deep cavity form in silicon by anisotropic etchants
(c) Isotropic etching of silicon [14].

2.2.2 Surface Micromachining

Surface micromachining is a more advanced fabrication technique. Complex 3D mechanical structures can be created using alternate layers of sacrificial and structural materials. Sacrificial layers act as spacers between structural layers. Freestanding 3D mechanical structures will be formed when the sacrificial layers are etched away during final release. In surface micromachining, thin-film materials are selectively added to or removed from the wafer. Thin-film material deposited where a freestanding mechanical structure is needed is called a sacrificial layer. The material that is left after etching of the underlying sacrificial layer is called the structural material. In surface micromachining, a combination of dry and wet etching, and thin film deposition are essential processes to realize micromechanical structures on silicon. A sacrificial layer, such as silicon dioxide, is deposited or grown underneath a patterned material for later removal. The removal process is usually done by chemical etching. After the removal of the sacrificial layer, the patterned material is left as thin-film freestanding mechanical structures as they are suspended over the substrate by the thickness of the etched sacrificial layer.

The Multi-user MEMS processes or MUMPs® is a three-layer polysilicon surface micromachining process. It is a commercial program that provides the international industrial, governmental and academic communities with cost effective, proof-of concept surface micromachining fabrication.

2.2.3 Other Micromachining Techniques

There are many other methods used in the fabrication of MEMS such as laser micromachining, LIGA and so on.

Advances in laser technology, which include optics and beam steering, computer control and a better understanding of laser-material interaction make "laser micromachining" a viable, attractive, cost-effective, and in some cases, enabling technology to support a varieties of applications [15].

Also, with the development of the MEMS technologies, complex microstructures that are thick and three-dimensional are required. Therefore, researches and effort of micromachining techniques are directed towards achieving high aspect ratio and three-dimensional devices. LIGA process is one of those micromachining techniques.

LIGA is an acronym for lithography, electroforming and micromolding (in German, lithographe, galvanoformung, abformung). The LIGA process is a technique for fabrication of three-dimensional microstructures with high aspect ratios having heights of several hundred micrometers, which is not possible with silicon-based micromachining techniques. With the LIGA process it is possible to make more complex microstructures and to work in the third dimension.

2.3 MEMS Optical Switch Architectures

There are currently two popular approaches to implement MEMS optical switches: 2D MEMS switches and 3D MEMS switches.

These two technologies have striking differences in terms of how they are controlled and their ability to redirect light beams. However, both of them have shown promise in finding their niches in telecommunication networks.

2.3.1 2D MEMS Switches

In this architecture, mirrors are arranged in a crossbar configuration as shown in Figure 2-2. Each mirror has only two positions and is placed at the intersections of light paths between the input and output ports. They can be in either the "ON" position to reflect light or the "OFF" position to let light pass uninterrupted. The binary nature of the mirror positions greatly simplifies the control scheme. Typically, the control circuitry consists of simple transistor-transistor-logic (TTL) gates and appropriate amplifiers to provide adequate voltage levels to actuate mirrors.

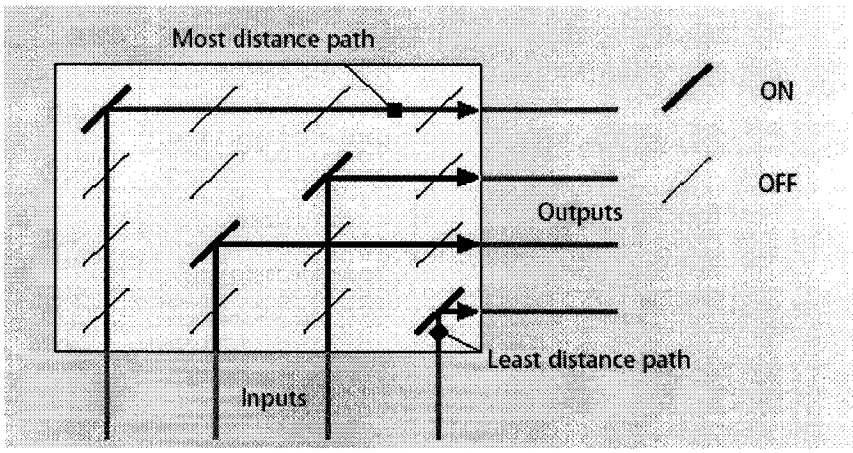

Figure 2-2. A 2D crossbar switching architecture [14].

2.3.2 3D MEMS Switches

A 3D or analog MEMS switch has mirrors that can rotate about two axes. Light can be redirected precisely in space to multiple angles — at least as many as the number of inputs. This approach results in only N or 2N mirrors. Currently, a majority of commercial 3D MEMS switch designs use two sets of N (total of 2N) mirrors to minimize insertion loss. Alternatively, if only N mirrors were used, port count would be

limited by insertion loss that results from finite acceptance angle of fibers/lens. Another advantage is that differences in free-space propagation distances among ports-to-ports switching are much less dependent on the scaling of the port-count. This architecture can be scaled to thousands by thousands of ports with high uniformity in losses. Inevitably, much more complex switch design and continuous analog control are needed to improve stability and repeatability of the mirror angles. Lucent Technologies announced a 3D optical crossconnect using MEMS mirror array called WaveStar™ Lambda Router [16]. The mirror can rotate on two axes and is continuously controllable to tilt greater than ±6°. Figure 2-3 shows a close-up view of the WaveStar MEMS mirror.

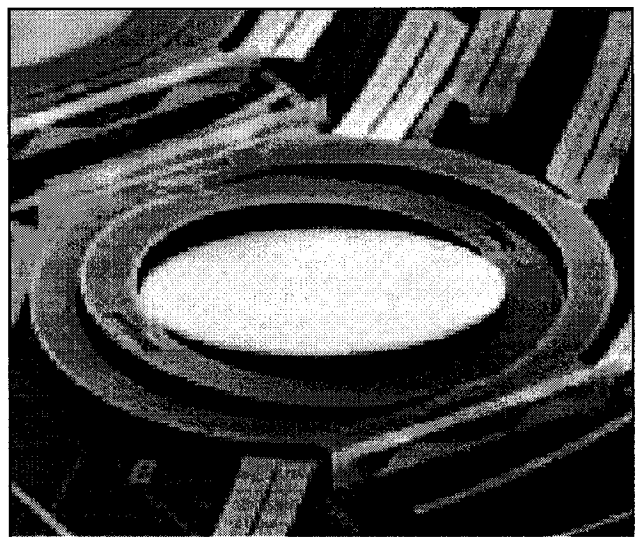

Figure 2-3. A close-up view of a MEMS mirror [16].

2.4 Actuating Mechanisms of Micro-Switches

In order for MEMS to be a viable optical switching technology, the actuating mechanisms used to move these mirrors must be easy to fabricate, accurate, predictable, reliable, and consume low power. This section briefly describes three actuating

mechanisms that are being researched extensively in the university laboratories as well as the industry.

2.4.1 Electro-Thermal Mechanism

Actuators based on the thermal expansion effect can provide a large force and a deflection perpendicular or parallel to the substrate. They have been shown to be a valuable complement to electrostatic actuators. The operating principle of a thermally driven actuator with lateral motion (parallel to the substrate) is the asymmetrical thermal expansion of a microstructure with variable cross sections. The resistance of the narrower section of the microstructure is higher than that of the wider section. When current passes through the actuator, more power dissipates in the narrower section, causing it to expand more than the wider section. This differential thermal expansion may be compared to that of a bimorph structure, causing the actuator to move laterally.

2.4.2 Electrostatic Mechanism

Electrostatic forces are used as the driving forces for many actuators. Electrostatic forces involve the attraction forces of two oppositely charged plates. The advantages of electrostatic actuation are that it has very well researched and understood behavior. Furthermore, it has very good repeatability, a very important property in optical switching. The disadvantages include nonlinearity in force vs. voltage relationship, and requirement of high driving voltages to compensate for the low force potential.

MEMS tilting mirrors alter the free-space propagation of light beams by moving into their propagation paths, thus achieving their switching functionality. The micromirror design usually involves mirrors being held in parallel plane (OFF) to the underlying electrodes. When an electrode is charged at a different voltage level than that of its corresponding mirror, the mirror will be tilted down to its "ON" position and thereby reflect a light beam to a different output fiber.

2.4.3 Electromagnetic Mechanism

Electromagnetic actuation involves attraction between electromagnets with different polarity. The advantages of electromagnetic actuation are that it requires low driving voltages because it can generate large forces with high linearity. Disadvantages such as shielding from other magnetic devices to prevent crosstalk is difficult, and it has yet to prove reliable. The California Institute of Technology has developed a magnetic 2x2 MEMS fiber optical bypass switch [17].

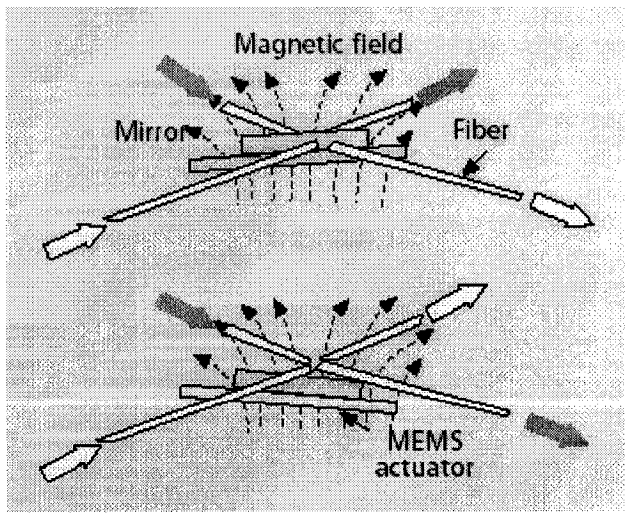

Figure 2-4. A close-up view of a MEMS mirror [17].

The operation principle of the magnetic MEMS switch in Figure 2-4 is: The thin double-sided bulk-micromachined mirror moves up or down in response to changing magnetic field. When the mirror moves up, it blocks the optical path to opposing optical fibers. In this case, light signal is reflected off the mirror into neighboring optical fibers. When the mirror moves down, it moves below the level of the optical fibers, and light signal is transmitted to opposing optical fibers. Electromagnetic actuation can achieve this displacement with less than 100 mW.

2.5 Micromachining Foundries

2.5.1 CMOS-Compatible Micromachining

Standard industrial CMOS technology can be used to fabricate MEMS devices with post-etching step to release the devices. This type of CMOS-compatible bulk micromachining provides a low cost monolithic solution for the integration of MEMS. Front-side bulk micromachining is most often used since it allows low cost mask-less silicon etching. A standard CMOS process is used to realize the actuator and control circuits, followed by a post-process of anisotropic wet etching that produces cavities on the substrate silicon to suspend the microstructures. The suspended parts are thermally isolated from the bulk. The suspended structures can be made of a sandwich of oxides (including LOCOS, gate and inter-level oxides), polysilicon and metal layers. Figure 2-5 shows a cross section of suspended structures. The cavity can be etched using wet anisotropic etchants such as Potassium hydroxide (KOH), Tetramethyl-ammonium hydroxide (TMAH) and Ethylenediamine-pyrocatechol (EDP). The etching takes place over the faster-etching crystallographic planes [18].

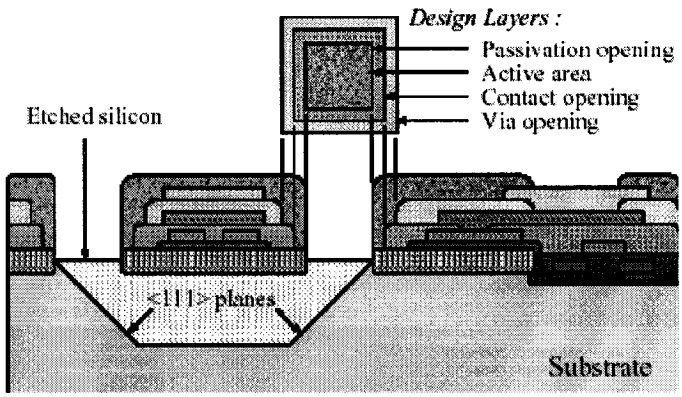

Figure 2-5. CMOS manufacturing process and associated post-process [18].

2.5.2 MUMPs Surface Micromachining

The Multi-User MEMS Processes or MUMPs® is a three-layer polysilicon micromachining process derived from work performed at the Berkeley Sensors and Actuators Center (BASC) at the University of California in the late 80's and early 90's. This process has the general features of a standard surface micromachining process as follows [19]:

- Polysilicon is used as the structure material
- Deposited silicon oxide is used as the sacrificial layer
- Silicon nitride is used as electrical isolation between the polysilicon and the substrate
- Metal (usually gold) is the top layer of the device and used as conductive layer

Figure 2-6 shows the cross section of an electrostatic motor fabricated by the MUMPs process. This device includes all the layers that are available in the MUMPs process. In order to make the process as general as possible, MUMPs process defines all the layers' thickness and their functions. All MEMS designers have to follow these definitions and design rules. These definitions and design rules limit the designers to design more

complex devices, but they make it possible for many different designs to be put on a single silicon wafer in one single fabrication process. Also, the standardization of the fabrication process reduces the fabrication cost and lets more and more designers submit their designs.

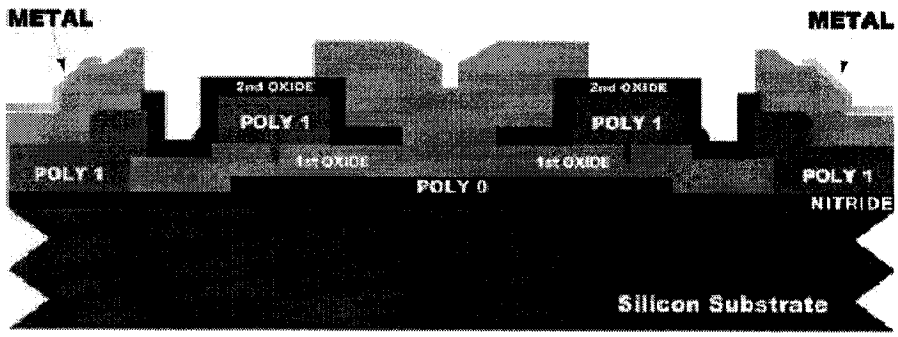

Figure 2-6. Cross section of structures after the process is completed [19].

After the final, unreleased structure is finished, the wafer are diced, sorted and shipped to the MUMPs® users for sacrificial release and test. Figure 2-7 is the cross section of structure after sacrificial oxide release. The release is performed by immersing the chip in a bath of 49% HF (room temperature) for 1.5-2 minutes. This is followed by several minutes in DI water and then alcohol to reduce stiction followed by at least 10 minutes in an oven at 110°C.

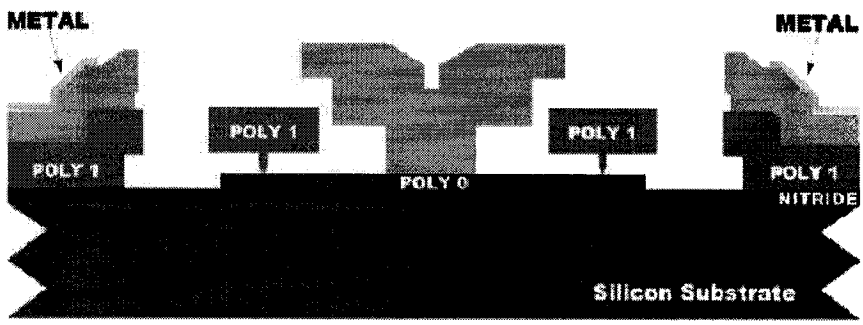

Figure 2-7. Cross section of structures after HF released [19].

Chapter 3

Electro-Thermally Actuated Micro-Switches

In micromechanical structures, actuators based on electrostatic forces operate at low power and high frequency, and are highly desirable. However, they have typically small deflections and require either close dimensional tolerances or high voltage to achieve large deflections. On the other hand, actuators based on the thermal expansion effect can provide a large force and a deflection perpendicular or parallel to the substrate. They have been shown to be a valuable complement to electrostatic actuators. In particular, polysilicon thermal actuators can operate in an integrated circuit (IC) current/voltage regime and can be fabricated by a surface-micromachining technology that is compatible with IC technology.

3.1 Uni-Directional Electro-Thermally Actuated Micro-Switches

3.1.1 Introduction

The operating principle of a thermally driven actuator with lateral motion (parallel to the substrate) is the asymmetrical thermal expansion of a microstructure with variable cross sections. The resistance of the narrower section of the microstructure is higher than that of the wider section. When current passes through the actuator, more power dissipates in the narrower section, causing it to expand more than the wider section. This differential thermal expansion may be compared to that of a bimorph structure, causing the actuator to move laterally. At the same time, this principle also renders the deflection of the actuator to be related to various process parameters, the physical geometry, and the driving current.

In Figure 3-1, the U-shaped folded beam micro-switch, which may be used as a micro shutter, consists of a "wide beam" and a "narrow beam" with a blade structure at the end as the shutter. When current is passed through the micro-switch from one mechanically anchored electrode to the other, the narrow beam becomes hotter than the wide beam due to the much higher current density and the ensuing larger Joule heating. As a result, the narrow beam tends to expand more than the wide beam and causes the whole structure along with the shutter blade to move toward "wide beam" direction.

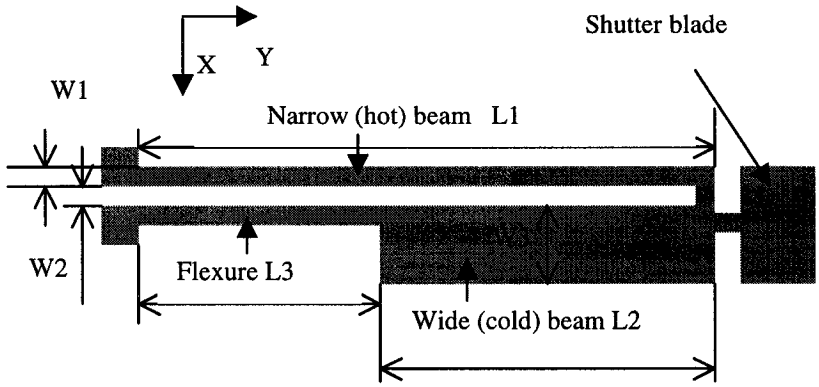

Figure 3-1. Schematic diagram of uni-directional micro-switch.

In order to characterize the uni-directional micro-switches performance, this type of switch has been designed for two different processes: commercial CMOS technology (CMOSP35) and standard surface micromachining (MUMPs). For the CMOS technology, it includes the CMOS-compatible wet post-etching process to etch the cavity and release the devices.

3.1.2 Optical Application of Micro-Switches

One application of these micro-switches is used as an optical microshutter or attenuators as we just explained. In this example application, a transmission light modulating

principle was selected; it relies on electro-thermally operated, laterally moving shutters, thereby switching off or on a spot of light. An important advantage of using a transmission scheme as opposed to a reflective scheme is that: in the active state (shutters open), the system performance is not defined by the optical properties of the shutter blade, nor by its fabrication tolerances. In Figure 3-2, when the input power is on, the shutter blade is moved toward wide beam direction and the light will pass through. When the power is off, the shutter part will block the light. The post-etching is used here to make the cavity and release the microstructure.

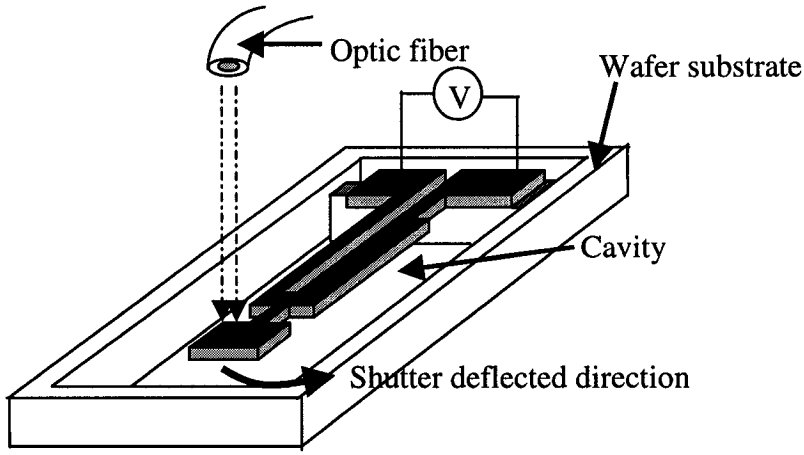

Figure 3-2. Schematic diagram of micro-switch application.

3.1.3 Device Designs for CMOS Technology

This CMOS technology used by our design is CMOSP 35 technology. This technology, manufactured by Taiwan Semiconductor Manufacturer Corporation (TSMC), is a 0.35-micron dual poly, triple metal, polycide CMOS process. The recommended nominal supply voltage is 3.3 volts. The minimum drawn gate length is 0.35 μm. The designs for uni-directional micro-switch were used only one polysilicon layer and without embedded

metal layer. After the devices are fabricated, a CMOS-compatible anisotropic wet etching process is carried out by using TMAH to etch silicon underneath the microstructures, and release the devices. The silicon dioxide layer embracing the polysilicon structure layer is used as a protection layer during the wet etching process.

3.1.3.1 Device Design (I)

The schematic view of design (I) is shown in Figure 3-3. The operation principle was already presented in the introduction section of this chapter.

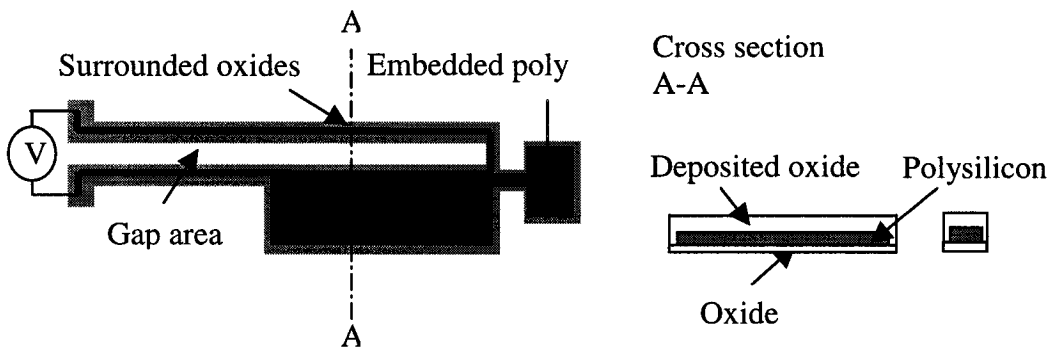

Figure 3-3. Uni-directional micro-switch design (I) for CMOS technology and its schematic cross-section view.

3.1.3.2 Device Design (II)

The second design of uni-directional micro-switch is given in Figure 3-4. Two identical uni-directional switches are combined together. When we apply the power supply to both of the single uni-directional switches, it will generate almost the same displacement as that of a single uni-directional micro-switch, but the generated force is more than that of a single uni-directional micro-switch.

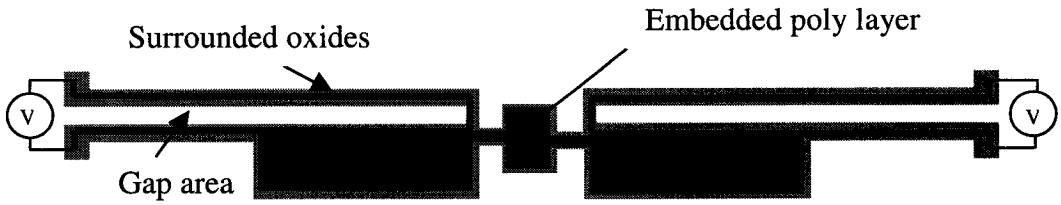

Figure 3-4. Design of uni-directional switch (II) for CMOS technology.

3.1.4 Devices Designs for MUMPs Technology

The three-layer polysilicon MUMPs process provides variability in microstructure design. There are no oxide layers surrounding the polysilicon as the structures in CMOS technology. The designs for this uni-directional micro-switch based on MUMPs process in this thesis have two categories: in the first one, design variations are in plane geometry, for the second category, the design variations are in devices cross-section and thickness.

3.1.4.1 Design Variations (I)

Three different design prototypes are presented in this part:

1) The first uni-directional micro-switch design in MUMPs technology is shown in Figure 3-5. This design is similar to the design for CMOS technology except for the surrounding oxide layer.

Figure 3-5. Schematic diagram of micro-switch design (I) for MUMPs technology.

2) In our second design, the suspended flexure is made of serpentine springs. A schematic view of a serpentine spring based micro-switch is shown in Figure 3-6. Serpentine spring get their name from the meandering snake-like pattern of the beam segments. Each meander is of length a, and width b, except for the first and last meanders, which are of width c. This kind of spring has been previously studied in [20]. The spring constant is a function of the number of meanders and design variables (a, b and c). Therefore this new design can offer the possibility to reduce the spring constant and increase the deflection.

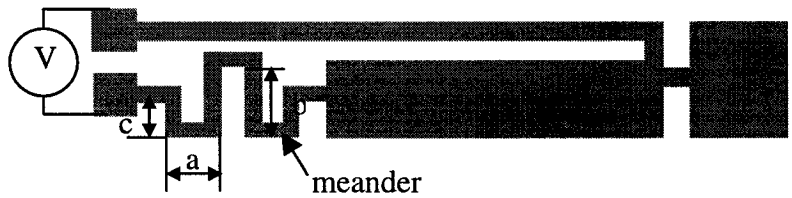

Figure 3-6. Schematic diagram of uni-directional micro-switch design (II).

3) Some effort has been directed at resolving these limitations of traditional thermal actuators and improving their efficiency. David M. Burns and Victor M. Bright designed a thermal actuator which has two hot arms [21]. This kind of two-hot arm thermal actuator is shown in Figure 3-7. In this thermal actuator, the electric current only passes through the outer and inner hot arms. This avoids the cold arm and flexure to being part of the electric circuit. It dramatically increases the efficiency since all the power consumed in the actuator contributes to the deflection of the thermal actuator. The flexure can also be thinner than the hot arm because no current passes through the flexure.

Figure 3-7. Schematic diagram of uni-directional micro-switch design (III).

3.1.4.2 Design Variations (II)

For the design variations in cross section and thickness, in order to characterize the devices performances, we have different designs in thickness which use POLY1 layer, POLY2 layer and double thickness structures (a technique developed for producing polysilicon parts made of both POLY1 layer and POLY2 layer). So the micro-switches can be 2μm, 1.5μm and 3.5μm thick respectively as Figure 3-8 shows.

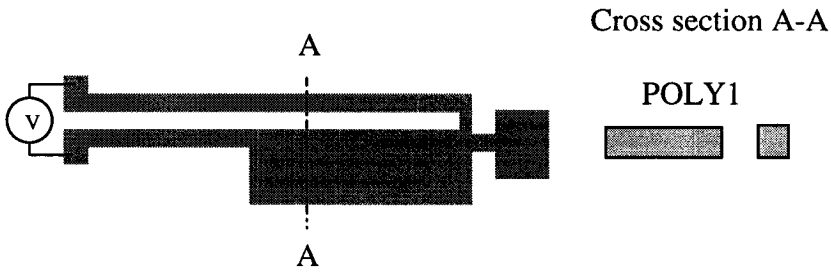

Figure 3-8. (a) Top view and cross-section view of design (a).

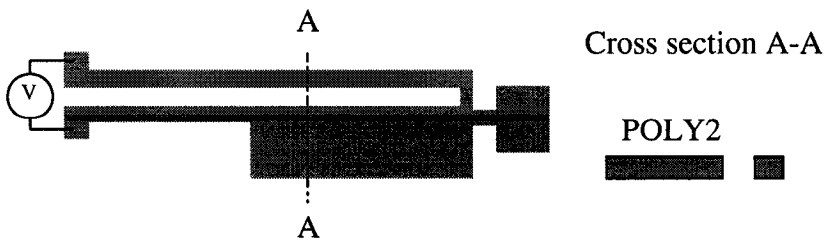

Figure 3-8. (b) Top view and cross-section view of design (b).

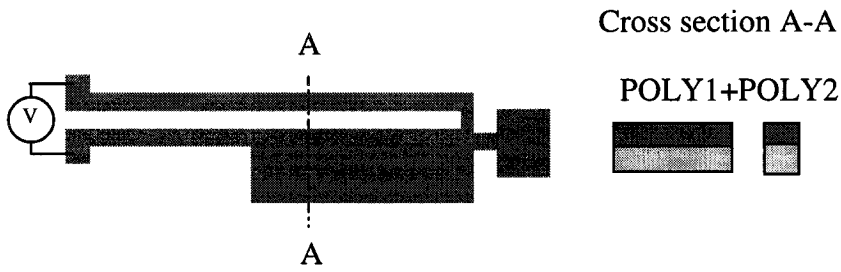

Figure 3-8. (c) Top view and cross-section view of design (c).

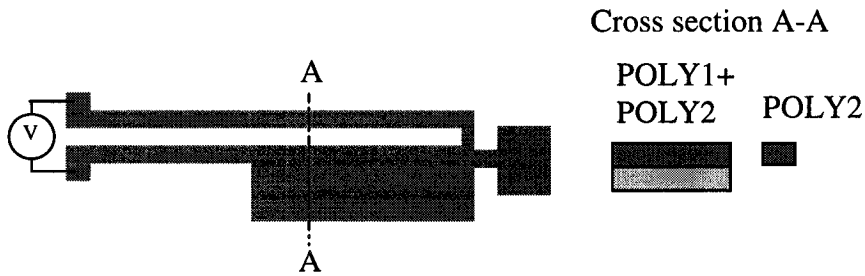

Figure 3-8. (d) Top view and cross-section view of design (d).

These designs were used to study how the thickness affects the out-of-plane deflection. And the last design maximizes the cross-section difference between narrow and wide beam, and improve the microstructure displacement.

3.1.5 FEM of the Device Performances

Based on the principles of electro-thermal actuated micro-switches, the FEM analysis has been performed to analyze the variation of device performance with device geometry before fabrication. A finite element software ANSYS was used in this work.

The devices were first analyzed by ANSYS. In general, it is desired to design polysilicon thermal micro-switches with large deflection. Hence, deflection as a function of geometry is studied here based on the following FEM analysis. Since the thickness of the structure (polysilicon layer) is very small compared to the length and width of the device, this

analysis can be simplified by 2-dimensional analysis. The polysilicon material properties and initial device dimensions for the uni-directional micro-switch structure in Figure 3-1 are given in Tables 3.1 and Table 3.2.

Table 3.1 Polysilicon material properties used in FEM analysis

Young's modulus	169GPa
Poisson ratio	0.22
Electric resistivity	2.3e-5 ohm-m
Thermal expansion coefficient	3.8e-5/° K
Thermal conductivity	150W/m °K

Table 3.2. Device initial dimensions

Narrow beam	Length (L1)	200μm
	Width (W1)	4μm
Wide beam	Length (L2)	160μm
	Width (W3)	24μm
Flexure length	Length (L3)	40μm
	Width (W1)	4μm
Shutter	Length	50μm
	Width	W1+W2+W3=32μm
Gap between two beams	W2	4μm

A 2-dimensional model of the structure depicted in Figure 3-1 is implemented in ANSYS 5.7 (university version) to obtain approximate performances tendencies. In order to

simplify the analysis, we removed the shutter parts of the devices. The simulation was divided into two steps: electro-thermal analysis first (using thermal-electric coupled-field element PLANE67) and then followed by thermal-structure analysis (using plane stress element PLANE42) [22]. Figures 3-9 and Figure 3-10 show the heat distribution and simulated displacement of the analyzed device example.

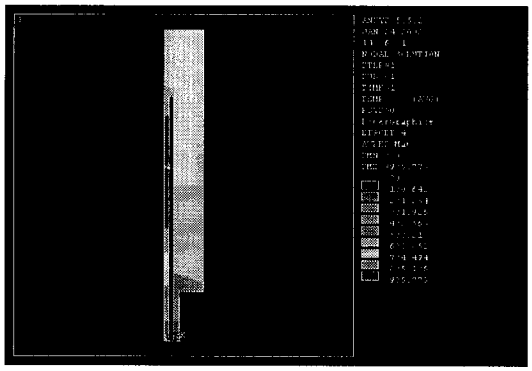

Figure 3-9. Temperature distribution along the device.

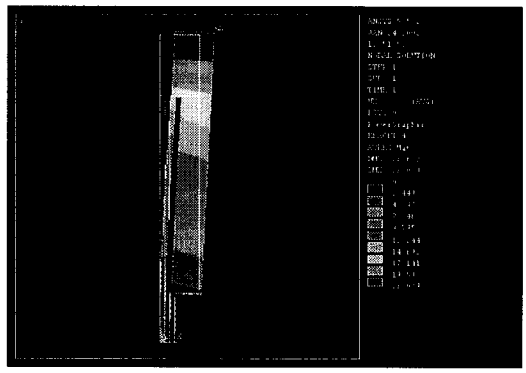

Figure 3-10. Simulated displacement of the device.

Two groups of analysis examples are applied to analyze the device behaviors.

(1) Shutter displacement vs. W3 (width of wide beam): While the other dimensions are held constant, W3 is varied. Figure 3-11 reports the corresponding shutter deflection in the x, y directions. As the width of the wide beam increases, the temperature difference between the two beams increases, in turn, resulting in a larger deflection in the structure.

(2) Shutter deflection vs. total length (L1+L2+L3): in this analysis, the total length varies from 200μm to 500μm (Same as L1 varies from 100μm to 250μm). All others dimensions were kept constant at their initial values in Table 3.2, except that L2/L3 was kept as a constant ratio, it was chosen as 4 here. Figure 3-12 shows that, as the total beam length increases, the deflection increases.

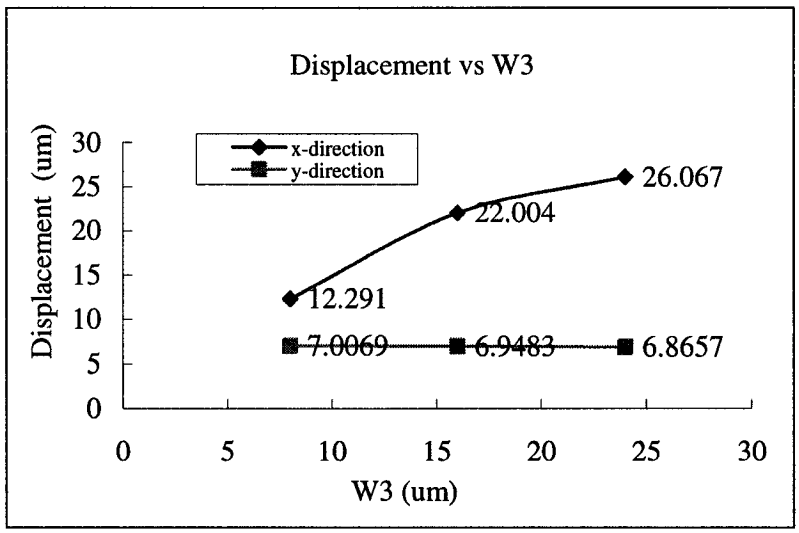

Figure 3-11. Shutter displacements in x, y direction vs. the width of wide beam.

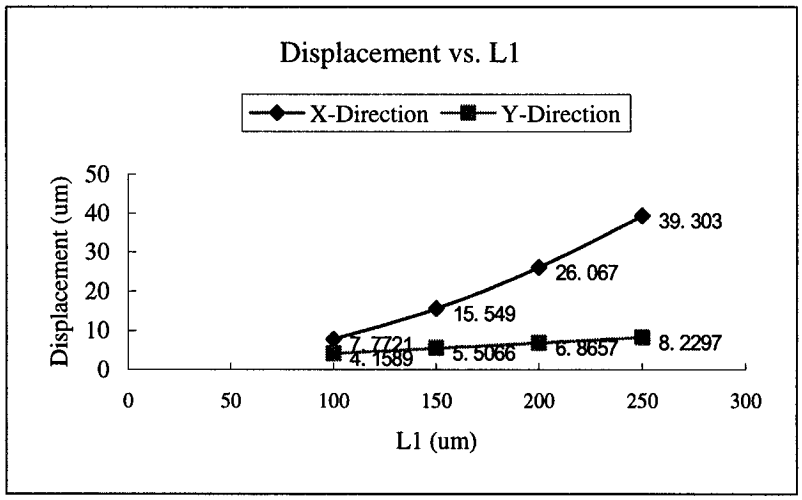

Figure 3-12. Shutter displacements in x, y directions vs. total length of the device.

In general, the performance of a polysilicon thermal micro-switch is related to process parameters and geometry as well as input power. Since the process parameters are fixed by each specific fabrication technology, the geometry will become the main design

consideration. From above analysis, we can conclude that wider cold beam; longer total length can achieve larger deflection.

3.1.6 Analytical Modeling

Using FEM analysis to optimize the structure of a micro-switch has been reported by other researchers in [23,24]. Obviously, it is versatile for an analytical method to be used in the design of micro-switches due to its simplicity. Analytical models have been reported [13,25] so as to provide an insight into the operation of the actuator, and to allow for predicting the performance of actuators with new designs before fabrication.

The analytical method depends on fabrication process since the layers under the suspended structure are process related. And it will affect the simulation results. For example, the devices fabricated by standard CMOS technology and MUMPs surface micromachining will need different model modification. Figure 3-13 shows the device simplified cross-section diagrams for MUMPs and CMOS-compatible bulk micromachining.

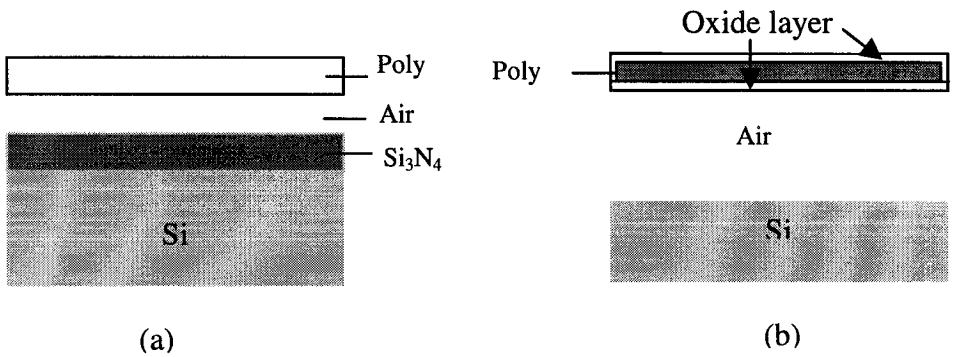

Figure 3-13. The devices cross-section diagram of for (a) MUMPs technology, and (b) CMOS technology.

Since the layers under the suspended structure are process related, and based on the previous researchers' works [13,25], we modified an analytical model for our electro-thermally actuated polysilicon micro-switches fabricated by MUMPs process.

3.1.6.1 Electro-Thermal Analysis

A diagram of a polysilicon thermal actuator is shown in Figure 3-14. The width of hot beam and flexure is same in this analysis.

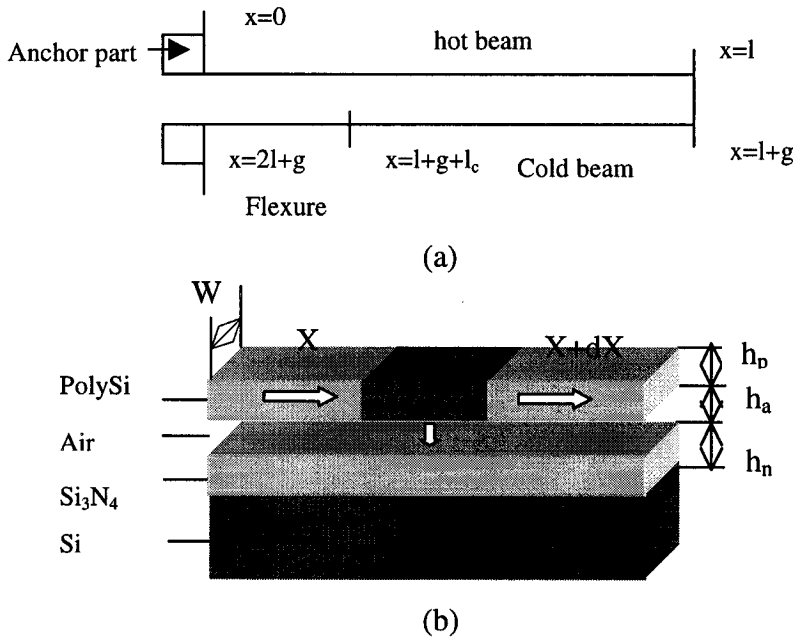

Figure 3-14. (a) Simplified one-dimensional coordinate system, (b) Cross-section diagram of the actuator for thermal analysis.

The electro-thermal response of polysilicon microbeams is generally simplified for analysis in one dimension, since the length of the microstructure is much greater than its cross-section. The arms of the actuator may be decomposed into three-line shape microbeams connected in series. The coordinate system for thermal analysis is given in

Figure 3-14(a). A part of the cross-section of the actuator is shown in Figure 3-14(b). The silicon nitride layers shown in this figure are used as electrical and thermal insulation.

The resistivity of polysilicon, ρ, is usually related to temperature. The resistivity is assumed here to have a linear temperature coefficient, ξ, such that $\rho(Ts) = \rho_0$, that is,

$$\rho(T) = \rho_0[1 + \xi(T-Ts)] \tag{3.1}$$

Where T is the operating temperature, and T_s is the substrate temperature.

When there exists a temperature gradient within a body, heat energy will flow from the region of high temperature to the region of low temperature. This phenomenon is known as conduction heat transfer, and is described by the equation:

$$q = -k\vec{\nabla}T \tag{3.2}$$

This equation determines the heat flux vector q for a given temperature profile T and thermal conductivity k. the minus sign ensures that heat flows down the temperature gradient. Therefore, as shown in Figure 3-14(b), the heat flow equation of this micro device is derived by examining a differential element of the microbeam of width w, thickness h_p and length Δx. Under steady-state conditions, resistive heating power generated in the element is equal to heat conduction out of the element [13].

$$-k_p w h_p [\frac{dT}{dx}]_x + J^2 \rho w h_p \Delta x = -k_p w h_p [\frac{dT}{dx}]_{x+\Delta x} + s\Delta x w \frac{T - T_s}{R_T} \tag{3.3}$$

Where k_p is the thermal conductivity of polysilicon, J is the current density, S is the shape factor which accounts for the impact of the shape of the element on heat conduction to the substrate [26] and R_T would be the thermal resistance between the polysilicon microbeam and the substrate if the microbeam were wide enough. R_T is given by

$$R_T = \frac{h_a}{k_a} + \frac{h_n}{k_n} \tag{3.4}$$

Where h_a, h_n are the elevation of the element above the Si_3N_4 surface and the thickness of Si_3N_4, respectively and, k_a and k_n are the thermal conductivity of air and Si_3N_4, respectively. The shape factor for heat conduction is given by one of the reference paper [26].

$$s = \frac{h_p}{w}\left(\frac{2h_a}{h_p} + 1\right) + 1 \tag{3.5}$$

Taking the limit as $\Delta x \to 0$ for equation (3.3) produces the following second-order differential equation.

$$k_p \frac{d^2T}{dx^2} + J^2\rho = \frac{s}{h_p}\frac{(T - T_s)}{R_T} \tag{3.6}$$

Physically, the first term on the left side of equation (3.6) represents the net rate of heat conduction into the element per unit volume. The second term on the left side is the rate of heat energy generation inside the element per unit volume, and the right side represents the rate of heat energy loss in the element per unit volume. Changing variables for equation (3.6) with equation (3.1) yields

$$\frac{d^2 f(x)}{dx^2} - A^2 f(x) = 0 \tag{3.7}$$

With

$$f(x) = T(x) - T_\theta$$

$$T_\theta = T_s + \frac{J^2\rho_0}{k_p A^2}$$

$$A^2 = \frac{s}{k_p h_p R_T} - \frac{J^2\rho_0\zeta}{k_p}$$

Solving equation (3.7) and applying the solution to the hot arm, cold arm and flexure, one obtains the temperature distribution as follows, respectively.

$$T_h(x) = T_H + C_1 e^{A_h x} + c_2 e^{-A_h x} \tag{3.8}$$

$$T_c(x) = T_C + C_3 e^{A_c x} + c_4 e^{-A_c x} \tag{3.9}$$

$$T_f(x) = T_F + C_5 e^{A_f x} + c_6 e^{-A_f x} \tag{3.10}$$

Where T_H and A_h are the same as $T\theta$ and A, respectively, except that w is replaced by w_h; T_C and A_c are the same as $T\theta$ and A, respectively, except that w is replaced by w_c; w_h and w_c are the widths of the hot and cold arms, respectively, C_j (j=1 to 6) are the constants to be solved, T_F=T_H and A_f =A_h since the width of the flexure is the same as that of the hot arm.

The anchor pads are assumed to have the same temperature as the substrate. Utilizing the continuity of both the temperature and the rate of heat conduction across the joint points of the hot arm, cold arm and flexure in Figure 3-15, one obtains the following equation (3.11) to solve the constants C_j (j =1 to 6) [13].

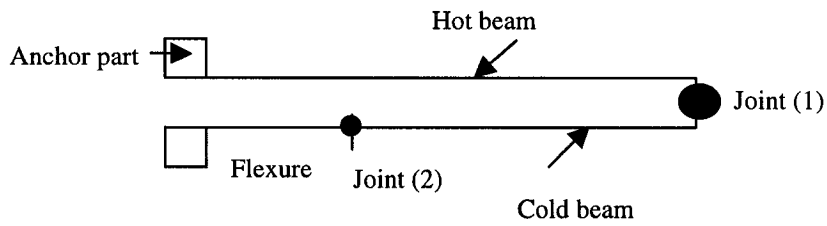

Figure 3-15. Schematic diagram for joints in the device.

$$\begin{bmatrix} 1 & 1 & 0 & 0 & 0 & 0 \\ e^{A_h L} & e^{-A_h L} & -e^{A_c L} & -e^{-A_c L} & 0 & 0 \\ e^{A_h L} & -e^{-A_h L} & -\lambda e^{A_c L} & \lambda e^{-A_c L} & 0 & 0 \\ 0 & 0 & e^{A_c(L+g+L_c)} & e^{-A_c(L+g+L_c)} & -e^{A_h(L+g+L_c)} & -e^{-A_h(L+g+L_c)} \\ 0 & 0 & \lambda e^{A_c(L+g+L_c)} & -\lambda e^{A_c(L+g+L_c)} & -e^{A_h(L+g+L_c)} & e^{-A_h(L+g+L_c)} \\ 0 & 0 & 0 & 0 & e^{A_h(2L+g)} & e^{-A_h(2L+g)} \end{bmatrix} \begin{bmatrix} c_1 \\ c_2 \\ c_3 \\ c_4 \\ c_5 \\ c_6 \end{bmatrix} = \begin{bmatrix} T_s - T_H \\ T_C - T_H \\ 0 \\ T_H - T_c \\ 0 \\ T_s - T_H \end{bmatrix}$$

(3.11)

Where L and L_c are the lengths of the hot and cold arms, respectively, g is the gap between the hot and cold arms, $\lambda = w_c A_c / w_h A_h$. The above equation (3.11) is written as a matrix format so that one may use the same subroutine as the deflection analysis to solve the linear algebraic equation. Once C_j (j from 1 to 6) are obtained, the resistance of polysilicon, which depends on temperature changes, may be estimated as follows

$$R = \int_0^{2L+g} dR(T) = \frac{L\rho_0}{w_h h_p}[1+\zeta(\overline{T}_h - T_s)] + \frac{(L_c+g)\rho_0}{w_c h_p}[1+\zeta(\overline{T}_c - T_s)] + \frac{L_f \rho_0}{w_h h_p}[1+\zeta(\overline{T}_f - T_s)]$$

(3.12)

Where T_h, T_c and T_f stand for the average temperature of the hot arm, cold arm and flexure, respectively, and they can be expressed as

$$\overline{T}_h = T_H + \frac{c_1}{A_h L}(e^{A_h L} - 1) - \frac{c_2}{A_h L}(e^{-A_h L} - 1) \tag{3.13}$$

$$\overline{T}_c = T_C + \frac{c_3}{A_c(L_c+g)}(e^{A_c(L+g+L_c)} - e^{A_c L}) - \frac{c_4}{A_c(L_c+g)}(e^{-A_c(L+g+L_c)} - e^{-A_c L}) \tag{3.14}$$

$$\overline{T}_f = T_H + \frac{c_5}{A_h L_f}(e^{A_h(2L+g)} - e^{A_h(L+g+L_c)}) - \frac{c_6}{A_h L_f}(e^{-A_h(2L+g)} - e^{-A_h(L+g+L_c)}) \tag{3.15}$$

The linear thermal expansion for the hot arm, cold arm and flexure, which is to be used later to estimate the deflection of the actuator, may be calculated as, respectively,

$$\Delta L_h = \alpha \int_0^L (T_h(x) - T_s)dx = \alpha L(\overline{T}_h - T_s) \tag{3.16}$$

$$\Delta L_c = \alpha \int_0^{L+g+L_c} (T_c(x) - T_s)dx = \alpha L_c(\overline{T}_h - T_s) \tag{3.17}$$

$$\Delta L_f = \alpha \int_{L+g+L_c}^{2L+g} (T_f(x) - T_s)dx = \alpha L(\overline{T}_f - T_s) \tag{3.18}$$

Where α is the thermal expansion coefficient of polysilicon. The thermal expansion due to the section of gap has been ignored in equation (3.17) because of its short length.

For the given parameters such as ρ_0 and ξ, physical geometry and driving current, the temperature distribution can be obtained by equations (3.8)–(3.11). MATLAB codes were developed to analyze the temperature distribution. Figure 3-16 is an example of the temperature distribution for the parameters specified in Table 3.3 and 3.4.

Table 3.3. Polysilicon material properties for analytical analysis

Material Properties	**Value**	**Unit**
Young' Modulus E	$162X10^9$	Pa
Poisson' ration v	0.22	
Thermal expansion coefficient K	$4.7X10^{-6}$	C^{-1}
Thermal conductivity of Polysilicon K_p	$41X10^{-6}$	$W\cdot \mu m^{-1}\cdot C^{-1}$
Thermal conductivity of air K_a	$0.026X10^{-6}$	$W\cdot \mu m^{-1}\cdot C^{-1}$
Thermal conductivity of Nitride K_n	$2.25X10^{-6}$	$W\cdot \mu m^{-1}\cdot C^{-1}$
Resistivity of Polysilicon ρ_0	20	$\Omega\cdot \mu m$

Table 3. 4 Initial device geometry parameters for analytical analysis

Geometrical data	Value	Unit
The length of the hot arm L	240	μm
The length of the cold arm L_c	200	μm
The width of the gap L_g	2	μm
The width of the hot arm W_h	2.5	μm
The width of the hot arm W_c	10	μm
The thickness of polysilicon h_p	2	μm
The thickness of air h_a	2	μm
The thickness of nitride h_n	0.6	μm
Input current	5	mA

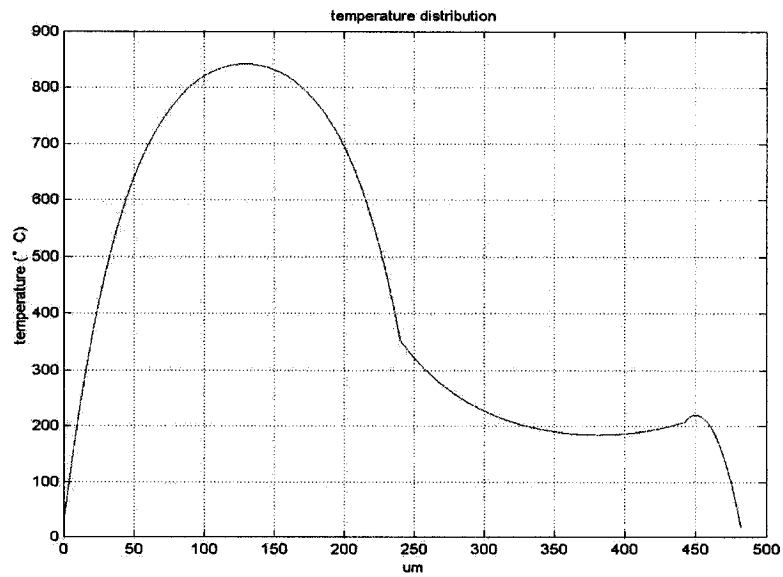

Figure 3-16. Temperature distribution along the total beam (including hot arm, cold arm and flexure).

It is clear from this figure that the temperature in most of the hot arm is much higher than that in the cold arm. It is also obvious that heat loss due to conduction to the substrate affects strongly the temperature in the arms of the actuator. As shown in equation (3.4), the elevation (h_a) of the polysilicon arm above the substrate governs heat loss to the substrate since the thermal conductivity of air is very small. It has been shown that a trench etched under the hot arm of the actuator increases the thermal isolation from the substrate, thereby decreasing the heat loss from the hot arm and increasing the deflection. Qualitatively, from Figure 3-13, we can see that devices fabricated by CMOS-bulk micromachining will have greater deflection since depth of cavities underneath the devices from CMOS-compatible process are much deeper than that of the devices from MUMPs process (2μm only).

As presented in the above, the thermal analysis performed for the actuator is based on heat conduction only. At higher power, however, heat loss due to thermal radiation may become significant. Especially, the heat radiative transfer from the hot arm to the cold one may give rise to increase of the cold arm temperature.

3.1.6.2 Mechanical Deflection Analysis

The structure of the thermal actuator shown in Figure 3-14 is similar to a plane-frame structure with fixed bases for elastic structure engineering. Deflection analysis of such structures has been well documented in [27,28]. Deflection analyses of the one-hot arm and two-hot arm have also been introduced in [13.25]. The principles of deflection analysis [Appendix A] are as follows:

- The force method for the structural engineering is used to analyze the bending moment.
- The virtual-work method for structural engineering is then utilized to estimate the deflection of the actuator.

The thermal actuator in Figure 3-14 is a statically indeterminate structure with the degree of indeterminacy being 3. The force method for structural engineering is first used here to analyze the bending moment of the actuator structure due to the three redundants, X1, X2 and X3, as shown in Figure 3-17(a) where X1 stands for a horizontal force, X2 a vertical force and X3 a couple force. The virtual-work method for structural engineering is then utilized to estimate the deflection of the actuator tip. Following the force method, the three redundants, X1, X2 and X3 can be obtained by solving a set of simultaneous equations:

$$\begin{bmatrix} f_{11} & f_{12} & f_{13} \\ f_{21} & f_{22} & f_{23} \\ f_{31} & f_{32} & f_{33} \end{bmatrix} \begin{bmatrix} X_1 \\ X_2 \\ X_3 \end{bmatrix} = \begin{bmatrix} 0 \\ \Delta L_h - \Delta L_c - \Delta L_f \\ 0 \end{bmatrix} \tag{3.19}$$

Where each item of the right hand side of Equation (3.19) represents the displacement of X_i in its own direction. For example, ΔL_h-ΔL_c-ΔL_f is the displacement of the force X_2 in the X_2 direction. f_{ij} represents the flexibility coefficient which is defined as the deflection at i direction due to the unit force acting in the j direction.

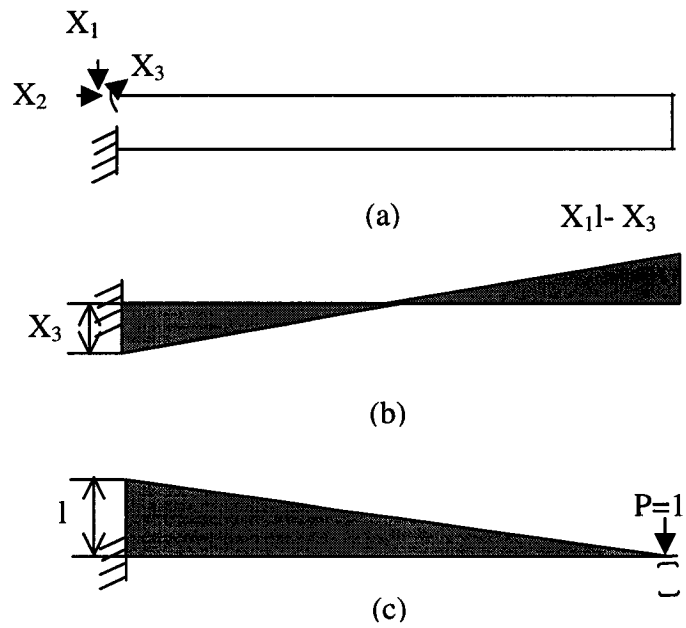

Figure 3-17. (a) The rigid frame simplified for the thermal actuator with three redundants, (b) The bending moment of the hot arm due to the thermal expansion of the structure, (c) The bending moment of the hot arm due to the virtual force [13].

Where terms f_{ij} represent flexibility coefficients were listed respectively in [13].

$$f_{11} = \frac{1}{3EI_h}(L^3 + L_f^3) + \frac{1}{3EI_c}(3L^2 g + L^3 - L_f^3) \tag{3.20a}$$

$$f_{12} = f_{21} = -\frac{1}{2EI_h}(L_f^2 g) - \frac{1}{2EI_c}(g^2 L + L^2 g - L_f^2 g) \tag{3.20b}$$

$$f_{13} = f_{31} = -\frac{1}{2EI_h}(L^2 + L_f^2) - \frac{1}{2EI_c}(L^2 + 2Lg - L_f^2) \tag{3.20c}$$

$$f_{22} = \frac{1}{3EI_c}(g^3 + 3L_c g^2) + \frac{1}{EI_h}(L_f g^2) \tag{3.20d}$$

$$f_{23} = f_{32} = -\frac{1}{2EI_c}(g^2 + 2gL_c) + \frac{1}{EI_h}(gL_f) \tag{3.20e}$$

$$f_{33} = \frac{1}{EI_h}(L + L_f) + \frac{1}{EI_c}(L_c + g) \quad (22f) \tag{3.20f}$$

Where E is the Young's modulus of polysilicon, I_h (= $hW_h^3/12$) is the moment of inertia for the hot arm, I_c (= $hWc^3/12$) is the moment of inertia for the cold arm, EI_h and EI_c represent the flexural rigidity of the hot and cold arms, respectively. The three redundants, X1, X2 and X3 may be solved by equation (3.19). Once they are obtained, the bending moment of the hot arm due to the thermal expansion can be represented as in Figure 3-17(b). In order to obtain the deflection of the actuator tip, a virtual unit force P is applied to the free end of the actuator. The bending moment of the hot arm due to the virtual force is shown in Figure 3-17(c). According to the method of virtual work [13,28], the deflection in the free end of the actuator can be written as [13]

$$u = \int \frac{\overline{M}M}{EI_h} ds = \frac{L^2}{6EI_h}(X_1 L - 3X_3) \tag{3.21}$$

Where M is the bending moment (Figure 3-17(b)) due to the thermal expansion $\overline{M}$ represents the bending moment (Figure 3-17(c)) due to the unit virtual force.

The analytical model has also been applied to study the device performance with variable geometry parameters starting from initial geometries.

(1) In this analysis, the length of narrow beam is variable, but the rest of geometry is held as constant. Figure 3-18 reports the corresponding device temperature distribution and deflection for different lengths of narrow beam. As the length of the narrow beam increases, a larger deflection can be gained.

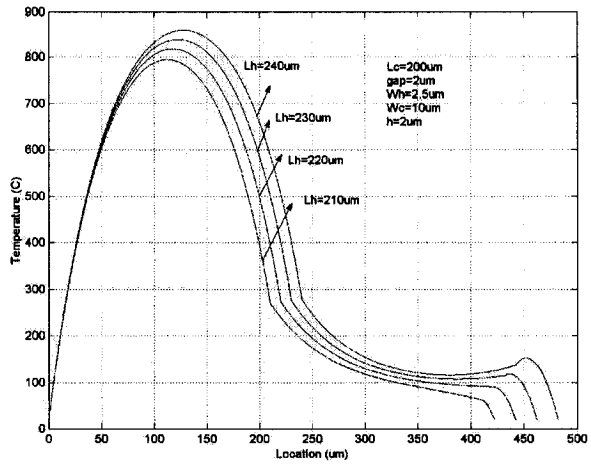

Figure 3-18. (a) Temperature distribution with variation of narrow beam.

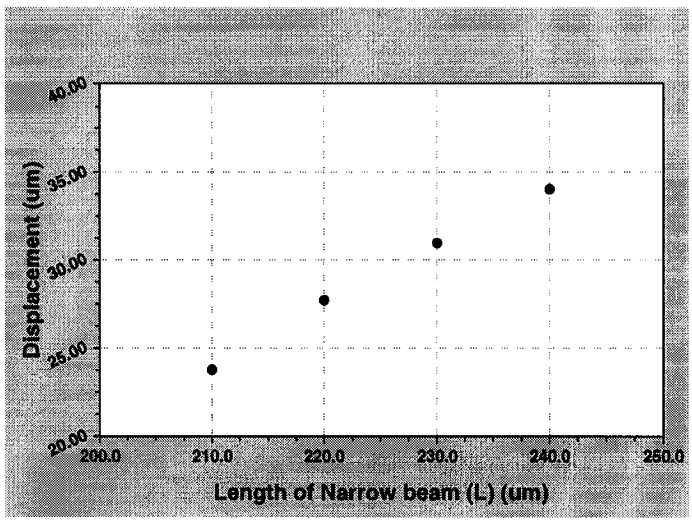

Figure 3-18. (b) Simulated deflection with variation of narrow beam.

(2) In the second analysis, again, all other dimensions were held constant. The width of wide beam is varied. Figure 3-19 shows the temperature and deflection results. Larger direction deflections were achieved for wider wide beam.

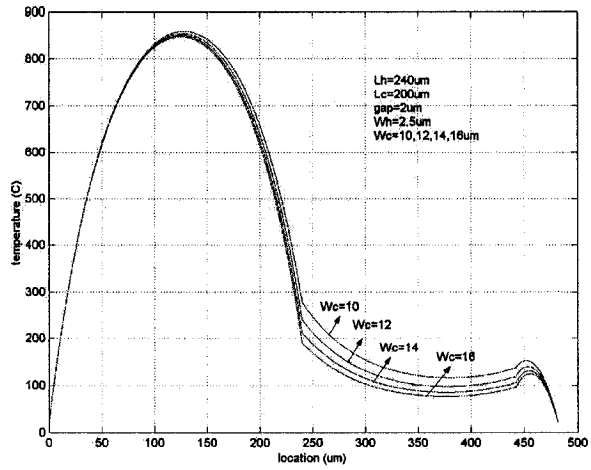

Figure 3-19. (a) Temperature distribution with variation of wide beam.

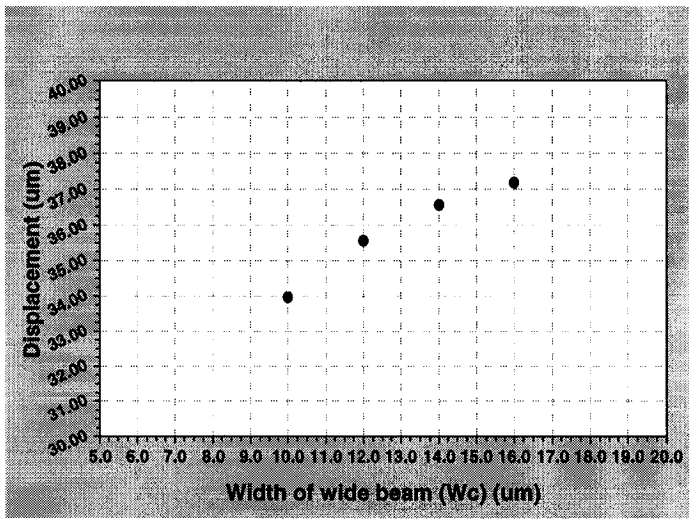

Figure 3-19. (b) Simulated deflection with variation of wide beam.

(3) In the third analysis, all other dimensions were held constant. The gap between narrow beam and wide beam is varied from 2 μm to 8 μm. Figure 3-20 shows the temperature and deflection results of different gap values. Larger direction deflections were achieved by narrower gap.

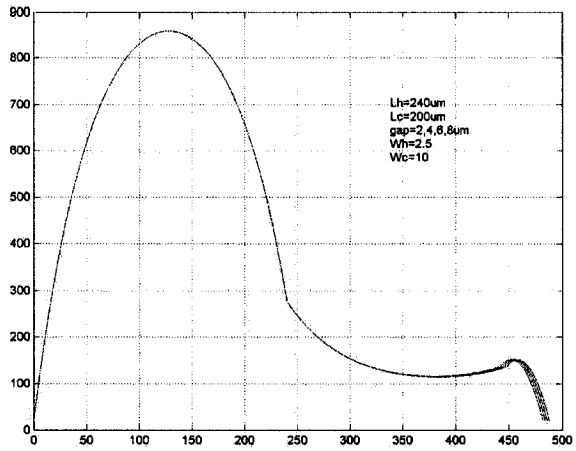

Figure 3-20. (a) Temperature distribution with variation of gap.

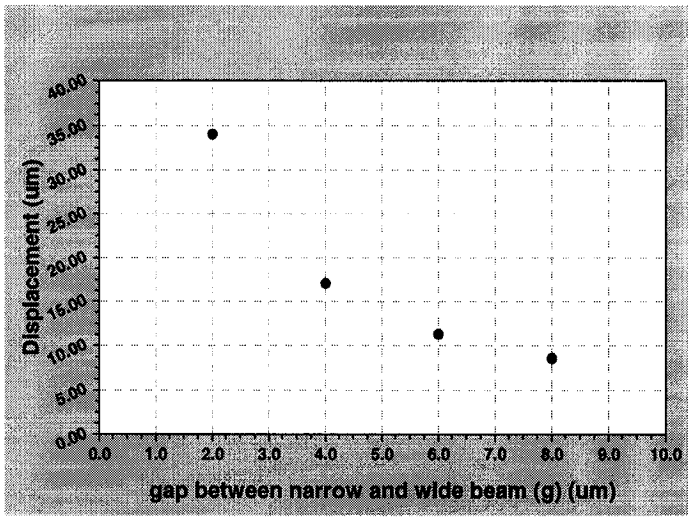

Figure 3-20. (b) Simulated deflection with variation of gap.

(4) In the last analysis, all other dimensions were held constant again. The flexure length is varied from initial value 40 μm to 1 μm to study the approximate optimized flexure length for greatest displacement. Figure 3-21 shows the simulation results of temperature distribution and displacement. From Figure 3-21(a), we can see that: with the flexure length decreases, the flexure and wide beam parts become colder. From Figure 3-21(b), we can find that: for about 20 μm flexure length, we can achieve the

greatest deflection. The explanation of optimized flexure length may be related to the mechanical structure analysis.

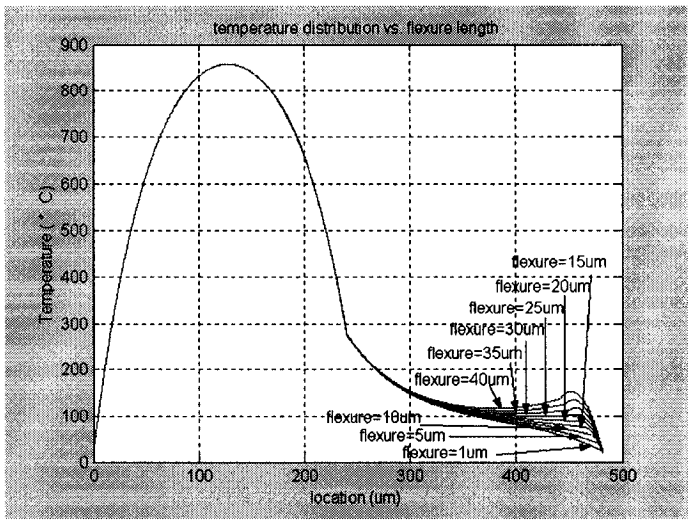

Figure 3-21. (a) Temperature distribution with variation of flexure length.

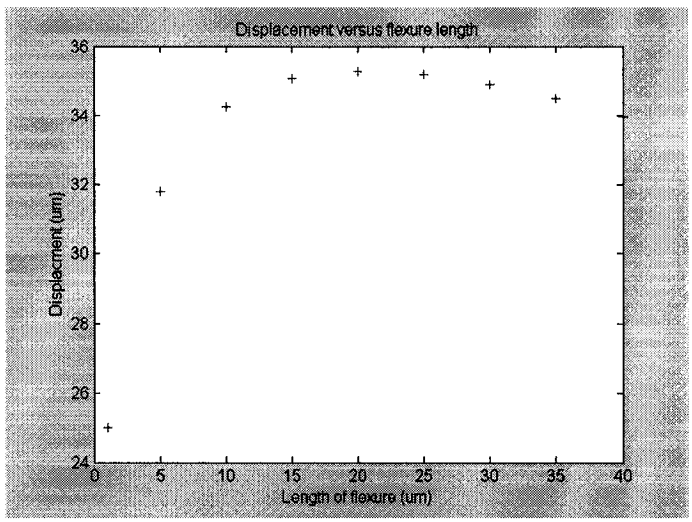

Figure 3-21. (b) Simulated deflection with variation of flexure length.

For uni-directional micro-switches, these analytical results are in agreement with our previous FEM analysis. They illustrated the devices' displacement tendencies change with variations of geometries.

The simulation results of uni-directional micro-switches with variations of geometries are summarized in Table 3.5. Please note that during the analysis: at each time, only one parameter of the geometries is varied, all other dimensions were held constant. And the width of narrow beam is always the same as the width of flexure.

The variables of uni-directional micro-switch used in Table 3.5 are as follows:

L_{total} = Total length (including the length of hot beam, cold beam and flexure)

$L_{flexure}$ = Length of flexure

W_{cold} = Width of cold (wide) beam

W_{gap} = Width of gap (distance between hot beam and cold beam)

Disp= Displacement of uni-directional switch

Table 3.5. The devices performances with variations of geometries

Variable (μm)	Displacement performance tendencies	Ratio of ΔDisp/Δvariable (Deflection variation vs. variable change) (μm/μm)
L_{total}	Longer total length => greater deflection	$Disp/L_{total} \approx 0.2\text{-}0.3$
$L_{flexure}$	Optimized flexure length =>greatest deflection	$Disp/L_{flexure} \approx 0.5$
W_{cold}	Wider cold beam => greater deflection	$Disp/W_{cold} \approx 0.7\text{-}0.8$
W_{gap}	Narrower gap => greater deflection	$Disp/W_{gap} \approx 0.3$

3.1.6.3 Transient Analysis Consideration

It is known that the heat propagates in the direction of decreasing temperature, and the rate of propagation is proportional to the gradient of the temperature. Using the thermal diffusivity of the media K and the temperature T (t, x, y, z), one finds the temperature of the homogeneous media, in Cartesian coordinate system [29]:

$$\frac{\partial T(t,x,y,z)}{\partial t} = k^2 \nabla^2 T(t,x,y,z) \tag{3.22}$$

The so-called one-dimensional heat equation is:

$$\frac{\partial T(t,x)}{\partial t} = k^2 \frac{\partial^2 T(t,x)}{\partial x^2} \tag{3.23}$$

With initial and boundary conditions

$T(t_0,x)=T_t(x)$, $T(t,x_0)=T_0$ and $T(t,x_f)=T_f$.

The analytical solution of heat equation is solved subject to initial and boundary conditions by assuming that both ends (pads) of the microstructure remain at the ambient temperature during the heating process and the microstructure is initially at the ambient temperature before heating. When the initial and boundary conditions turn to: $T(t_0,x)=0$ and $T(t,x_f)=0$. Then the transient solution of temperature distribution is:

$$T(t,x) = \sum_{i=1}^{\infty} B_i \sin\frac{i\pi x}{x_f} e^{-i^2 \frac{k^2 x^2}{x_f^2} t} \tag{3.24}$$

$$B_i = \frac{2}{x_f} \int_{x_0}^{x_f} T_t(x) \sin\frac{i\pi x}{x_f} dx \tag{3.25}$$

The transient solution has been applied to the lineshape microstructures to estimate the transient time. By examining the transient solution, it is found that the slowest transient decay time (i=1) is of the order of 10μs for lineshape microstructures [26].

3.2 Bi-Directional Electro-Thermally Actuated Micro-Switches

3.2.1 Design Introduction

Based on our previous studies on CMOS process and uni-directional micro-switches, a novel bi-directional micro-switch design was presented in this chapter. This novel micro-switch, which offers the possibility of two directional displacements, is designed for CMOS-compatible bulk micromachining. The novel bi-directional micro-switch takes advantage of the features of CMOS process. In CMOS process technology, the silicon dioxide layer is used as structural layer, and the embedded polysilicon layer is used as a heating element. Moreover, during the wet-etching process, the silicon dioxide layer also serves as a mask layer to protect the polysilicon layer from being etched by TMAH.

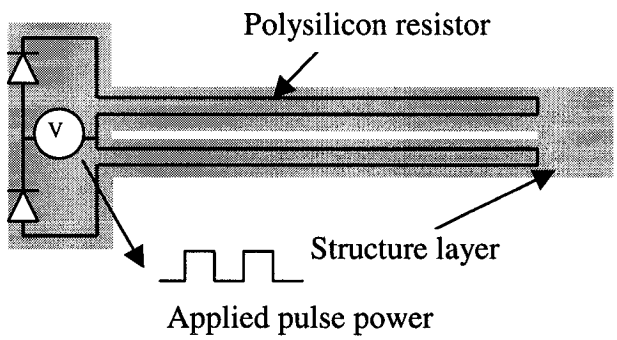

Figure 3-22. Schematic diagram of bi-directional switch (I).

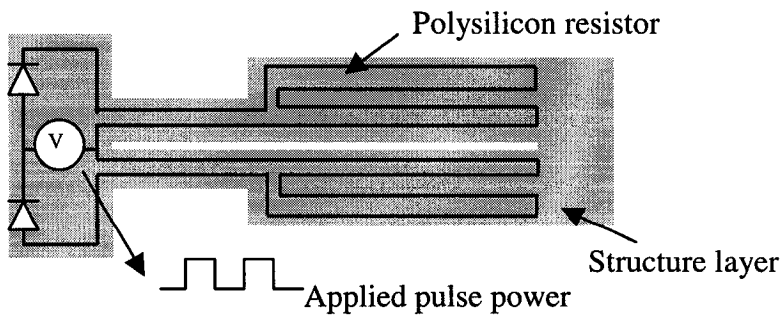

Figure 3-23. Schematic diagram of bi-directional switch (II).

As shown in Figure 3-22 and Figure 3-23, the two beams are identical with embedded polysilicon heating elements, offering the possibility of bi-directional displacement. The anchors are attached to two diodes, one being p-n and the other being n-p. When a common voltage pulse is applied to the diodes, the diodes turn on and off alternately. At any given time, only one junction is "open" to heat a beam and the Joule heating causes the whole structure to deform toward the unheated beam. The deflection of the beams follows the pulse. The speed of the switch depends on the pulse frequency, structural parameters and material properties of the micro-switch. The unique features of CMOS-compatible bulk-micromachining provide the feasibility to realize bi-directional micro devices.

3.2.2 FEM Analysis

The simulation of bi-directional micro-switches would be more complicated than that of the uni-directional micro-switches since there are silicon dioxide structure layer surrounding the polysilicon heating elements. Two designs were considered for this bi-directional deflections purpose. The two-pn junctions control the current flow direction, as a consequence, to control only one polysilicon circuit being "ON". The heat caused by the polysilicon Joule heating transfers from the polysilicon heating element to the structural layer by thermal conduction, and causes the whole structure to deform in the expected direction. Here we just obtain approximate tendencies of device behavior. In order to simplify the analysis to obtain the performance qualitatively, we neglect the oxide structure layer and blade part. In this case, the simulation method of bi-directional micro-switches will be similar to that of the uni-directional micro-switches.

A 2-dimensional analysis was again carried out by ANSYS. The material properties are the same as those used in uni-directional micro-switches. The simulation was divided into two steps: electro-thermal analysis first (using thermal-electric coupled-field element PLANE67) and then followed by thermal-structure analysis (using plane stress element PLANE42). The following figures show the simulation results of two types designs.

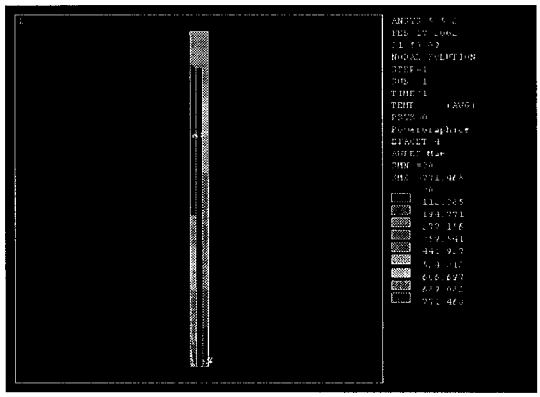

Figure 3-24. The temperature distribution of bi-directional switch (I).

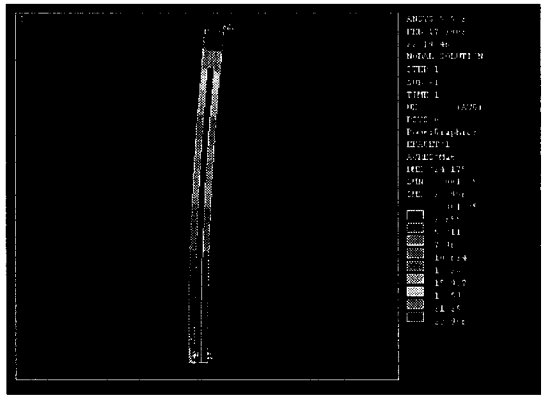

Figure 3-25. The displacement of bi-directional switch (I).

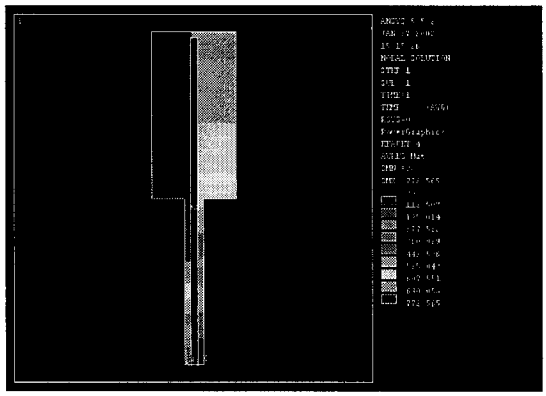

Figure 3-26. The temperature distribution of bi-directional switch (II).

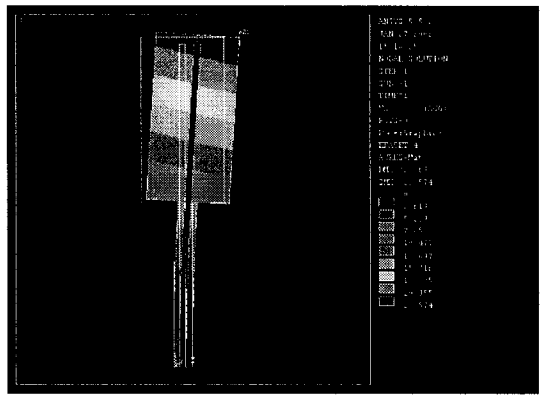

Figure 3-27. The displacement of bi-directional switch (II).

These simulation results show that: at a given time, only one structural beam is heated by Joule heating and other identical beam is unheated. Therefore the switch can deflect to the unheated beam direction.

In this chapter, the designs of uni-directional and bi-directional micro-switches for MUMPs technology and CMOS technology were presented. Both FEM analysis and analytical model were used to analyze the devices' displacement performances.

Chapter 4

CMOS-Compatible Micromachining Post-Processing

4.1 Introduction

In recent years, there has been growing interest in the research and development of integrated MEMS. Various MEMS devices have been fabricated using different foundry technologies. Concurrently, there is also a strong interest in developing MEMS that are compatible with a commercial CMOS process. Compatibility with a commercial CMOS process allows for monolithic integration of analog and digital circuits, which provide signal conditioning, interface control, and wireless remote communication. After receiving the chips from the foundry, the MEMS devices are then released by an additional maskless front-side post-etching process. To realize the MEMS devices at low cost, there are several requirements on the post-etching process. The chemical etchants must be compatible with materials used in the commercial CMOS processes, namely, silicon dioxide, silicon nitride, and exposed aluminum. The etchants must not contaminate the gate dielectrics with impurities such as mobile alkali ions, which shift the flatband voltage and affect the circuits otherwise. Depending on the design, the suspended microstructures can be realized using either an isotropic or anisotropic etch. Commonly used anisotropic etchants are ethylenediamine-pyrocatechol (EDP), tetramethyl-ammonium hydroxide (TMAH), Potassium hydroxide (KOH). Finally, other requirements for these etchants are ease of handling and safety.

Our micro-switches were fabricated by standard CMOS technology: CMOSP35. This technology, manufactured by TSMC and provided through Canadian Microelectronics Corporation (CMC), is a 0.35-micron dual poly, triple metal, polycide CMOS process.

Figure 4-1 shows an example that how the cavity is etched by TMAH and the microstructure is released. The etching takes place over the fast-etching planes.

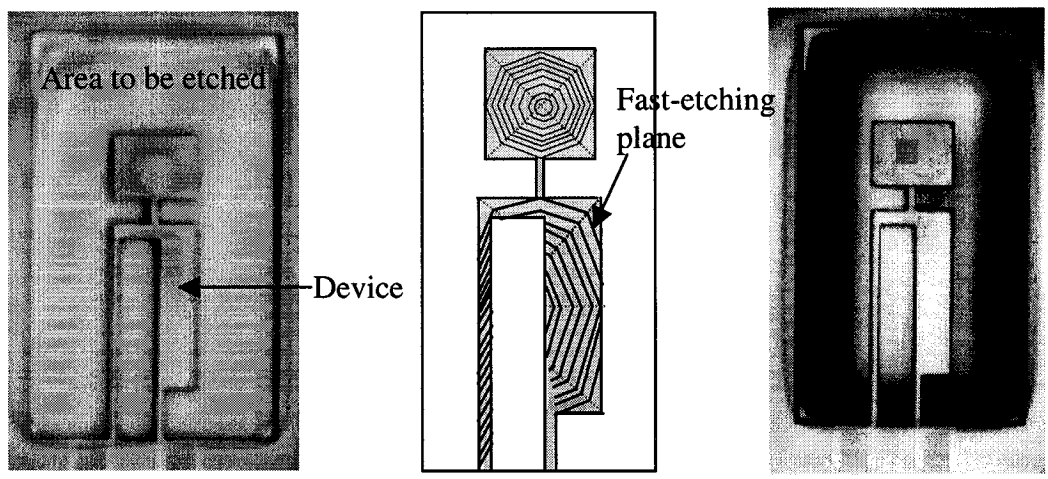

Figure 4-1. (a) Device before post-etching, (b) Fast-etching planes underneath the microstructure, (c) Device after post-etching.

Wet anisotropic etching is done by immersing the sample into a bath of TMAH etchants, at a controlled temperature, perhaps with externally-applied magnetic stirring. Figure 4-2 shows the post-etching bath. The CMOS-compatible TMAH post-etching is carried out in our Lab.

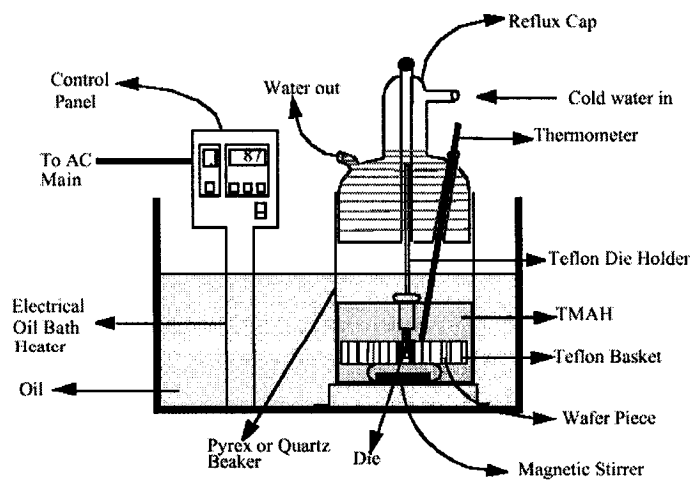

Figure 4-2. Schematic diagram of etch bath.

4.2 Al Pad Layer Passivation Motivation

In our post-etching process, TMAH is chosen as the etchant. TMAH is relatively non-toxic. In contrast to KOH (also relatively no-toxic), there are no alkali metals (K, Na) in TMAH. Such alkali metals are not CMOS-compatible, even if used during post-processing. Microelectronic devices are extremely sensitive to these metallic contaminants, even if exposed to them only at room temperature, since they have non-trivial diffusion rates even at room temperature. One can control etch anisotropy to some extent by varying etchant concentration. The disadvantage of TMAH is that it etches aluminum rapidly (EDP and hydrazine do not). This is a particularly serious nuisance, because the bonding pads in CMOS technology die are made of Al [30].

In our initial experiment (without any Al pad passivation effort), the etching conditions are as follows:

Initial experiment condition:

Etching solution: 25w% TMAH

Etching temperature: 80 °C

The initial experiment was carried out in our Lab using etch station. Figure 4-3 shows the original pad before TMAH post-etching. After one hour etching, the aluminum layer on the pad was etched away and the surface of pad was getting dirty (Figure 4-4). After another 2 hours, we found that there were some cracks on the pad as Figure 4-5 shows and most of devices were fully released. But the devices cannot be bonded and cannot get good electrical conductive contact for these pads even by manipulators.

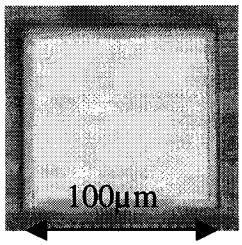

Fig.4-3. Original pad.

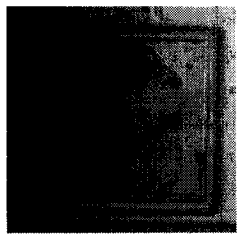

Fig.4-4. Pad after etched for 1 hour.

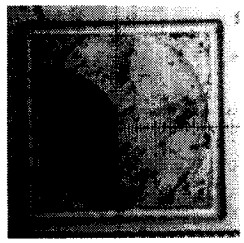

Fig. 4-5. Pad after etched for 3 hours.

The Aluminum protection methods have been addressed previously in [31-34]. In these methods, the additives, such as Silicon powder and silicic acid, are added in the TMAH solution.

4.3 Al Pad Layer Passivation Mechanism

When aluminum is exposed to air, a thin layer of aluminum oxide grows in the surface of aluminum. The main component is amphoteric $Al(OH)_3$, which passivates around neutral pH, and corrodes in alkaline and acidic environments. For alkaline solutions of moderate pH (between 8 and 12) the aluminum is passivated. The reaction of forming aluminate in an alkaline environment is as follows.

$$Al(OH)_3 + OH^- \longleftrightarrow Al(OH)_4^-$$

When the pH of the alkaline solution is decreased, the chemical equilibrium shifts toward the left side, thus reducing the effective aluminum etch rate.

For TMAH solutions, the silicates to provide aluminum passivation can come from dissolved silicon or silicic acid. It works in two ways to provide aluminum passivation. The mechanisms of aluminum passivation are as follows [32]:

1) By dissolve silicon powder or silicic acid, lower the pH value of the solution. The amount of silicon required to form this passivation layer is not great. However the pH must be low to form the passivation layer. It is well known that the hydroxide ion is consumed by the etching reaction. Therefore, the pH of the etching solution decreased with the increasing amount of dissolved silicon. However, if the pH of the TMAH decreases too much by dissolving excess amount of silicon or acid, the etching rate of silicon decreases and the etched surface becomes rough.

2) The effect of the dissolved silicon or silicic acid appears to be a reaction of silicates in solution with $Al(OH)_3$ at the surface of the aluminum. This is thought to form insoluble silicates that passivate the aluminum oxide.

   Furthermore, in the presence of silicates, sparingly soluble pyrophyllite could be formed, according to the following reaction mechanism:

$$2H_2Si_2O_5 + 2Al(OH)_3 \longrightarrow Al_2(OH)_2[Si_2O_5]+4H_2O$$

   These pyrophyllite-type silicates are presumable accountable for passivating the aluminum oxide surface preventing further etching.

4.4 Post-Etching with Additives

4.4.1 Silicon Doping

Since it is undesirable to dissolve excessive amounts of silicon in the etching solution, lower TMAH concentrations are preferable from an aluminum passivation standpoint. Dilute concentrations also provide a higher silicon etch rate.

For our experiments presented in this work, the 5 weight percent solution and the 25 weight percent solution are used. The 5 weight concentration solution was chosen since it

is near the peak etch rate of 2 weight percent concentrations, but the etchant will not be as sensitive to contamination as more dilute solutions. The required amount of dissolved silicon to passivate aluminum at 5 weight percent is 16 grams per liter.

For some applications, the quality of an etched surface may not seem to be an issue. But the hillocks are still a problem, since they expose (111) silicon planes, and significantly reduce the etch rate. The low concentration, however, tends to expose rough surface with hillocks, which will decrease the etch rate greatly. So in some experiments, we choose 25-weight percent solution to reduce hillocks.

The silicon can be added in the form of wafers, or wafer pieces, but these can take several hours to fully dissolve. A more expedient method is to add powdered silicon, which is available is 99.9% purity from Aldrich Chemicals®. Powdered silicon has a much higher surface area than wafer pieces, and dissolves very rapidly. Due to the large amount of hydrogen gas that evolves during this process, foaming and excessive bubbling of the solution can occur. To prevent the solution from foaming over the edge of the etch bath, it is necessary to dissolve the silicon at a relatively low temperature (around 45 °C).

4.4.2 Silicic Acid Doping

Silicon dissolves in TMAH to form silicic acid. It is this silicate that forms a protective layer on exposed aluminum. Instead of silicon, silicic acid ($Si(OH)_4$) can be added to TMAH as an alternative source of silicates . It has been found that the required amount of silicic acid for aluminum passivation is 40 grams per liter for 5 weight percent TMAH. This is a substantially higher quantity than for the added silicon, which is partly due to the lower number of silicon atoms per gram of silicic acid. Since silicic acid is a low-

density powder, the volumes necessary are quite large. There is no apparent advantage to using silicic acid instead of silicon, except that it does not foam when it is dissolved at high temperature. The solution is also somewhat cleaner, since silicon powder leaves an insoluble powdery material at the bottom of the etch bath.

4.4.3 Oxidizers Doping

TMAH solutions with a pH lower than 13 produce very rough etched silicon surfaces, due to the formation of hillocks. These hillocks form due to local pseudomasking of the silicon surface. The exact cause of this micromasking is still unknown, but is likely due to some combination of redeposition of insoluble etch products and formation of bubbles on the etched surface.

When silicon is etched in TMAH, gaseous hydrogen forms as a byproduct. If small bubbles cling to the surface before they release, they temporarily mask the surface underneath from the TMAH. The bubbles block the free diffusion of reactants and products to and from the surface. The length of time it takes a bubble to release is known as the "dwell time". A precipitate forms at the point of contact between the bubble and the silicon that creates a temporary masking layer as it is slowly dissolved upon release of the hydrogen bubble. This localized mask is composed of partially hydrated silicate species. Initially, the number of pyramids at the surface is small, but as etching continues new pyramids are formed and begin to superimpose over previous hillocks. If surface roughness is present to begin with, this process will occur more rapidly, since more nucleation sites are already present.

The formula describes how the hydrogen formed.

$$Si + 2OH^- \longrightarrow Si(OH)_2^{2+} + 4e^-$$

$$Si(OH)_2^{2+} + 4e^- + 4H_2O \longrightarrow Si(OH)_6^{2-} + 2H_2$$

We can use strong oxidizer to eliminate hydrogen. Peroxydisulfate is one of the strongest known oxidizers in aqueous solution. Ammonium peroxydisulfate (also known as ammonium persulfate) ($(NH4)_2S_2O_8$) does not contain alkaline ions, and is therefore CMOS compatible. Ammonium persulfate (AP) is somewhat less stable than the other two, and requires refrigeration to preserve it. Hydrogen peroxide is a strong oxidizer. The reaction

$$2H_2O \longrightarrow 2OH^- + H_2$$

$$H_2O_2 + 2H^+ + 2e^- \longleftrightarrow 2H_2O$$

Ammonium persulfate, when added to silicon doped TMAH solutions, eliminates hillock formation, much as hydrogen peroxide has been shown to do in ammonium hydroxide. The required amount is only 2 to 5 grams per liter of solution.

$$S_2O_8^{2-} + 2e^- \longleftrightarrow 2SO_4^{2-}$$

After some time, hillock formation resumed, which indicates that the oxidizer is consumed in the reaction with silicon. This usually takes about 3 hours for the above concentrations at 85°C. In contrast to hydrogen peroxide, the addition of excess peroxydisulfate does not stop the silicon from etching. When ammonium persulfate is added to silicon-doped TMAH solutions, a white precipitate forms. This is probably due to a reaction between the oxidizer and the silicates in solution. The precipitate dissolves after about 20 minutes.

4.5 Al Protection Experiments

Five Al passivation experiments with individual etching condition were designed in schematic diagram in Figure 4-6.

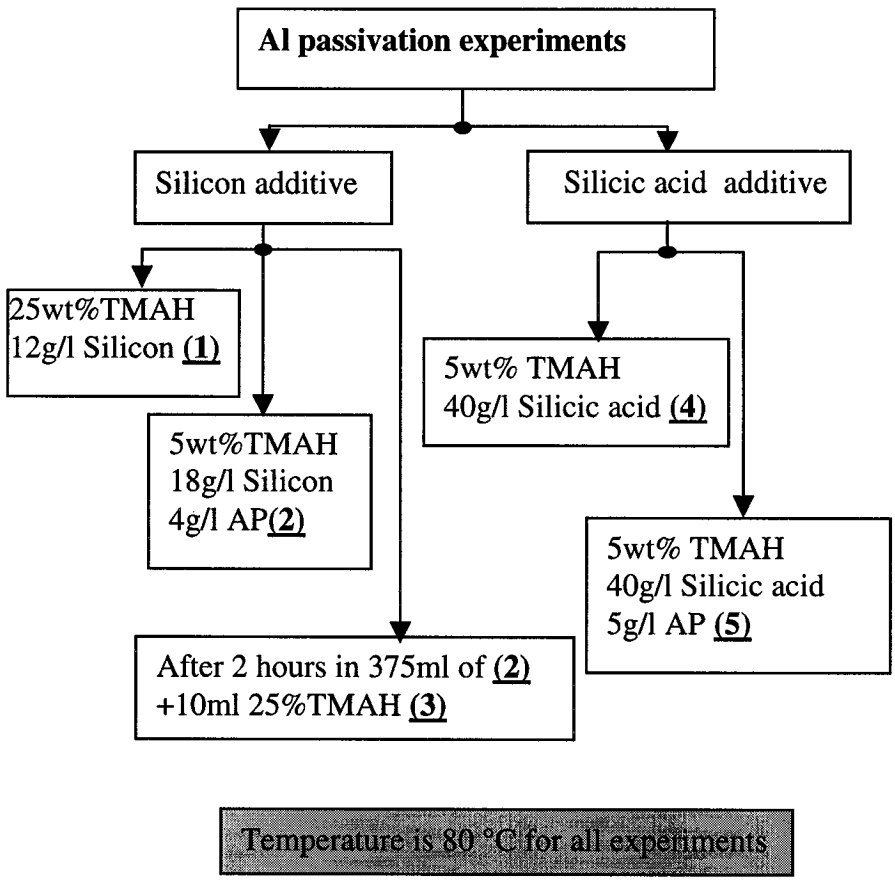

Figure 4-6. Schematic diagram of experiments design.

(1) Experiment 1

Etching condition:

- Solution: 25wt% TMAH + 3 gram/liter silicon powder
- Temperature: 80 °C

In experiment 1, the aluminum is etched away in half an hour. However, the pads do not crack, and exposed the underneath titanium nitride layer. The titanium nitride layer is

also a good conductive layer. The devices can be fully released in 3-4 hours. Compare the pads with those in initial experiment, it is nice and clean (Figure 4-7), what is more, the metal on the shutter part was protected while the metal on shutter in initial experiment is etched. One of the released devices in this experiment is given in Figure 4-8.

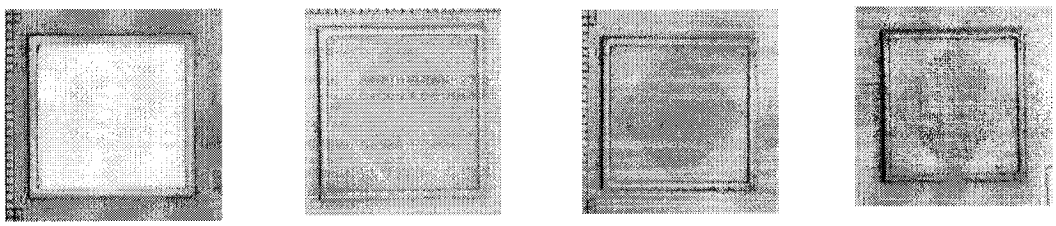

(a) (b) (c) (d)

Figure 4-7. Al pad in different etching periods, (a) original pad (b) After 1 hour, (c) After 2 hours, (d) After 3 hours.

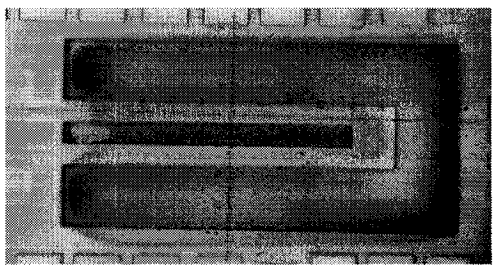

Figure 4-8. Released device in Al passivation experiment 1.

(2) Experiment 2

Etching condition:

- Solution: 1.5wt%TMAH + 18g/l Silicon + 4g/l AP
- Temperature: 80°C

During this experiment, the pad pictures for different etch time were recorded. After 3 hours, we achieve aluminum protection result clearly. We can find the bright and beautiful aluminum layer even after etching for 3 hours (Figure 4-9). We also put some test wafer sample in solution. The sample is a bipolar transistor made in our lab. Due to

the experiment condition, the aluminum layer has appeared some dots and speckles. We put the test sample in the solution for 10 hours and the aluminum is still on the surface (Figure 4-10). However, the etch rate of silicon is very slow. In initial experiment and experiment 1, we can find the fast-etching plane in half an hour. But in experiment 2, even after one hour, there is no fast-etching plane appearing. After etched for 3 hours, the cavity bottom is still full of hillocks and we cannot observe fast-etching planes.

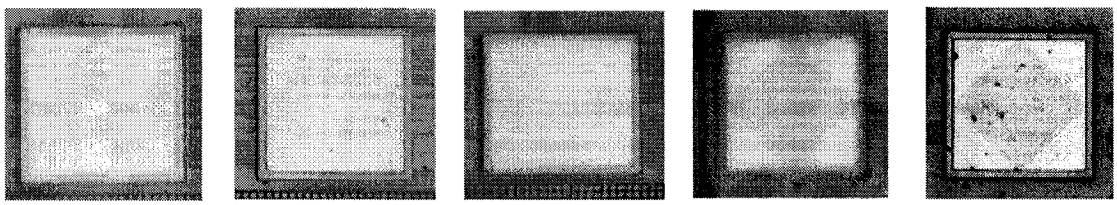

(a) (b) (c) (d) (e)

Figure 4-9. Al pad in different etching period: (a) Original pad (b) After 0.5 hour (c) After 1 hour (d) After 2 hours (e) After 3 hours.

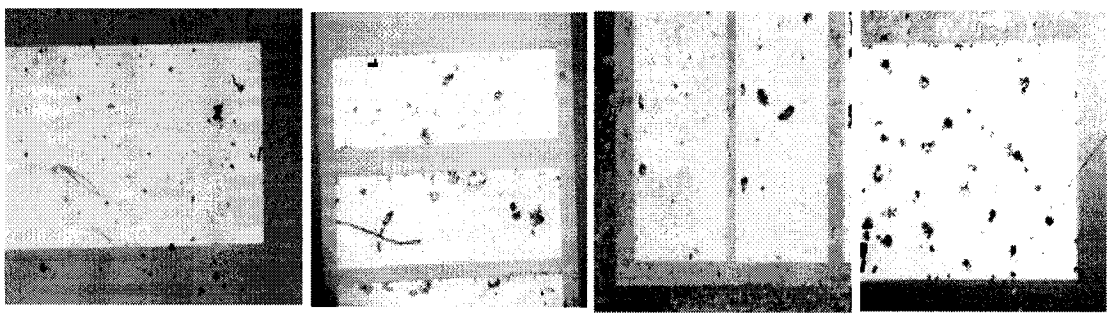

(a) (b) (c) (d)

Figure 4-10. Al test sample in different etching period: (a) Original pad (b) After 1 hour (c) After 2 hours (d) After 10 hours.

(3) Experiment 3

Etching condition:

- Solution: After 2 hours in 375ml of solution (2) + adding 10ml 25%TMAH
- Temperature: 80 °C

The device is etched in the same solution for 2 hours and the aluminum is still on the surface. Then we added 10ml 25%TMAH into the solution, and etched for half an hour in this new solution, the aluminum layer was etched away, exposed the layer underneath Al, titanium nitride (Figure 4-11). But the etch rate of silicon increases. Under the microscope, the fast-etching planes are exposed as shown in Figure 4-12. The reason is that: after adding new TAMH, the concentration is higher, which leads to more smooth surface, though the etch rate tends to decrease in high concentration. In first part of this experiment, hillocks dominate, after adding TMAH, the higher concentration remove hillocks a little thus increases the etch rate. The etch rate cannot be comparable to experiment 1 due to the hillocks, though it is faster than the etch rate in experiment 2.

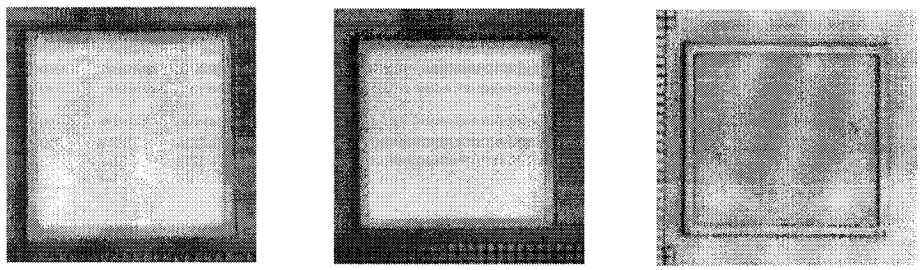

(a) (b) (c)

Figure 4-11. Al pad in different etching period: (a) Original pad (b) After 2 hours (c) After 0.5 hour in solution (3).

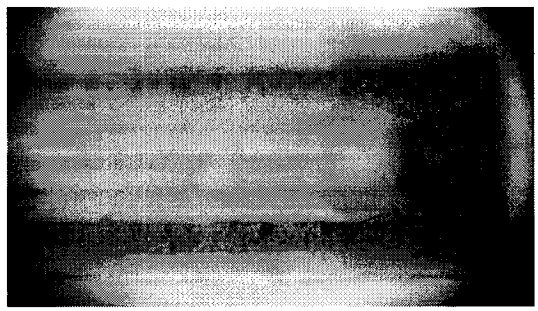

Figure 4-12. Fast-etching plane after adding TMAH for 0.5 hour.

(4) Experiment 4

Etching condition:

- Solution: 5wt%TMAH+40g/l Silicic acid
- Temperature: 80 °C

Instead of silicon, silicic acid $Si(OH)_4$ can be added to TMAH solution as an alternative source of silicates. Figure 4-13 shows the experiment results after 2 hours etching.

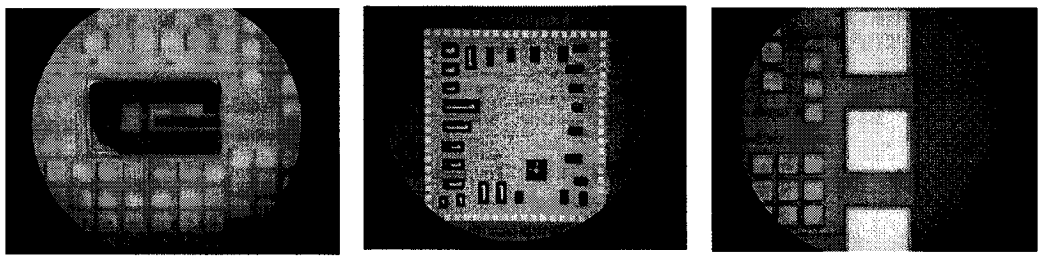

(a) (b) (c)

Figure 4-13. (a) Device cavity etching, (b) Top view of chip layout, (c) Al pad.

In this experiment, Al pads are protected, too. But the etch rate of silicon is slow.

(5) Experiment 5

Etching condition:

- 5wt% TMAH + 40g/l Silicic acid + 5g/l AP
- Temperature: 80 °C

The difference between experiment 5 and 4 is adding AP as oxidizer to prevent hillocks.

Figure 4-14 shows the experiment results after 2 hours etching

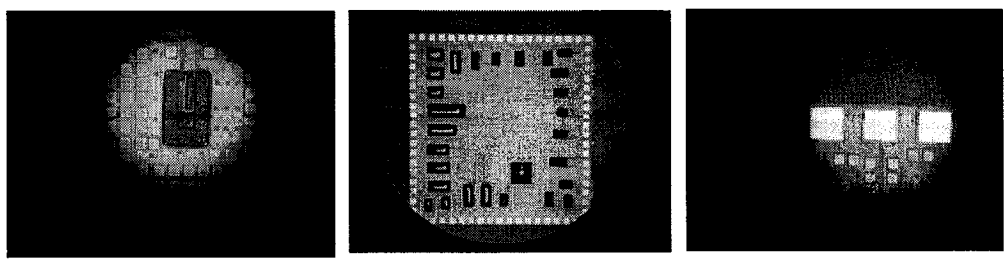

(a) (b) (c)

Figure 4-14. (a) Device cavity etching, (b) Top view of chip layout, (c) Al pad.

In experiment 5, the Al pads are also kept, and etch rate of silicon is just a little faster than that of experiment 4.

4.6 Experimental Results and Discussions

These pictures in Figure 4-15 are the Al pads after 1 hour etching in the five different experiments. We can find that the Al pads in experiment 2, 4 and 5 are well protected. However, in experiment 1, the first layer, aluminum, was etched away and exposed the second layer, titanium nitride which is also a good conductive layer. In experiment 3, in the first two hours, the aluminum is protected. But after adding new TMAH and etched for half an hour, the aluminum layer is etched away.

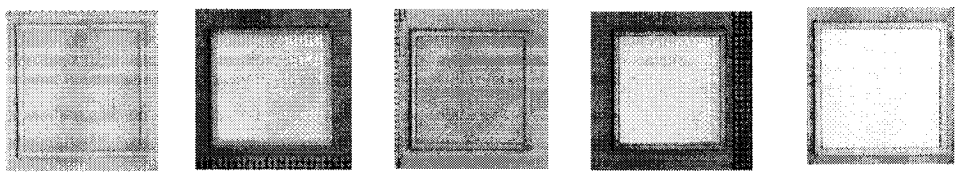

(a) (b) (c) (d) (e)

Figure 4-15. Al pad in (a) Exp.1 (b) Exp.2 (c) Exp.3 (d) Exp.4 (e) Exp. 5.

The five experiments conditions are as follows and the performance results are summarized in Table 4.1.

Experiment #1: 25wt%TMAH 12g/l Silicon

Experiment #2: 5wt%TMAH 18g/l Silicon + 4g/l AP

Experiment #3: After 2 hours in 375ml of Exp. (2) +10ml 25%TMAH

Experiment #4: 5wt% TMAH 40g/l Silicic acid

Experiment #5: 5wt% TMAH 40g/l Silicic acid + 5g/l AP

Table 4.1. Pad passivation experiments results

No. of Exp.	Pad protection	Contact ability	Si etch rate
Exp. (1)	Al layer gone, TiN layer keep	Good	Fast
Exp. (2)	Al layer left	Good	Slow
Exp. (3)	Al layer gone, TiN layer keep	Good	Relative fast
Exp. (4)	Al layer left	Good	Slow
Exp. (5)	Al layer left	Good	Slow

The fully released devices from Al passivation experiment 1 are given in Figure 4-16 and Figure 4-17. Most of devices in this work were released in the condition of experiment 1.

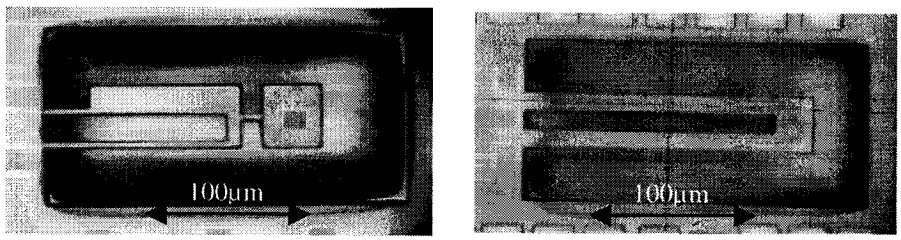

(a) (b)

Figure 4-16. (a) Uni-direction micro-switch, (b) Bi-directional micro-switch.

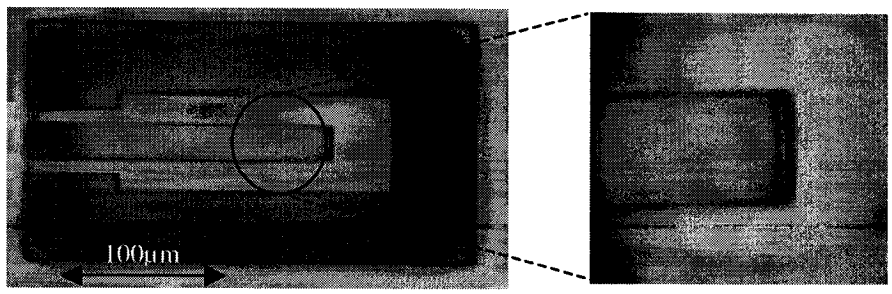

Figure 4-17. Micro-switches after TMAH released & Magnification view of embedded polysilicon resistors.

Researchers at University of Alberta has reported that using 5wt% TMAH with 44g/l silicic acid doping with persulfate $K_2S_2O_8$ (potassium persulfate) as the oxidizer, they can achieve the etch rate of (100) at 80 °C is about 0.9μm/min. there was no visible gas formation on the exposed silicon, and etched (100) surface is fairly smooth [35]. For their combinational etching, TMAH anisotropic etching only takes 30-50 minutes to release their cantilever device. But for longer etching times, such as etching time of our micro-switches, the depletion effects have to be considered. In his work, when the TMAH was significantly doped with silicic acid, it etches silicon slowly. The pH value is about 12.5. In fact, the solution is in some kind of balanced stated, a "window" states. After about 1 hour etching, due to the depletion of the TMAH and oxidizer from the solution, the solution begins to exhibit a lower (100) etch rate with rough etched surfaces and bubble formation. To maintain smooth etched surface and the (100) etch rate, 5ml/L 25 wt% TMAH and 3g/L potassium persulfate should be added into the solution every 30 minutes to compensate for the depletion which is very similar to our passivation experiment #5. It can be seen that the control for the amount of new adding TMAH is a very important. It has to be chosen at a "balance" amount which can passivate the Al and keep reasonable silicon etch rate.

4.7 Silicon Dioxide Layer Etching

As we mentioned in previous chapter, the micro-switch fabricated by the CMOSP35 technology has polysilicon heating element surrounded by silicon dioxide layer. After device released by TMAH, we used HF to remove the surrounded oxide layer to study the

stress of polysilicon beam and properties of structural layer. After 2 minutes dipping in HF solution, some of devices bended down to the bottom of cavity (Figure 4-18).

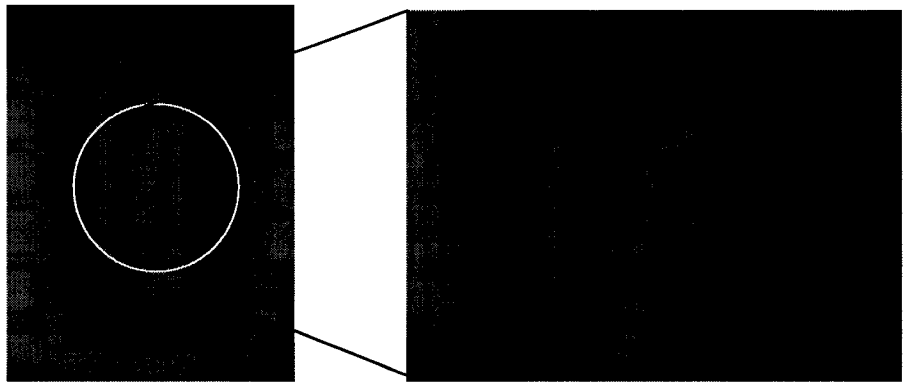

Figure 4-18. Device bends to cavity bottom after 2 minutes etching in HF solution.

During the CMOS-compatible bulk micromachining, the internal stresses of each film must be considered. The control of the internal stresses of a thin film is important for the fabrication of micro-electro-mechanical structures. The microelectronic fabrication industry typically grows/deposits polysilicon, silicon nitride, and silicon dioxide films with recipes that minimize time. Unfortunately, a deposition process which is optimized to speed, does not always create a low internal stress film. In fact, most of these films have internal stresses which are highly compressive. This is more likely the reason that some devices would bend toward the bottom of the cavity when the oxide layer was etched away. Comparison of same device before and after oxide layer being etched is given in Figure 4-19. After oxide layer was etched away, the polysilicon structure bent toward the bottom of cavity. The SEM pictures in Figure 4-20 show the details of oxide layer "peeling off".

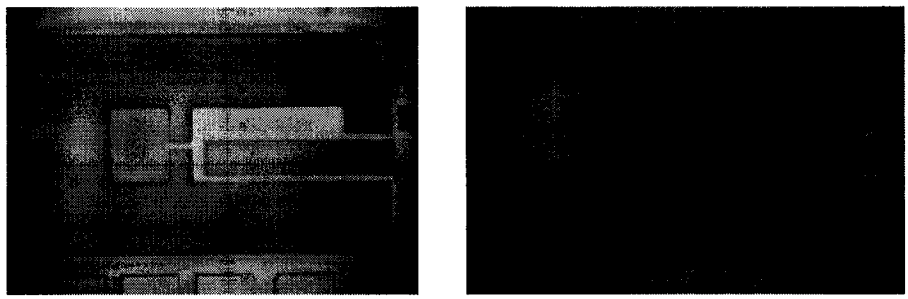

(a) (b)

Figure 4-19. (a) Device with oxide structural layer, (b) Device after oxide layer etched.

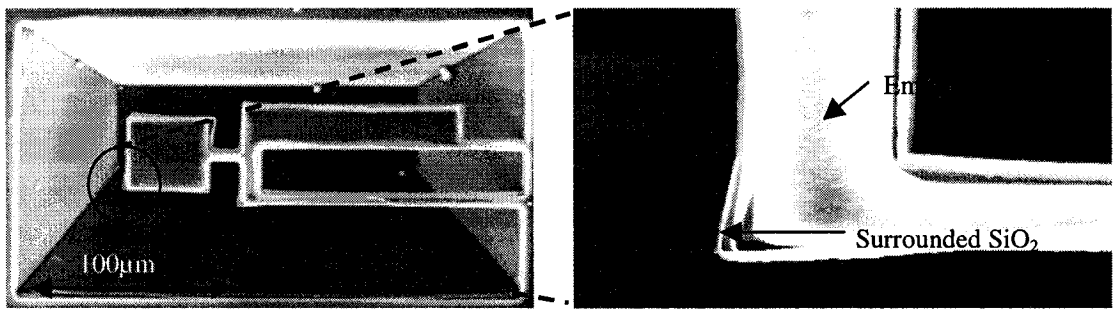

Figure 4-20. SEM pictures of device after 2 minutes in HF solution.

In this oxide layer etching experiment, first, device was put in 49% HF solution for 2 minutes; the oxide layer was etched away a little bit. The freestanding polysilicon structure buckles (as shown in Figure 4-18, Figure 4-19 and Figure 4-20). Then, after the device was continued to dip into the 49% HF solution for another 5 minutes, the oxide layer was completely etched away. The whole structure falls down toward the bottom of cavity since the supported flexure and narrow beam became "weak" without surrounded oxide layer. All the silicon dioxide layers are gone and only poly beams were left. All the uni-directional devices were seriously deformed and fallen down to the cavity bottom (Figure 4-21), and for bi-directional devices, only polysilicon heating elements were left as Figure 4-22 shows.

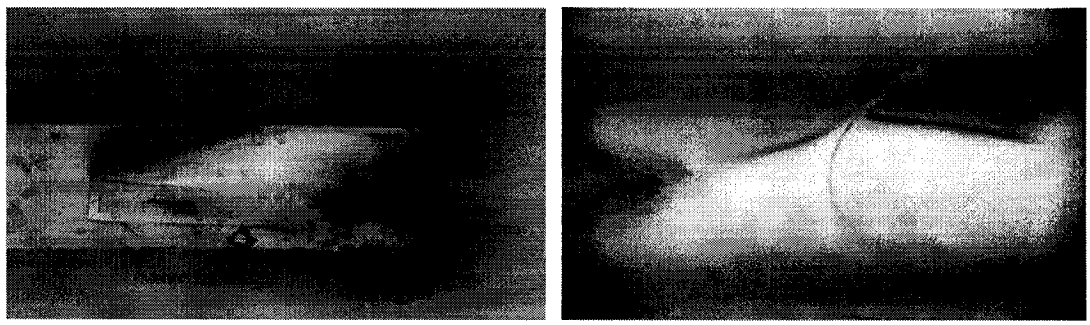

Figure 4-21. Two uni-directional devices after oxide layer completely etched.

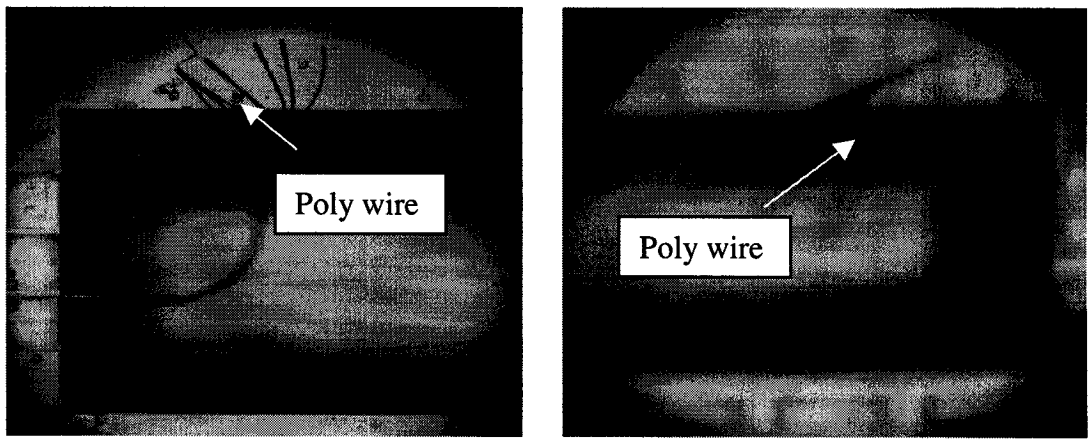

Figure 4-22. Two bi-directional devices after oxide layer completely etched.

Chapter 5

Experimental Measurements, Observations and Discussions

5.1 Experimental Setup

The experimental apparatus is composed of probe station, power supply, digital multimeter and function generator. Figure 5-1 illustrates the probe station used in these experiments. The probe station with scale in eyepiece, is used to measure the displacement of the devices. Power supply is applied to heat the devices and generate the displacement. Voltage and current across the devices are recorded by digital multimeter. The test chip is put on the probe station stage, therefore, the heat conduction from the chip substrate to the stage of probe station is effective and it is assumed that the temperature of the substrate remains constant at room temperature during the experiment.

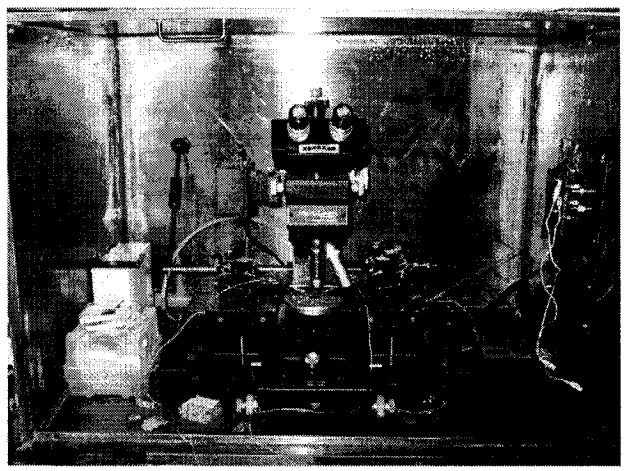

Figure 5-1. Experimental setup at probe station.

The Figure 5-2 shows an example of the device fabricated by MUMPs technology in the original (OFF) position without applied power and deflected (ON) position with applied power. With the attached ruler scale, the deflection can be observed quantitatively.

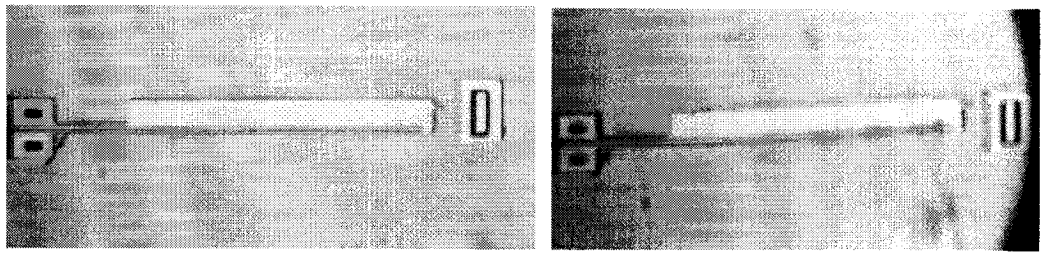

(a) (b)

Figure 5-2. (a) Device in "OFF" position (b) device in "ON" position.

5.2 Displacement Measurements of Devices from MUMPs Technology

As mentioned in previous chapters, the release of devices fabricated by MUMPs technology is performed by immersing the chip in a bath of 49% HF (room temperature). Figure 5-3 shows a released microstructure and magnified view for parts of this microstructure after sacrificial oxide release.

(a) (b) (c)

Figure 5-3. (a) SEM of a released device from MUMPs technology, (b) Magnification view for scale ruler part, (c) Magnification view for part of device.

5.2.1 Devices Made from POLY2 Layer

Figure 5-4 shows device made from only the POLY2 layer (1.5μm thick). When power is applied to this device, a dark region appears in the narrow beam. With increasing input power, the dark region increases along the narrow beam. Very small lateral deflection can be seen. The possible reasons for this behavior are: first, the device is not fully released.

In order to investigate the etching result, the microstructure made from POLY2 layer was removed; we found some small dark regions and spots underneath the POLY2 layer. These regions are the areas which were not released during HF etching. Second, the POLY2 structure layer is only 1.5μm thick, and the in-plane thermal actuator made from thin structure layer is most likely to cause the side effect of lateral deflection, the out-of-plane deflection, while applying input power [11].

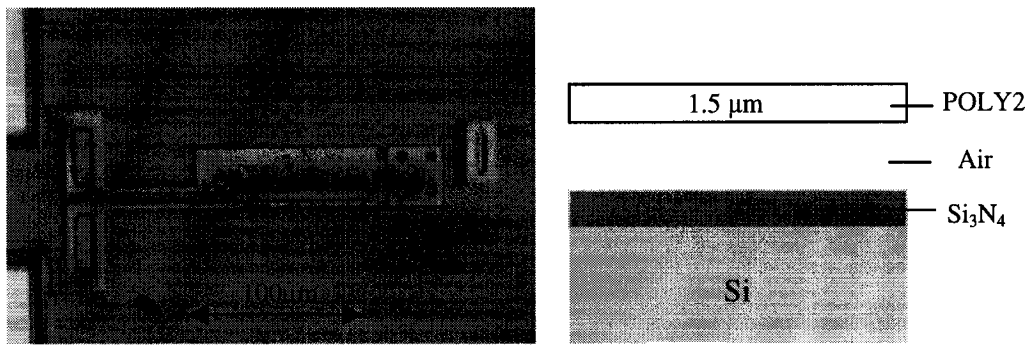

Figure 5-4. (a) Device made from POLY2, (b) schematic view of device cross-section.

5.2.2 Devices Made from POLY1 Layer

The POLY1 layer is 2 μm thick (which is 0.5 μm thicker than POLY2 layer). The device in Figure 5-5 is made from POLY1 layer. The experimental deflection results are given in Figure 5-6.

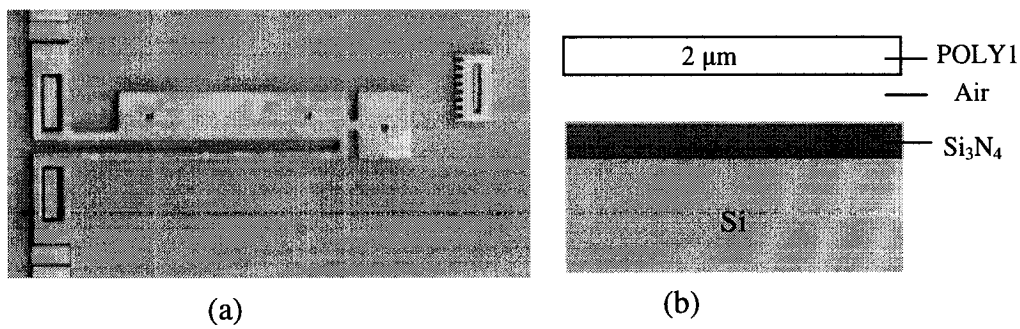

Figure 5-5. (a) Device made from POLY1, (b) schematic view of device cross-section.

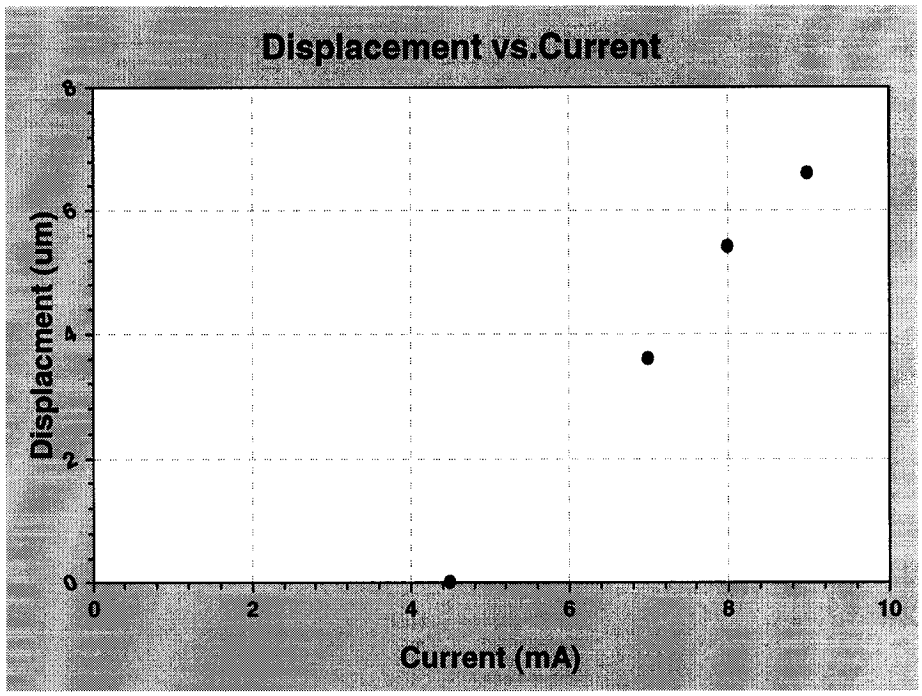

Figure 5-6. Experimental result of device made from POLY1 layer.

For this design, we also compared the experimental data with analytical results. The displacement results of the device in Figure 5-5 are given in Figure 5-7. The experimental data and simulation data are in agreement at lower temperature. But at high temperature, they begin to show a difference. This is because that the thermal analysis for the micro-switches considered only heat conduction in the microstructure, without including the thermal radiation. However, at higher power, heat loss due to the thermal radiation may become significant. Especially, the heat radiative transfer from the hot arm to the cold one may give rise to increase of the cold arm temperature. Therefore it causes the discrepancy between experimental results and simulation results at high input power.

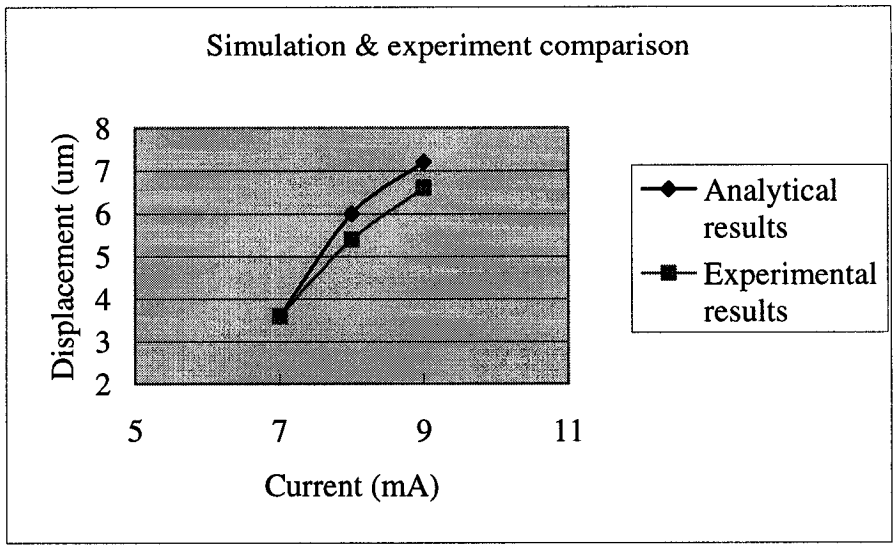

Figure 5-7. Displacement vs. current: comparison of experimental and simulation results.

5.2.3 Devices Made from POLY1 and POLY2 Layers

In the MUMPs process technology, a technique has been developed for producing polysilicon parts made of both POLY1 and POLY2 layer (Figure 5-8). This technique makes the final stacked structure is indistinguishable from a single 3.5 μm polysilicon layer.

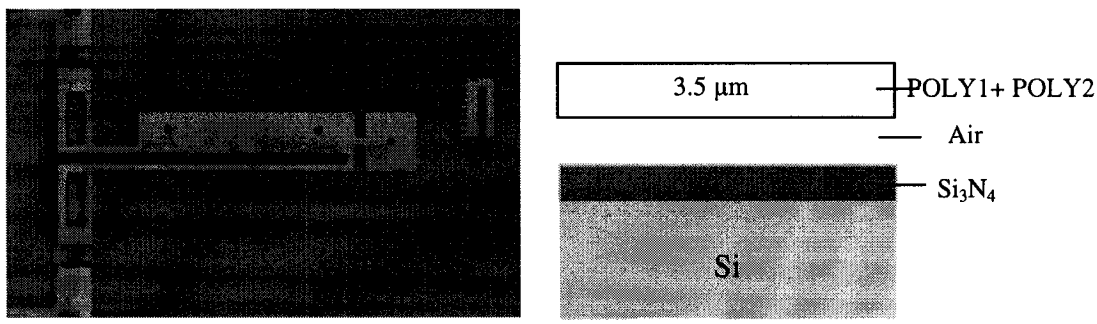

Figure 5-8. (a) Device made from POLY1 and POLY2, (b) schematic view of device cross-section.

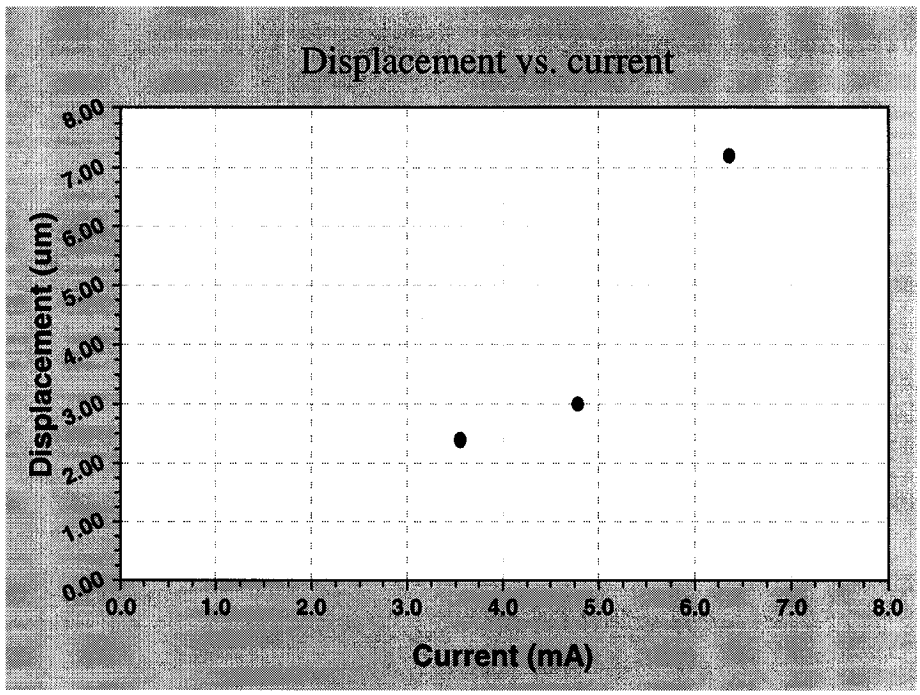

Figure 5-9. Experimental results of the device made from POLY1 and POLY2 layers.

The displacement results of this double thickness device (Figure 5-8) are given in Figure 5-9. The key advantage of this double thickness structure is that: it can improve the lateral deflection performance of devices.

5.2.4 Devices with Serpentine Spring Flexure

The devices with serpentine spring flexures were also fabricated by MUMPs technology (Figure 5-10). The experimental results of these devices are given in Figure 5-11.

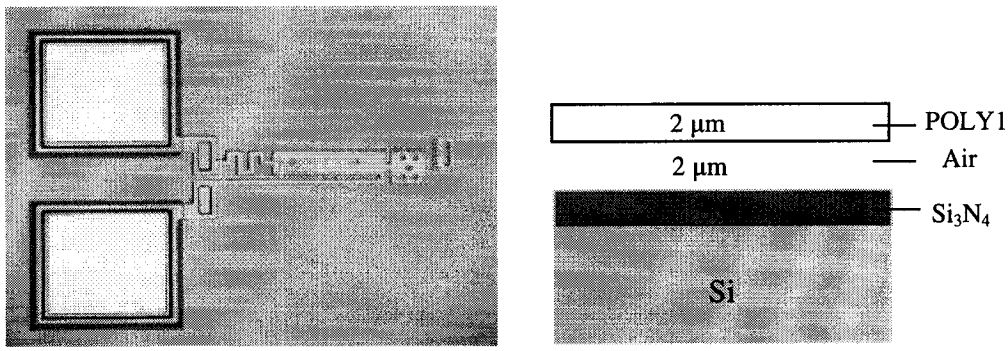

(a) (b)

Figure 5-10. (a) Device with serpentine spring flexure, (b) schematic view of device cross-section.

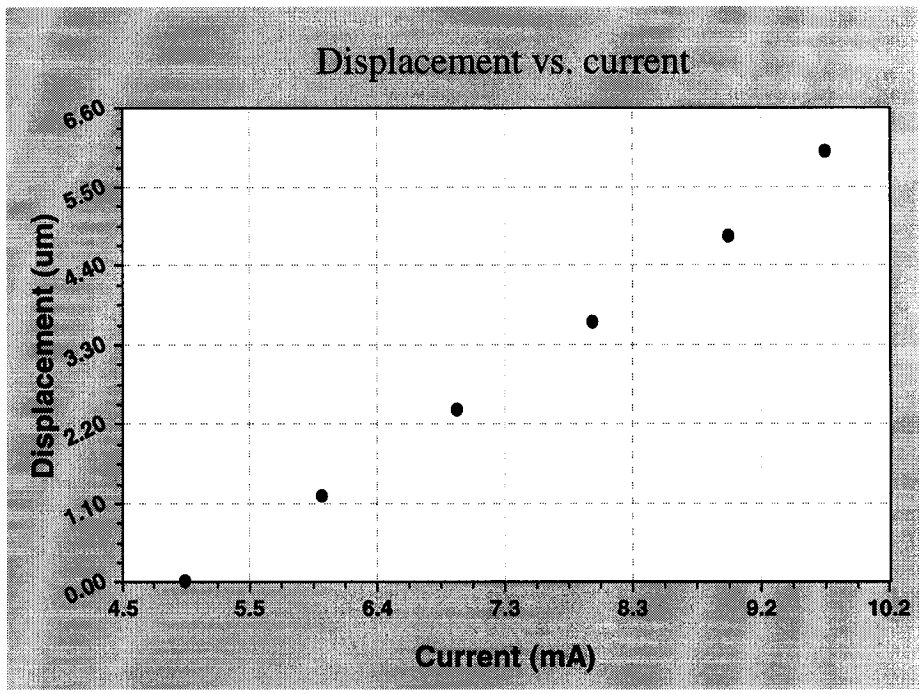

Figure 5-11. Experimental results of device with serpentine spring flexure.

As described in Chapter 3, the spring constant is a function of the number of meanders (odd and even number) and design variables (a, b and c). Therefore this new design can offer the possibility to reduce the spring constant and increase the deflection.

5.2.5 Devices with Two Hot Arms

The experimental results of the device with two hot arms (Figure 5-12) are given in Figure 5-13.

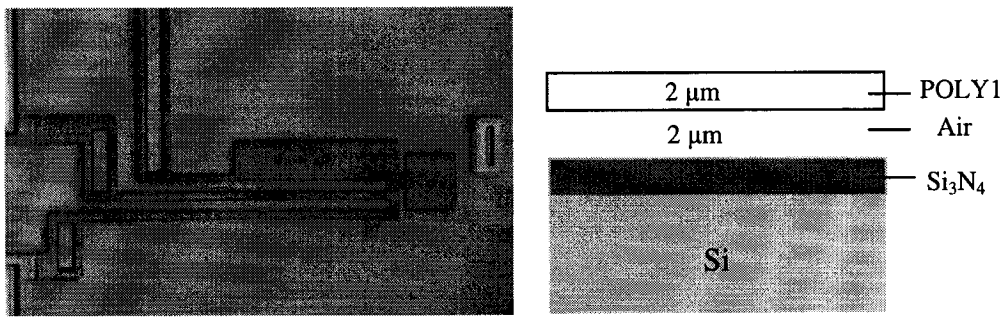

(a) (b)

Figure 5-12. (a) Device with two hot arms, (b) Schematic view of device cross-section.

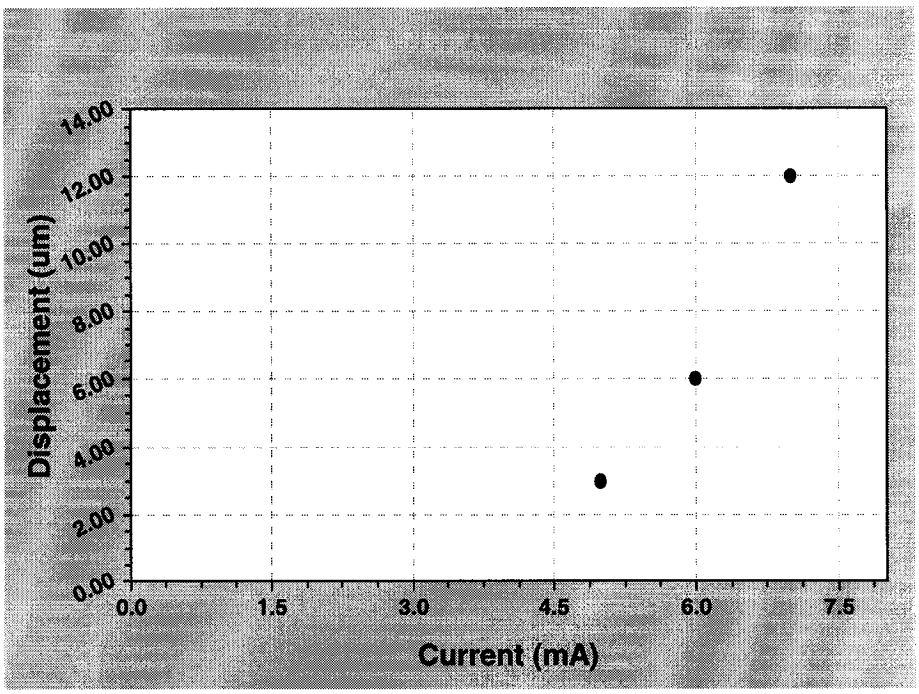

Figure 5-13. Experimental results of device with two hot arms.

In this two-hot arm thermal actuator, the electric current only passes through the outer and inner hot arms. This avoids the cold arm and flexure being part of the electric circuit.

It dramatically increases the efficiency since all the power consumed in the actuator contributes to the deflection of the thermal actuator tip. The flexure can also be thinner than the hot arm because no current passes through the flexure. Obviously, compared with the traditional U-shaped folded beam, the two-hot arm thermal actuator has improved the displacement.

The experimental results of different designs are summarized in Table 5.1.

Table 5.1 Summary of experimental results for different designs

	Original resistance & length of structure (except the shutter part)	Device performance
Device with POLY1+POLY2 as wide beam, POLY2 as narrow beam.	R=9.5 KΩ Length= 200μm	No visible displacement is observed. (The microstructure was most likely not fully released)
Device with POLY2 layer only	R=410 Ω Length= 200μm	No displacement of whole structure, only narrow beam deform.
Device with POLY1 layer only	R=470 Ω Length= 200μm	Medium range displacement. (6.5 μm at 9mA)
Device with POLY1 and POLY2 layers	R=350 Ω Length= 200μm	Medium range displacement, but avoid the out-of-plane deflection. (7 μm at 6.5 mA)
Device with serpentine springs flexure	R=430 Ω Length= 200μm	Medium range displacement, provide the more design flexibility (6 μm at 9.5 mA)
Device with 2-hot arm	R=820 Ω Length= 200μm	Relatively large displacement. Design area is relatively big. (12 μm at 7 mA)

5.3 Displacement Measurements of Devices from CMOS Technology

The schematic diagram in Figure 5-14 shows the cross-section view of device fabricated by CMOS-compatible micromachining. The devices are released by TMAH wet etching. Compared with the devices made from MUMPs process, there is a thin layer of silicon dioxide surrounding the polysilicon structure. Figure 5-15 and Figure 5-16 are SEM pictures of released devices.

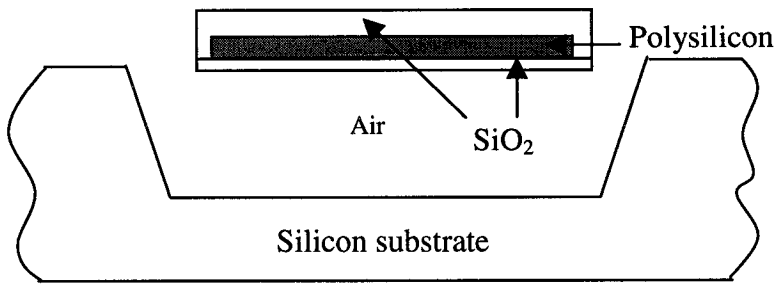

Figure 5-14. Schematic cross-section view of device from CMOS process.

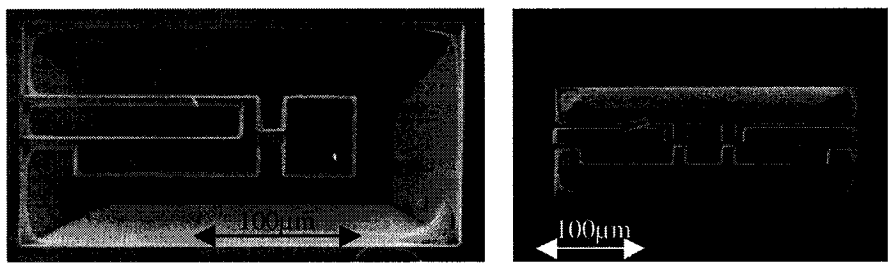

(a) (b)

Figure 5-15. (a) SEM of uni-directional micro-switch (I),
(b) SEM of uni-directional micro-switch (II).

For the two uni-directional micro-switches, the design (II) has almost the same displacement as that of design (I), but it provides larger force than that of design (II).

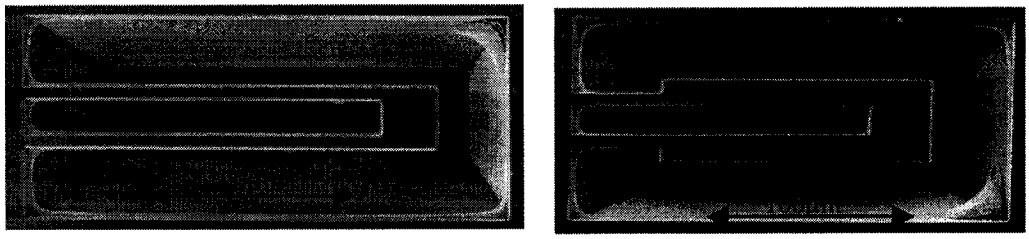

(a) (b)

Figure 5-16. (a) SEM of Bi-directional micro-switches (I),
(b) SEM of Bi-directional micro-switches (II).

The experimental data of these devices are given in Figure 5-17. From previous FEM analysis and analytical model, we can conclude that wider cold beam and longer total length, narrower gap can achieve larger deflection. The displacements of devices with different geometrical designs were measured to verify the previous FEM analysis and analytical modeling.

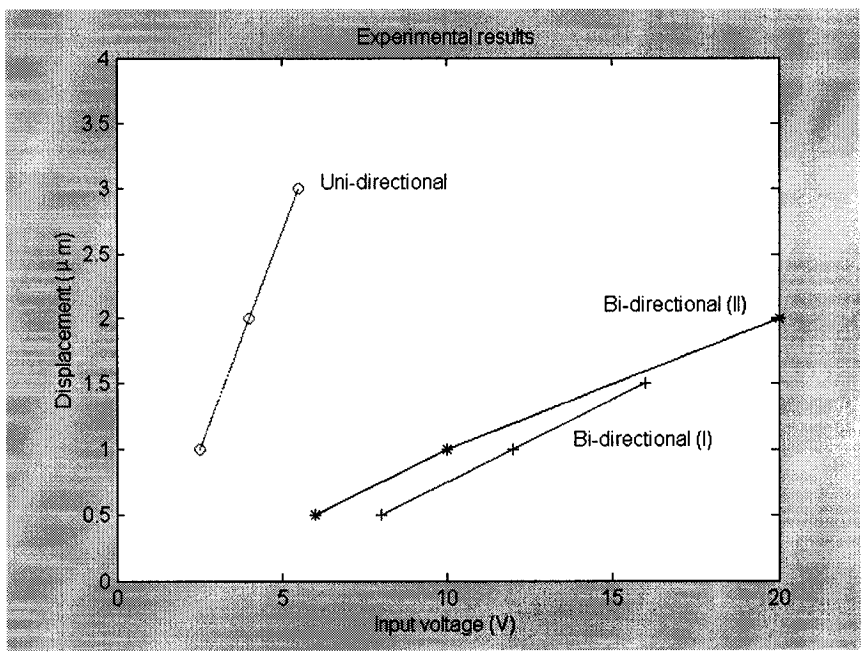

Figure 5-17. Experimental results of displacement for uni-directional device (I), Bi-directional devices (I) & (II).

5.4 Switching Time Measurements

The switching time is also an important specification for micro-switch. In this thesis, we introduced a visual technique to measure the switching time of the micro-switch and examine the time and frequency response characteristics of the uni-directional micro-switches.

The visual technique, in which vibrating movement is observed under high magnification (by optical microscope), is used to characterize the switching time. The function generator is applied to actuate the electro-thermal switches. The voltage range of the function generator is set to 0 to 4 volts and the initial frequency was set at 1Hz. The device in Figure 5-3, fabricated by MUMPs technology, is used as an example to measure the switching time. At first, the device would travel from original "OFF" position to deformed position "ON", back and forth according to the excitation frequency (starting at 1Hz). As the frequency is increased slowly, it is observed that: at first, the device can follow the frequency and vibrates from "ON" to "OFF" and "OFF" to "ON" as described in Figure 5-18. However, when the frequency increases further, the switch only vibrates a little around the deformed "ON" position (Figure 5-19). If the frequency is further increased to a certain value, we can observe that; the switch cannot heat or cool fast enough and it deflects to a fixed position (which is roughly in the "ON" position according to the visual observation). The approximate threshold at which the actuation no longer responds is about 10Hz.

Figure 5-20 shows the vibration distance from "ON" position (deflection position) to "OFF" position (zero-deflection position) with variable frequency.

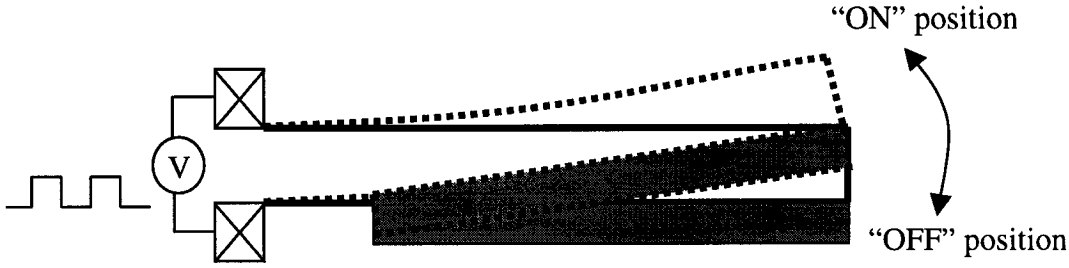

Figure 5-18. At "low" frequency, the device vibrates between "OFF" and "ON" position. Solid line is device in original "OFF" position and dash line is device in deformed "ON" position.

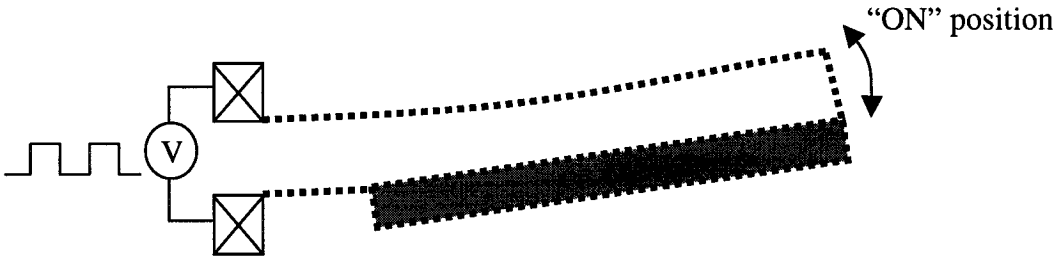

Figure 5-19. After "certain" frequency, the device only "stays" around the deformed "ON" position instead of vibrating between "ON" and "OFF" Position.

When the function generator was applied to the device, at high frequencies the micro-switch cannot heat or cool fast enough. The frequency limitation is due to the thermal material properties, such as thermal mass and thermal conductivity. Also the response times of this micro devices scale with size; the smaller the switch is made, the faster it will respond.

Microstructures of these sizes and dimensions have resonance frequencies in the 30-70 kHz range. At applied frequencies below the mechanical resonance, the microstructure system is dominated by the first-order thermal response [36].

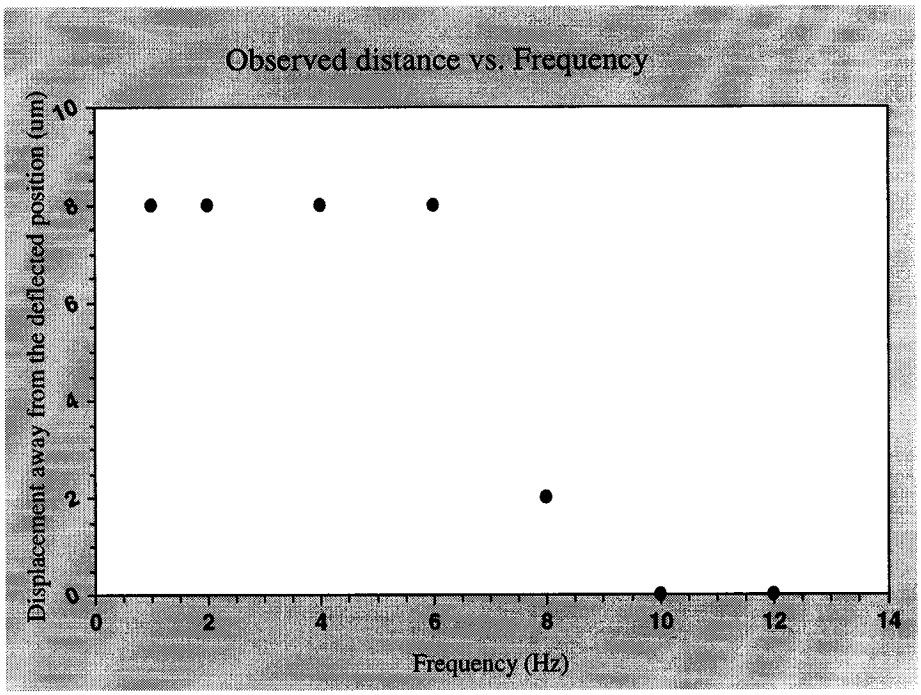

Figure 5-20. The vibration distance (which is away from "ON" position) versus the variable frequency.

For the uni-directional micro-switches fabricated in MUMPs technology, the thermal threshold frequencies are roughly in 10-100 Hz range.

5.5 Device Buckling Phenomenon

During our experiments, in order to investigate the physical effects of the microstructures, the devices were tested in an extreme condition (in our device case, the input power is continuously increased until the maximum value which the device is really hot in narrow beam and nearly broken). At these experiments, some interesting phenomena were observed. One is the back-bending phenomenon from micro-switches fabricated by MUMPs process as Figure 5-21 shows.

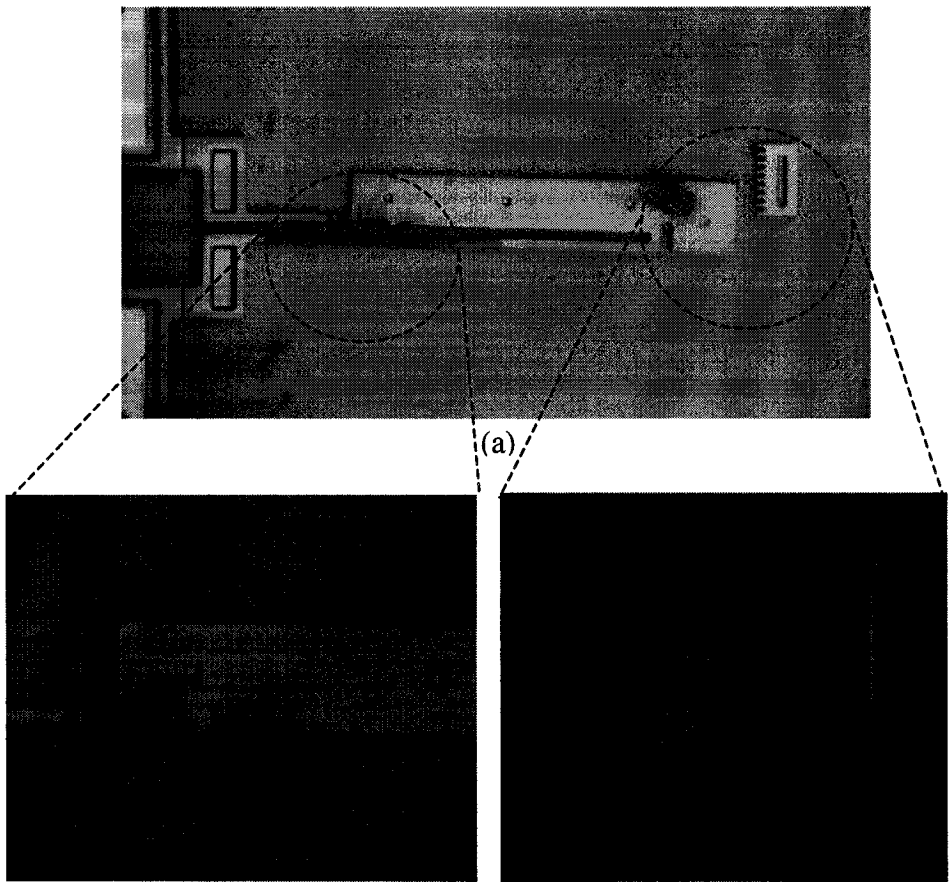

Figure 5-21. (a) After applying current higher than "critical" value and turning off the power, the micro-switch is back bending. (b) & (c) Magnification views, dark region implies the physical damage.

Normally, when input power is applied to the electro-thermally actuated polysilicon micro-switch, the device will deform toward the wide beam direction. And when the power is off, the device will move back to its original position. And the switching states between "ON" and "OFF" work well for about 3 hours cycles in our test. But with the current increasing to a "critical" value, a very brightly glowing portion of the narrow beam can be seen (critical temperature in narrow beam). We noticed that: after we switch off input power, the device will revert back "over" the original position (zero-deflection position) and sometimes shape of narrow beam can change from the straight beam to the

curved shape beam (Figure 5-22) and can not recover to straight beam again. Obviously, the beams changed from elastic buckling to plastic bucking. To estimate the critical temperature of the brightly glowing, hot zone in the narrow beam, a test beam with gold (Au) film coating on top of the beam is used to verify the brightly "glowing" beam temperature. When the input power is applied to the test beam, the glowing, hot region can be seen in the middle of the beam and Au film is melted away. Au melting point is about 1064 °C, thereby the temperature of the brightly glowing color zone somewhat can be estimated to be around 1000 °C if we assume that there is not reaction happened to Au in atmosphere.

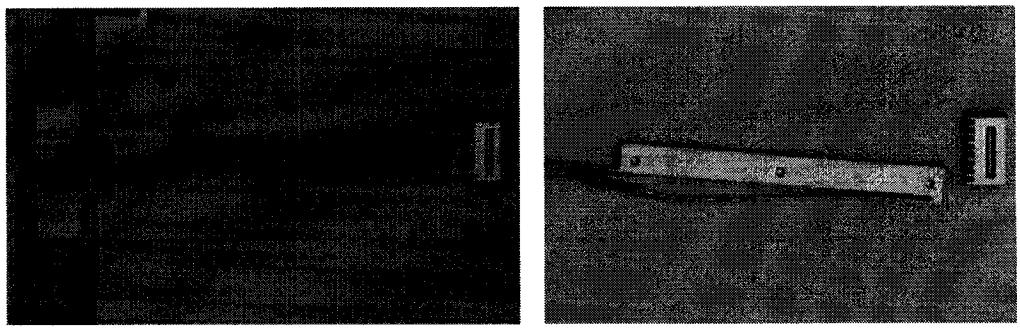

(a) (b)

Figure 5-22. (a) Micro-switch in original "off" position, and (b) After applying current higher than "critical" value and turning off the input power, switch is back bending and has a curved shape beam.

The back-bending phenomenon that we had observed here is possibly related to the compressive stress of microstructure. When both high stress and temperature change are involved, such creep-like behavior may occur and affect the reliability of MEMS devices. Several MEMS structures that may have great chance in encountering this problem include thermally driven microactuators [37–39], chemical sensors that operate at elevated temperature [40] and micro turbines [41]. Therefore, it is important to

investigate the buckling phenomena in the microscale for reliable operation of these and other MEMS devices.

The micro-switches are fabricated from the MUMPs Process. A residual, compressive stress of approximately 10 MPa exists after the completion of the microfabrication process [19]. The gap between the bottom of the POLY1 micro beam and substrate is 2μm. When a constant input current is supplied at or above a threshold value, electro-thermally induced buckling occurs. Two types of material behaviors: the pure elastic buckling and the combination of melting and irreversible plastic damage are reported in this work.

5.5.1 Elastic Buckling

When the micro device was applied a constant current smaller than "critical" value and no bright, glowing portion observed at the narrow beam. An expected tip displacement is observed immediately upon the application of the constant current. The current supply is cut off and the beam reverts back to its original shape as shown in Figure 5-23. No sign of observable structural deterioration or permanent plastic deformation can be found. It can therefore be deduced that the beam buckles in the elastic regime without sustaining observable physical damage.

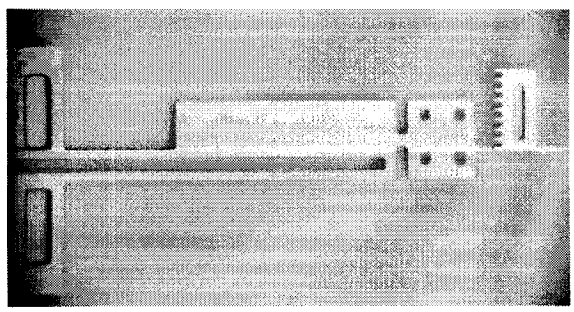

Figure 5-23. Micro-switch in original "OFF" position after cut off the power.

5.5.2 Permanent Plastic Damage

When the input current is increasing until higher than a threshold value, the highest temperature is attained at the middle of the narrow beam from a heat transfer standpoint, this region experiences the greatest extent of damage. During the testing period, the center portion of the beam glows brightly as Figure 5-24 shows, indicating that the temperature can be around 900°C -1000 °C (as we described in the test beam).

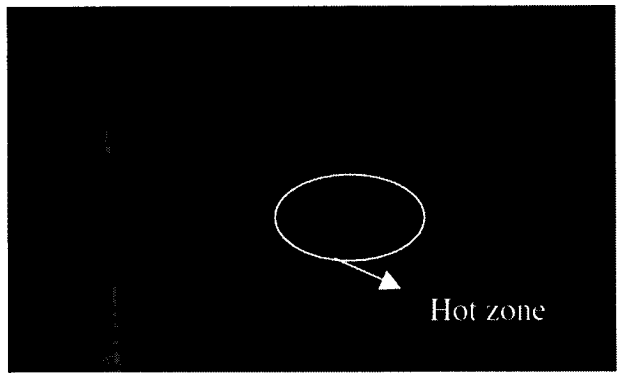

Figure 5-24. The hot region at narrow beam under applied power.

When temperature of polysilicon beam is above 900 °C, localized melting and hence drastic change in material property can therefore be expected [42]. The damaged areas, represented by the dark portions, are shown in the narrow beam. As the input power is continuously increasing, the narrow beam will crack and devices are broken (Figure 5-25). The generation of cracks on the narrow beam is the reason for the fault and degradation of the micro devices. The polysilicon structures generate the crack before the polysilicon beam reaches the melting point of polysilicon.

Compared with the devices made by polysilicon, the devices made by the crystalline silicon demonstrate another interesting fault mechanism. Author has also recorded the phenomenon of crystalline silicon beam breakdown during previous study for [11] in

Figure 5-26. When the input power is continuously increasing, some parts of crystalline silicon beam melt away at high temperature instead of generating cracks as polysilicon.

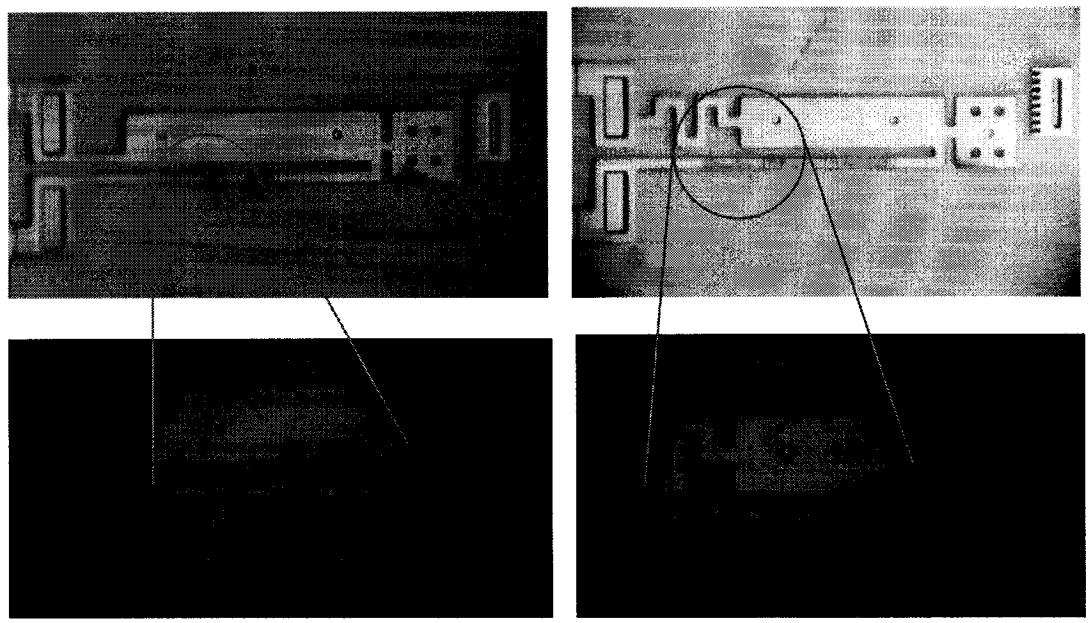

Figure 5-25. Polysilicon broken beams (cracks can be seen at narrow beam) and magnification view.

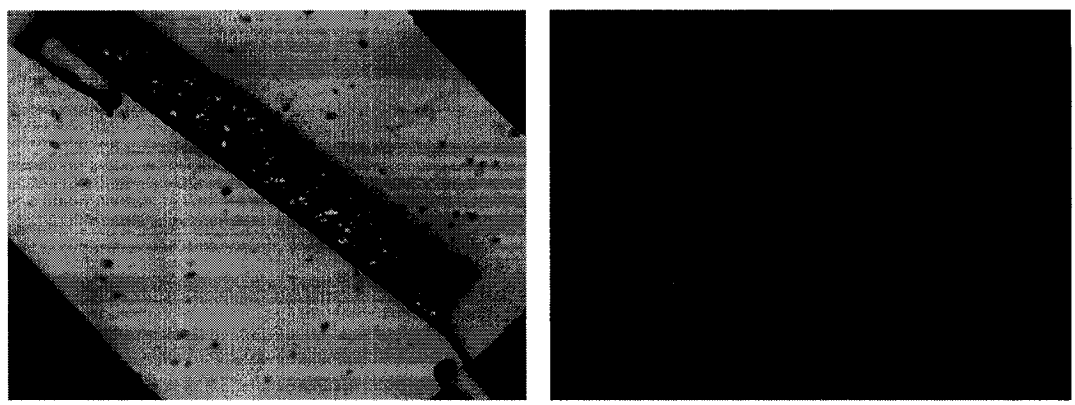

Figure 5-26. Two melted single-crystal silicon micro beams.

5.6 Polysilicon Resistance Behavior at High Temperature

Polycrystalline silicon is commonly used in integrated circuits (ICs), MEMS and microsensors. The performance and reliability of micro devices are strongly influenced by heat conduction. To effectively design, operate and analyze the electro-thermally

actuated micro devices, it is critical to know the temperature-dependent material properties, such as electrical resistivity. Two kinds of experiments were performed: (1) the temperature dependent resistance behavior; (2) irreversible resistance variations when temperature is raised and lowered.

The experimental apparatus is composed of probe station, power supply and digital multi-meters. The power supply is applied to heat the micro device and generate the thermal deflection. Voltages and currents across the devices are recorded to compute the resistances. The dissipated power in the micro-switch is found using the relations

$$P = VI \tag{5.1}$$

V and I are the voltage and current across the device.

For the temperature-dependent resistance study, the experimental measurement results are given in Figure 5-27. In this experiment, the input power is used as an approximate indicator for the temperature.

In order to roughly estimate the temperature for each input power, the temperature dependence of the polysilicon heater resistance, $R(T)= R_0[1+ \xi(T-Ts)]$, was used in the analysis. Here, R_0 is the resistance at room temperature, and ξ is the temperature coefficient of resistance (TCR) of polysilicon. The heating temperature is T. The TCR was used as 1.25×10^{-3} $°C^{-1}$ from [13]. Then the temperature, T, and thermal isolation, G, of the microstructure were calculated as

$$T = T_s + (\frac{R(T)}{R_0} - 1)/\xi \tag{5.2}$$

$$G = \frac{T}{P} \tag{5.3}$$

The electro-thermal properties of CMOS-based microstructures similar to these switches have been investigated in [43], and the thermal isolation was found to be in the range of 50K/mW. This quantity will not change as dramatically as polysilicon resistance and TCR (which are electrical properties, sensitively dependent on polysilicon grains, dopant concentration and dopant distribution). So for this analysis, we assume that the thermal isolation is relatively constant over the temperature range in these experiments. The thermal isolation of the polysilicon microstructure fabricated by MUMPs technology is calculated from Figure 5-27, Equation (5.2) and Equation (5.3), to be about 5 K/mW. The reason for the different thermal isolations of polysilicon microstructures made from different processes is that: The devices made in the CMOS process are likely to have higher thermal isolation (for roughly the same microstructure shape), because of the deeper cavity and oxide surrounding the heat-dissipating polysilicon (which is likely to reduce radiation).

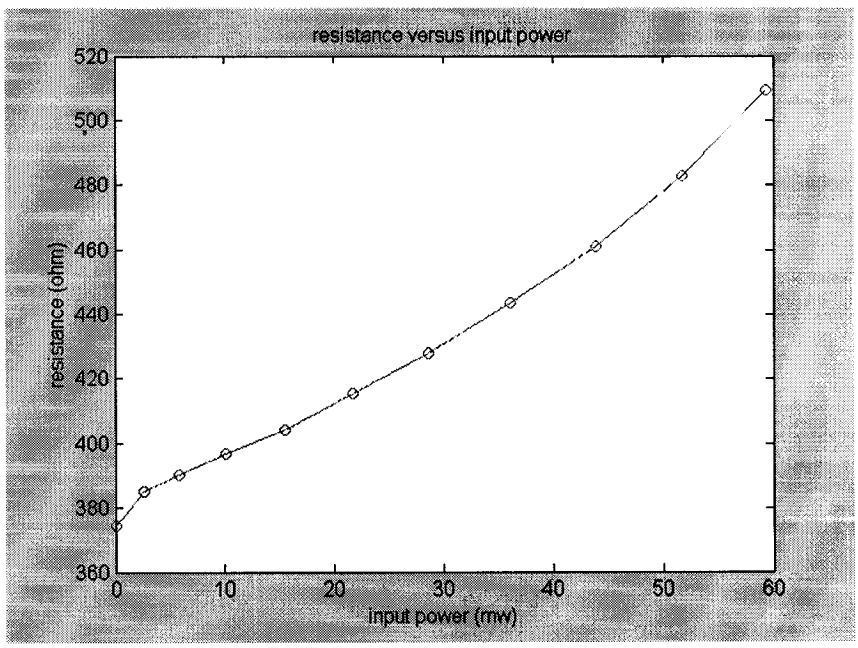

Figure 5-27. The experimental resistance versus input power.

The Figure 5-28 shows the calculated temperature variation with the input power based on Equation (5.2) and (5.3). As the applied power is increased up to about 60 mW, T increases roughly linearly.

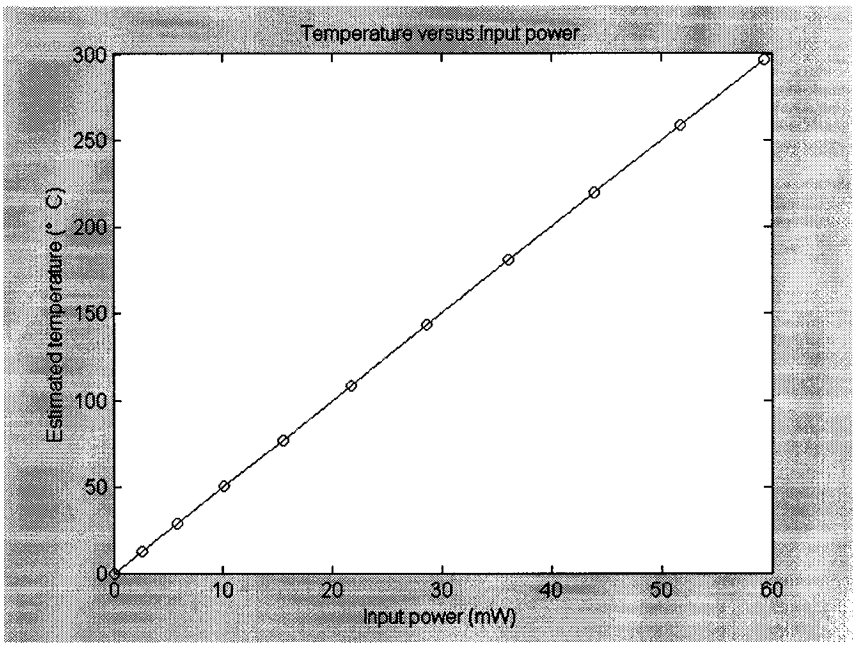

Figure 5-28. Calculated temperature versus input power base on G=5K/mW.

These estimated temperatures are quite rough. The actual temperature of the heated part of the micro-switch is expected to be significantly higher than these calculated values. The reason for this is that, in our calculation we used the average temperature for the whole structure. In actuality, only part of the resistance lies on the hottest part of the structure. The temperature for most of the remaining is lower.

Then three experiments were carried out to investigate the phenomenon that the irreversible polysilicon resistance variations when temperature is raised and lowered.

5.6.1 Experiment 1

The first experiment is carried out in two steps:

(1) In first step, the device #1 is heated up by input power. The variable resistance of the device is recorded by computing the voltage and current across the device and this step is called "R-up". But the input power has to be kept far below the value which the bright glowing zone can be seen.

(2) Then, the input power is decreased step by step and the resistance is computed again at each point. This step is called "R-down".

In this experiment, No significant differences between "R-up" curves and "R-down" curves can be found, as shown in Figure 5-29. The calculated temperature curves of heating and cooling cycle with applied power at low temperature range are very close (Figure 5-30). It is reasonable that if the elevated temperature of heating cycle is far below the "Critical" temperature as mentioned in Section 5.5, the material properties of polysilicon would not change.

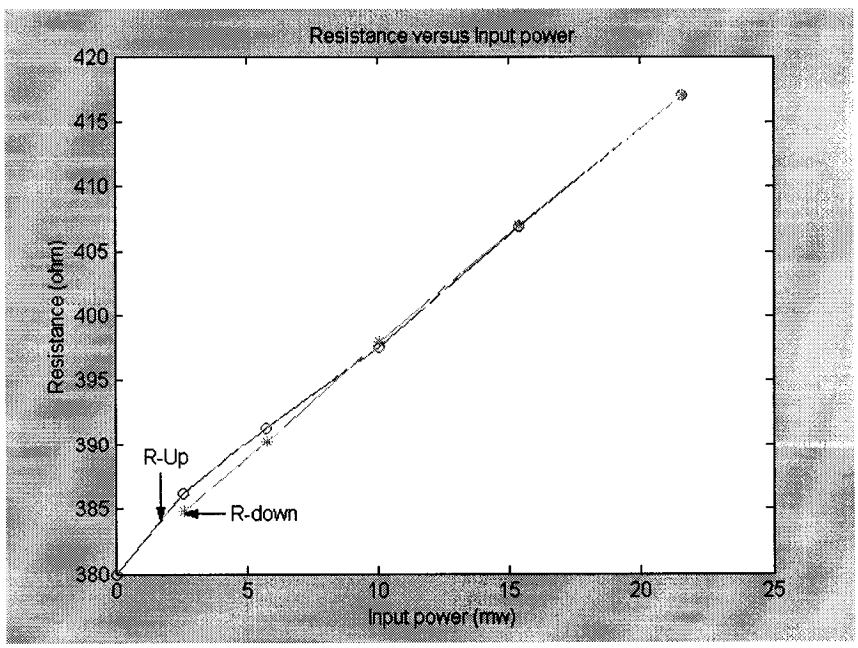

Figure 5-29. Experimental data of resistance versus input power at Experiment 1.

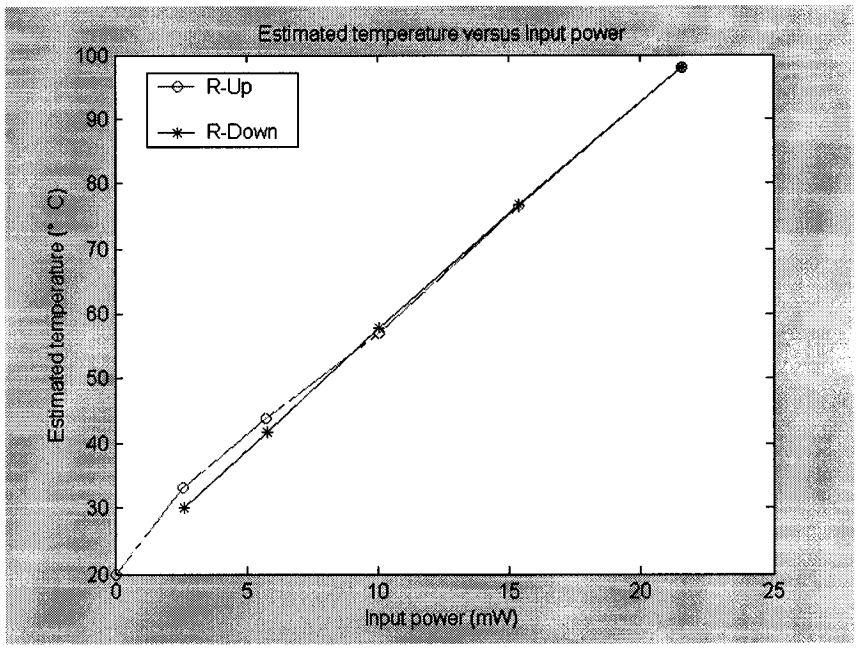

Figure 5-30. Calculated temperatures of heating/cooling cycle versus applied power at experiment 1 based on G=5k/mW.

5.6.2 Experiment 2

The second experiment is divided into three steps:

(1) First, the device #2 is heated up by input power until the glowing, hot zone appears in narrow beam. The variable resistance of the device is recorded by computing the voltage and current across the device.

(2) After seeing the bright, glowing zone, the input power is again decreased step by step from the high value, and resistance of the device is computed again during each recording point.

(3) Then the input power is increased again. The last step is called " R-up-again".

Figure 5-31 shows the resistance behavior during the sessions of temperature heating up, cooling down and heating up again. It is observed that when the temperature is heated up to a "critical" value and then cooled down, the resistances of devices demonstrate different values along the "R-up" and "R-down" curves. It provides a phenomenological trend for polysilicon resistivity while being heated up and cooled down required further investigation. After first cooling, when temperature is heated up again, the "R-up-again" and "R-down" values are almost same according to our observation. The phenomenon observed in above figure is that: Polysilicon resistivity (resistance) has difference values before and after being heated to a "CRITICAL" value (as R-Up and R-Down curves in Figure 5-31). The "critical" temperature here is the temperature when a bright, glowing zone appears in the narrow beam, same as mentioned previously in Section 5.5. It is noticed from Figure 5-31 that when the polysilicon is heated above a threshold temperature, and cooled down stepwise, the resistances of the polysilicon for the first heating and first cooling cycle have significant difference. But after the first heating /cooling cycle, and when polysilicon is heated again, the resistances values of the second heating cycle is almost the same as that of the cooling cycle. It implies that the polysilicon material property has been changed during the first heating cycle.

In order to further investigate and verify the resistance behaviors at high temperature, experiment 3 was carried out.

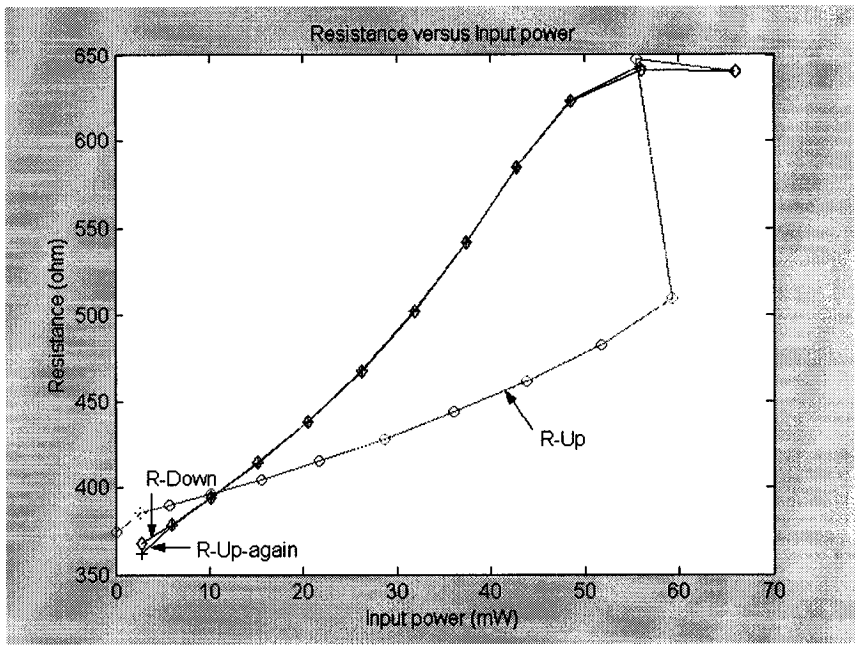

Figure 5-31. Experimental data of resistance with input power at Experiment 2.

5.6.3 Experiment 3

There are four steps in experiment 3.

(1) First, The device used in experiment 3 is heated up until the bright, glowing zone can be seen at narrow beam.

(2) And then cooled down by decreasing the input power.

(3) Reheated the device by increasing the input power.

(4) And cooled down again by decreasing the input power.

These resistance curves are demonstrated in Figure 5-32. The results are similar to that of experiment 2: only initial resistance curve of "R-up" is different from other three resistance curves. It implies that the first heating cycle is reason that causes the significant material properties change in polysilicon, such as resistance.

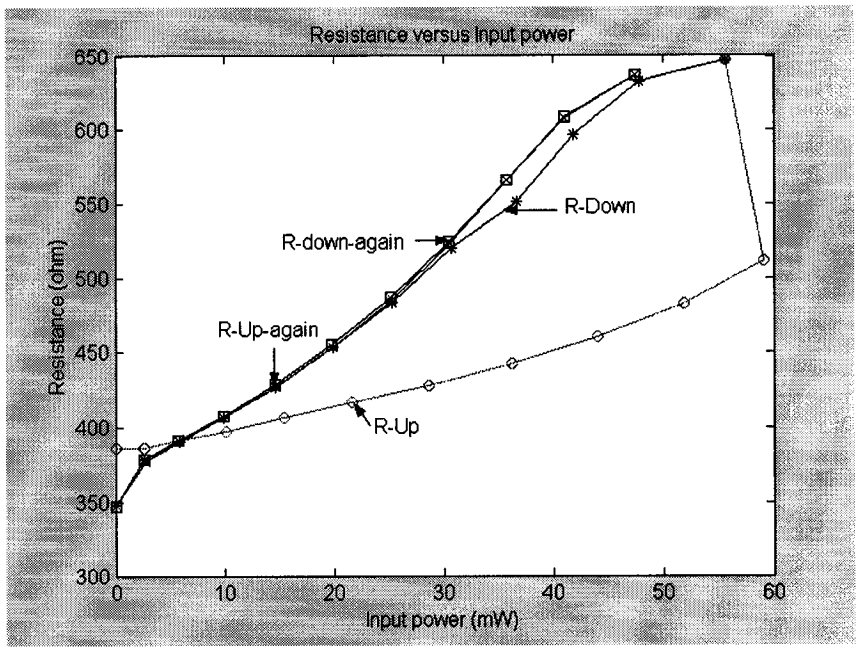

Figure 5-32. Experimental data of resistance versus input power at Experiment 3.

5.6.4 Discussions

In these three experiments, the resistance of polysilicon phenomena have been demonstrated and recorded experimentally. Based on the above experiments, we can get the experimental conclusions.

(1) In low temperature range, the variations of polysilicon resistance versus input power (temperature) remain the same during the heating/cooling cycles.

(2) At high temperature (especially when device became brightly glowing), the variations of resistance versus input power (temperature) will have significant change after the first heating cycles.

(3) Once the device experienced the high temperature, the resistance curves are relatively unchanged for subsequent heating/cooling cycles.

The temperature dependent resistivity of polysilicon related phenomena have been studied in [11,26,43]. The mechanisms of these phenomena will require further investigation. When the temperature is above a threshold value, the localized melting and drastic material properties change could happen. The possible mechanism may be similar as the thermal conductivity properties of polysilicon layers. The thermal conductivities of polysilicon layers depend on the deposition process, the grain size, shape, and distribution, and concentration and type of dopant atoms [44]. For electro-thermal micro devices, the heat treatment of polycrystalline silicon films causes changes in microstructure, in particular, the grain structure. The Joule heating generates the heat treatment and recrystallization for polysilicon layers, may change the grain size and structure grain boundaries. Localized melting and regrowth can affect recrystallization. In recrystallization of polysilicon structures, a number of the foregoing driving forces, nucleation processes and growth mechanisms may be operative simultaneously. As the temperature of device is raised to somewhat higher temperature (850 °C or above), grain boundary mobility becomes high enough for some grain boundary motion to occur. At still higher temperatures (950 °C and above), a few grains may grow to a much greater size, eventually consumes all the others [45]. This polysilicon grain size and grain boundary change mechanism may explain the phenomena of polysilicon resistance behavior after being raised at temperature.

Chapter 6

Conclusions, Contributions and Future Work

6.1 Conclusions

The designs for the MEMS-based optical switches structures have been demonstrated in this thesis. Several new electro-thermally actuated micro-switches designs have been documented in Chapter 3. These uni-directional switches were designed and fabricated for two different processes: CMOS-compatible bulk micromachining and MUMPs surface micromachining. Also in this chapter, a novel bi-directional switch was designed for CMOS-compatible bulk micromachining and simulated with ANSYS tool to obtain the simplified device performances. In Chapter 4, in order to release the devices fabricated by CMOS technology in anisotropic wet-etching process successfully, post-etching experiments with Al metal pad layer protection were studied. Chapter 5 includes the experimental measurements for devices. And some interesting phenomena, such as back bending and polysilicon resistance behaviors at high temperature, were observed and studied during this chapter. At last, a novel electrostatic switch combined both comb-drive structure and parallel plate was also presented in Appendix B.

The traditional and well-known uni-directional deflection thermal actuator has been well documented in many previous published works. In this work, the FEM analysis for device performances and analytical solution of the uni-directional thermally actuated micro-switches were carried out. Some devices with new designs were studied to improve the actuators performances. And a novel bi-directional switch, which takes advantages of CMOS technology features, was presented here. According to the best knowledge of the author, the designs of horizontal bi-directional thermally actuated

switches are reported first here. In these designs, the silicon dioxide layer from standard CMOS process is served as structural layer, and polysilicon heating elements were embedded in the structural layer. At any given time, with IC control circuit fabricated in the CMOS process, only one narrow structural beam is heated by polysilicon, and causes the whole structure to deflect to the unheated beam direction.

Displacements of the uni-directional devices and bi-directional devices were tested with probe station and micromanipulators. During these experiments, we also found some interesting phenomena: back buckling and polysilicon resistance variation while heating up and cooling down the devices. These phenomena were further studied in this work to investigate the reasons. This fundamental study about polysilicon material properties at high temperature provides a reference and guidance for design and operation of these thermally actuated polysilicon devices.

6.2 Contributions:

The contributions of this thesis work are summarized as follows:

(1) The novel designs for electro-thermally actuated U-shape folded beam micro-switch:

While the U-shape folded beam electro-thermal actuator has been well known for several years, the operating principle of this thermally driven actuator based on the asymmetrical thermal expansion of a microstructure with variable cross sections is not new, several new designs have been presented in this thesis, including:

- Design using serpentine spring as flexure beam. It offers the possibility to change the flexure beam spring constant and improve the displacement performance.

- Design with different thickness of narrow beam and wide beam for MUMPs technology (POLY2 layer for narrow beam and POLY1+POLY2 layer for wide beam). This effort is to maximize the cross-section difference between narrow beam and wide beam, therefore improve the displacement by increasing the asymmetrical thermal expansion of wide beam and narrow beam.

(2) New design of the in-plane bi-directional electro-thermally actuated micro-switches:

This novel micro-switch, which offers the possibility of lateral displacement in two directions, was designed for CMOS-compatible bulk micromachining. The novel bi-directional micro-switch takes advantage of the unique features of CMOS process. The silicon dioxide layer is used as structural layer, and the embedded polysilicon layer is used as a heating element. Moreover, during the wet-etching process, the silicon dioxide layer also serves as a mask layer to protect the polysilicon layer from being etched by TMAH. This type of CMOS-compatible bulk micromachining provides a low cost monolithic solution for the integration of this micro-switch and control circuits.

(3) Electro-thermally actuated micro-switches were fabricated by CMOS-compatible micromachining and tested:

The uni-directional and bi-directional micro-switch prototypes were fabricated by commercial CMOS technology. Wet post-etching process was carried out in our Lab with pad passivation effort. And the micro devices were able to demonstrate the displacements and to be bonded in packages.

(4) New design for electrostatic micro-switch combined the comb-drive and parallel plates:

A new micro-switch design, which combines two electrostatic mechanisms (parallel plates and comb drive structures) together, was presented in Appendix B. An analytical model was used to simulate the static displacements of the design with parallel plates and displacements of design without parallel plates, and show the displacement difference.

(5) The back-bending phenomenon and polysilicon fault mechanism were studied:

Back-bending phenomenon from micro-switches fabricated by MUMPs process was observed at high temperature. The beams changed from elastic buckling to plastic bucking. And polysilicon devices fault mechanism at high temperature was studied here.

(6) The effect of elevated temperature on polysilicon resistance was studied by increasing and decreasing the input heating power stepwise:

The polysilicon resistance property was studied by a number of heating/cooling cycles. At high temperature (especially when device became brightly glowing) the variations of resistance versus input power (temperature) will have significant change after the first heating cycles. But once the device experienced the high temperature, the resistance curves are relatively unchanged for subsequent heating/cooling cycles.

(7) Publications related to this work:

- Li, Jun. Kahrizi, M. Landsberger, L.M., "Design, Fabrication and Characterization of CMOS-compatible Optical Microswitches," IEEE Canadian Conference on Electrical and Computer Engineering, CCECE 2003, May 4-7 2003, Montreal, Canada

- Li, Jun. Kahrizi, M. Landsberger, L.M., "In-plane Electro-thermally actuated Optical Switches," Technical Digest of SPIE at Opto-Canada, Ottawa, Canada, May 9-10, 2002.pp. 482-484.

6.3 Future Work

The work presented in this thesis can be subject to further study and analysis.

- Some new electro-thermally actuated micro-switches (Design using serpentine spring as flexure beam and Design with different thickness of narrow beam and wide beam) and switching time can be further analyzed by simulation tool.
- The post-etch process for MUMPs process can be carefully studied in order to avoid the stiction and successfully release device with specific design.
- For longer etching times Al pad layer passivation experiments, the depletion effects of the TMAH and oxidizer from the solution have to be considered. The amount of new adding TMAH is a very important. It has to be chosen at a "balance" amount which can passivate the Al and keep reasonable silicon etch rate. It can be the future work of post-processing for the Al passivation experiments.
- In order to achieve the displacement as we expect from simulation in electrostatic micro-switch, For fabrication consideration, high aspect ratio fabrication technique will be suitable these in-plane motion electrostatic devices.

Appendix A

Introduction for Structural Analysis

The force or flexibility method is one of the several techniques available to analyze indeterminate structures [46]. In order to illustrate this technique, a frame in Figure A-1 is used here as an example. The following procedures describe the concept of this method for analyzing externally indeterminate structures.

- Determine the degree of indeterminacy

Determine the degree of indeterminacy of a given structure. This can be accomplished by calculating the number of unknown reactions, r, minus the number of static equilibrium equations, e. For example, considering the frame shown in Figure A-1, the number of unknown external reactions, r, equals 5, (X_A, Y_A, M_A, X_B, and Y_B). The number of static equilibrium equations, e, equals 3, ($\Sigma F_x = 0$, $\Sigma F_y = 0$ and $\Sigma M = 0$). Therefore, the number of degree of indeterminacy, n, is calculated as:

$n = r - e = 5 - 3 = 2$

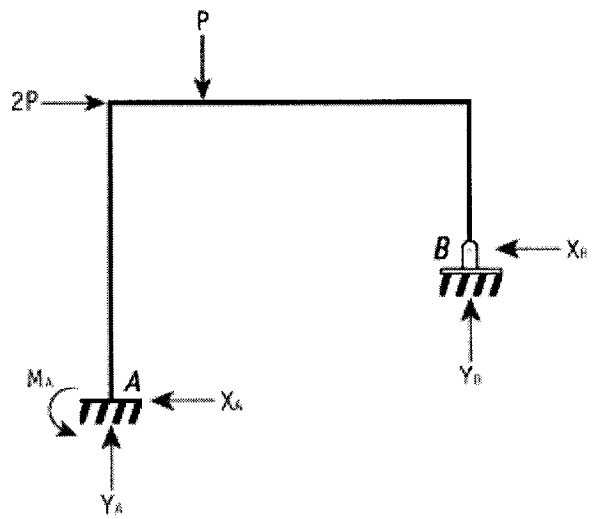

Figure A-1 - Indeterminate frame structure.

- Select redundants

Select a number of the support reactions equal to the degree of indeterminacy as redundants. The choice of the redundants will vary since any of the unknown reactions can be utilized as a redundant. In the example shown in Figure A-1, one choice is to select the X reaction at B and the moment at A as redundants.

- Remove restraints at the redundants

Remove the support reactions (restraints) corresponding to the selected redundants from the indeterminate structure to obtain a primary determinate structure, or sometimes referred to as a released structure. This determinate system must represent a stable and admissible system.

- Sketch deflected shape

Sketch the deflected shape of the primary determinate structure under the applied loads, and label the deformations at the removed restraints, (see Figure A-2).

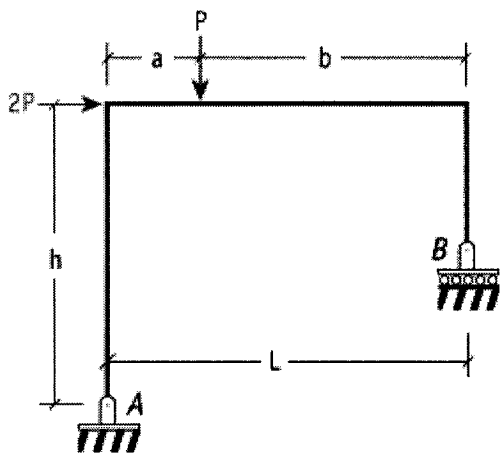

Figure A-2(a) - Primary structure.

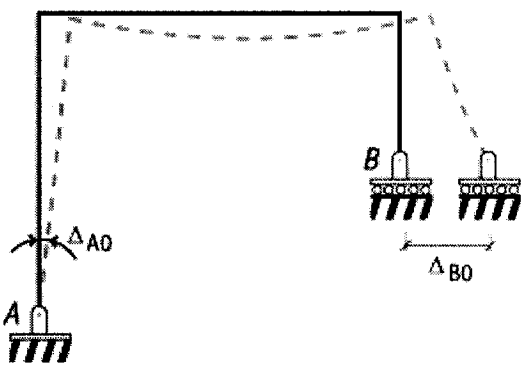

Figure A-2(b) - Primary structure deflected shape.

- Calculate deformations at redundants

Calculate the deformations corresponding to the redundants, i.e., the rotation at Support A, Δ_{A0}, and the translation, Δ_{B0}, at Support B. This can be accomplished as follows; using the virtual work method,

(a) Draw the moment diagram, M_0, for the primary structure under the applied loads, (see Fig. A-3(a)(i)). The method of superposition can also be utilized when drawing the M_0 diagram, (see Fig. A-3(a)(ii)). This will simplify the integration needed to calculate the deformation Δ_{A0} and Δ_{B0}.

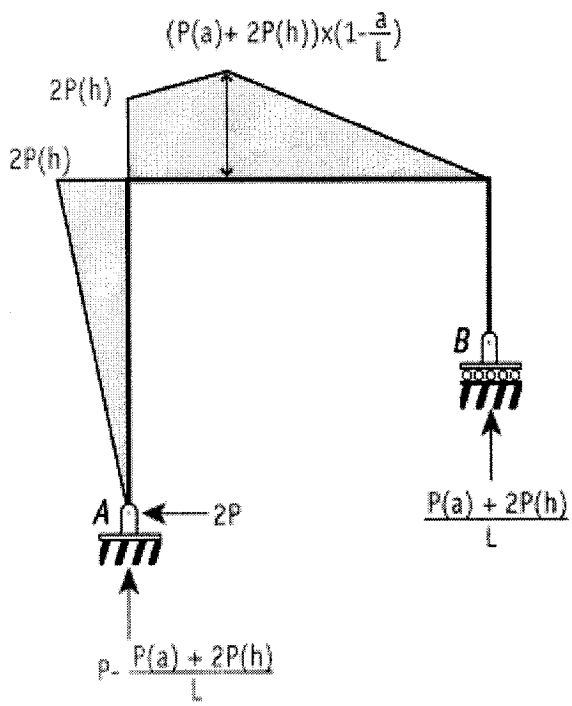

Figure A-3(a)(i) - Moment diagram of primary structure.

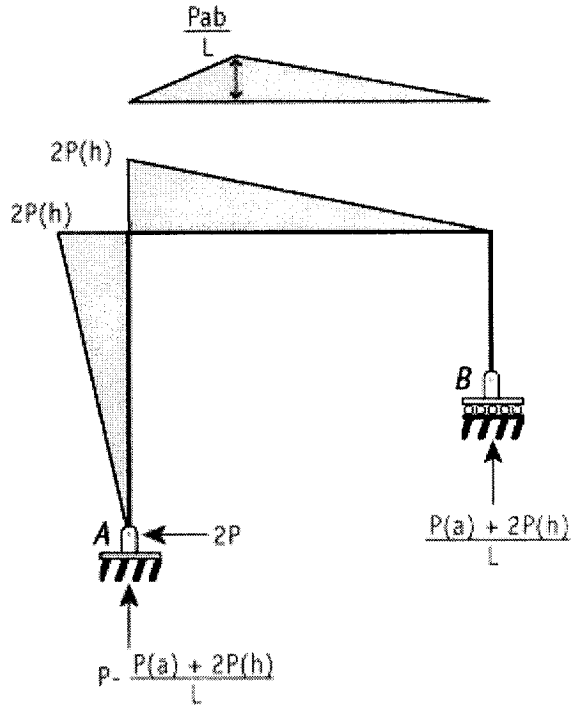

Figure A-3(a)(ii) - Moment diagram by superposition.

(b) Apply a unit load at the location of the first redundant. In this case, apply a unit moment, M_A = 1 ft-k at Support A. Sketch the deflected shape, label the deformation at

the removed restraints and draw the moment diagram of the primary structure when subjected to this load, see Fig. A-3(b).

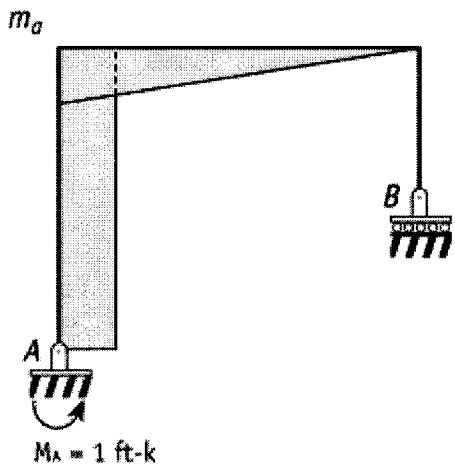

Figure A-3(b)(i) - Moment diagram with M_A = 1 ft-k.

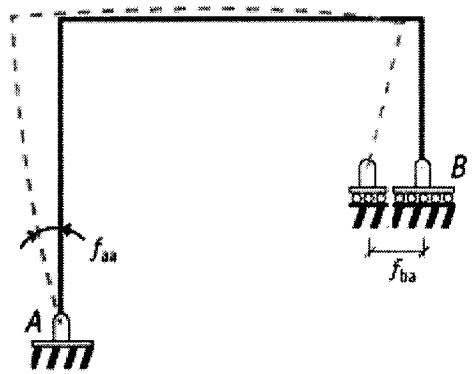

Figure A-3(b)(ii) - Deflected shape with M_A = 1 ft-k.

(c) Calculate the rotation, Δ_{A0}, at Support A using the following equation:

$$\Delta_{A0} = \int_l \frac{M_0 m_a}{EI} dx$$

(d) Apply a unit load at the location of the next redundant. i.e., apply a unit force, X_B = 1 k at Support B. Sketch the deflected shape, label the deformation at the removed restraints and draw the moment diagram of the primary structure when subjected to this load, see Fig. A-3(c).

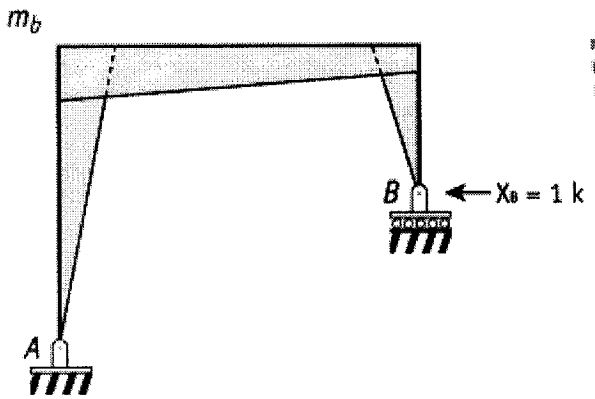

Figure A-3(c)(i) - Moment diagram with X_B = 1k.

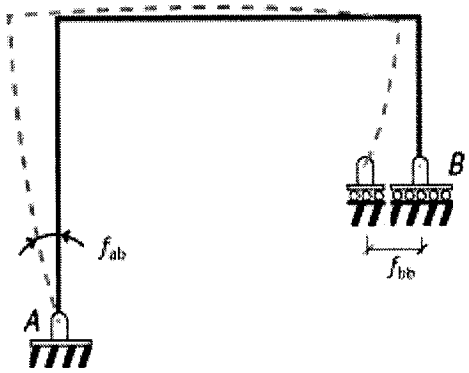

Figure A-3(c)(ii) - Deflected shape with X_B = 1k.

(e) Calculate the translation, Δ_{B0}, at Support B using the following equation:

$$\Delta_{B0} = \int_l \frac{M_0 m_b}{EI} dx$$

(f) Calculate the deformations of the primary structure when subjected to the redundant M_A, see Fig. A-3(b), or the redundant X_B, see Fig A-3(c). This is accomplished by using the following relationships:

$$f_{aa} = \int_l \frac{m_a m_a}{EI} dx$$

$$f_{ab} = f_{ba} = \int_l \frac{m_a m_b}{EI} dx$$

$$f_{bb} = \int_l \frac{m_b m_b}{EI} dx$$

The above relationships yield the flexibility coefficients f_{aa}, f_{ab}, f_{ba}, and f_{bb}. The flexibility coefficient fij is defined as the deformation corresponding to the redundant i, due to a unit value of the redundant j.

- Write consistent deformation equations

Write consistent deformation equations that correspond to each redundant. In this case:

(a) Rotation at Support A = 0 since Support A is a fixed support that prevents rotations.

$$\Delta_{A0} + f_{aa}M_A + f_{ab}X_B = 0 \qquad (1)$$

(b) Translation at Support B = 0 since Support B does not allow horizontal translation.

$$\Delta_{B0} + f_{ba}M_A + f_{bb}X_B = 0 \qquad (2)$$

- Solve deformation equations

Solve Equations (1) and (2) in the previous step to obtain the unknown redundants M_A and X_B. Notice that if the answers of M_A and X_B are positive, this means that the assumed directions of the applied force in Figures A-3(b) and A-3(c) are correct.

- Determine support reactions

Determine the remaining support reactions, i.e., X_A, Y_A, and Y_B of the indeterminate structure by imposing the calculated values of M_A and X_B in the correct directions and utilizing the three equilibrium equations, ($\Sigma F_x = 0$, $\Sigma F_y = 0$ and $\Sigma M = 0$).

Once all reactions have been evaluated, the axial, shear, and moments diagrams can be drawn. With this information, an approximate deflected shape can also be sketched.

Appendix B

Electrostatic Micro-Switches

B.1 Micro-Switch Design

Electrostatic actuation operation principles normally consist of two categories as illustrated in Figure B-1:

1) Electrostatic force prompts the relative motion of the plates in normal direction of aligned plates (The electrostatic force is created by parallel plates as given in Figure B-1(a)).
2) Electrostatic force prompts the parallel movement for misaligned plates (electrostatic force is created by comb drive structures as given in Figure B-1 (b)).

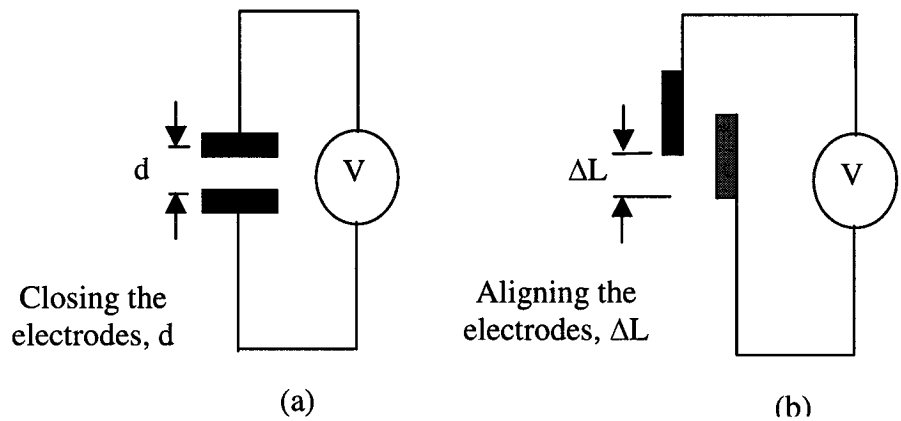

Figure B-1. (a) Normal direction of aligned plates, (b) Parallel movement for misaligned plates.

For the standard comb drive actuator (Figure B-2), electrostatic force prompts the movement parallel to the interdigitated finger structures (X-direction). Comb drive actuator consists of two interdigitated finger structures, where one comb is fixed and the other is connected to a compliant suspension. Applying a voltage difference between the comb structures will result in a deflection of the movable comb structure by electrostatic

forces. Voltage controlled comb-drive actuators exert a lateral electrostatic force which is independent of position making them attractive for many applications including optical shutters [47–49], optical switches [50-51].

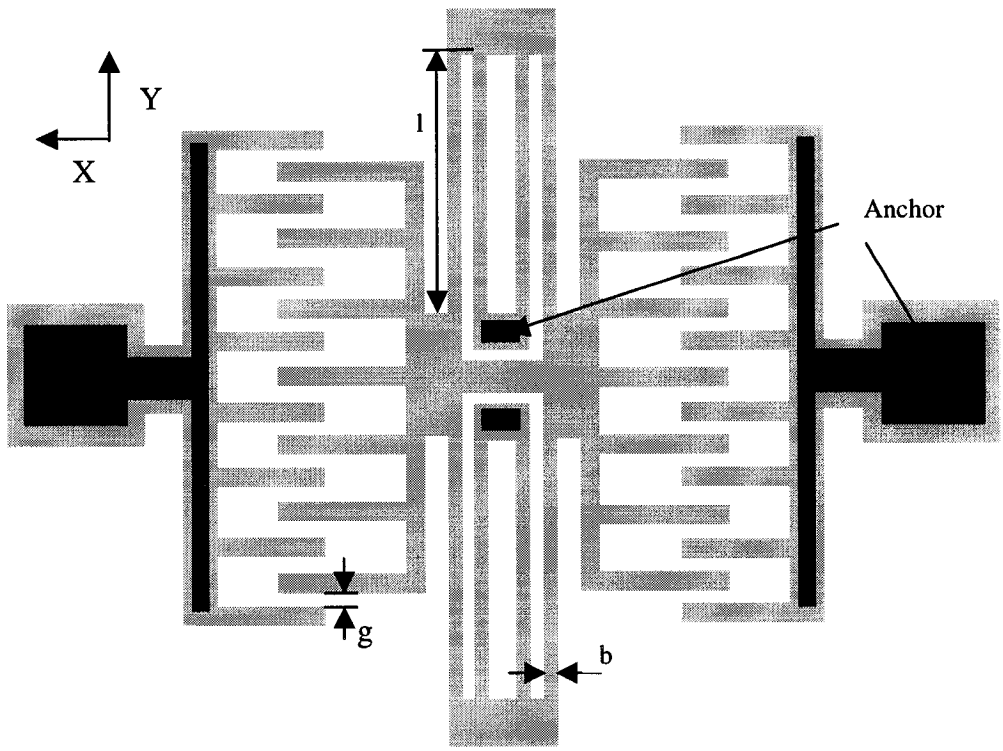

Figure B-2. Schematic view of comb drive structure.

Based on the study of two kinds of electrostatic actuation mechanism, a new micro-switch design (Figure B-3), which combines two electrostatic mechanisms (parallel plates and comb drive structures) together, has been developed. And cantilever beam is chosen as suspension beam instead of the most commonly used the folded-beam flexure in standard comb drive actuators. Here, we assume the parameters of geometry in Figure B-2 and Figure B-3 are same except for difference in the cantilever beam and folded-beam flexure.

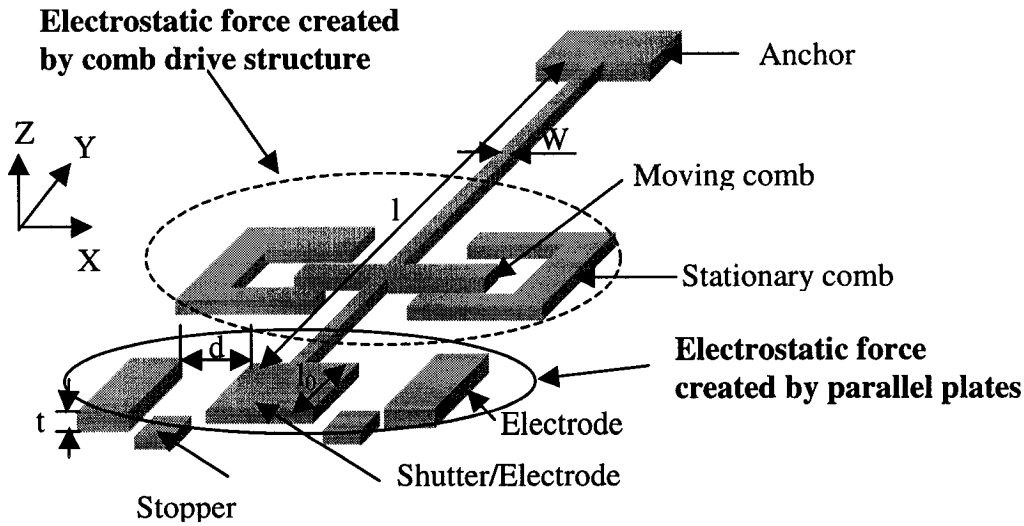

Figure B-3.Schematic diagram of in-plane micro-switch based on electrostatic mechanism.

For the interdigitated finger structures in this design, when a driving voltage, V, is applied between the movable and fixed fingers of comb drive structure, the equations to compute the electrostatic force F_x along the x-direction is the same as that of the standard comb drive structure in Figure B-2 except the spring constant K_x. Here, K_x is the spring constant of the compliant suspension cantilever beam in the x-direction.

$$F_X = \frac{n\varepsilon t}{g} V^2 \tag{B.1}$$

$$\delta_x = \frac{n\varepsilon t}{gK_x} V^2 \tag{B.2}$$

For the parallel plates in this design, when the driving voltage, V, is applied between shutter and electrodes, the electrostatic force created parallel charged plates is:

$$F_d = \frac{1}{2}\frac{\varepsilon t l_0}{d} V^2 \tag{B.3}$$

The spring constant K_x of the cantilever beam in the x-direction is:

$$K_x = \frac{3EI}{l^3} \tag{B.4}$$

where E is Young's modulus, The moment of inertia for rectangle cross-section is given by

$$I = \frac{wt^3}{12} \tag{B.5}$$

where w is cantilever beam width, t is thickness of the structure, Therefore,

$$K_x = \frac{Ewt^3}{4l^3} \tag{B.6}$$

Compared our microswitch design with normal comb drive devices, the spring constant for our design is $K = \frac{Ewt^3}{4l^3}$ and spring constant for normal comb drive is $k_x = 2Etb^3 / l^3$ (b is beam width of folded-beam flexure).

Figure B-4 is the new electrostatic micro-switch fabricated by MUMPs technology.

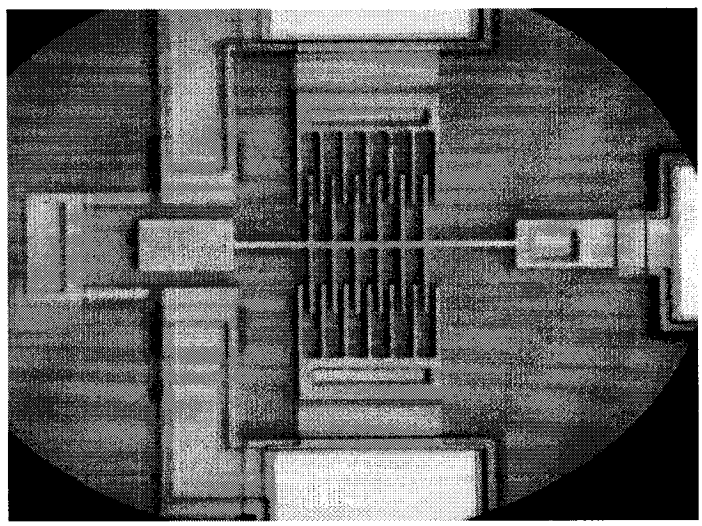

Figure B-4.Micro-switch fabricated by MUMPs technology.

Analytical models have been developed to simulate the static displacements of the design with parallel plates and design without parallel plates (Figure B-5). The simulation results are given in Table B.1 and Table B.2.

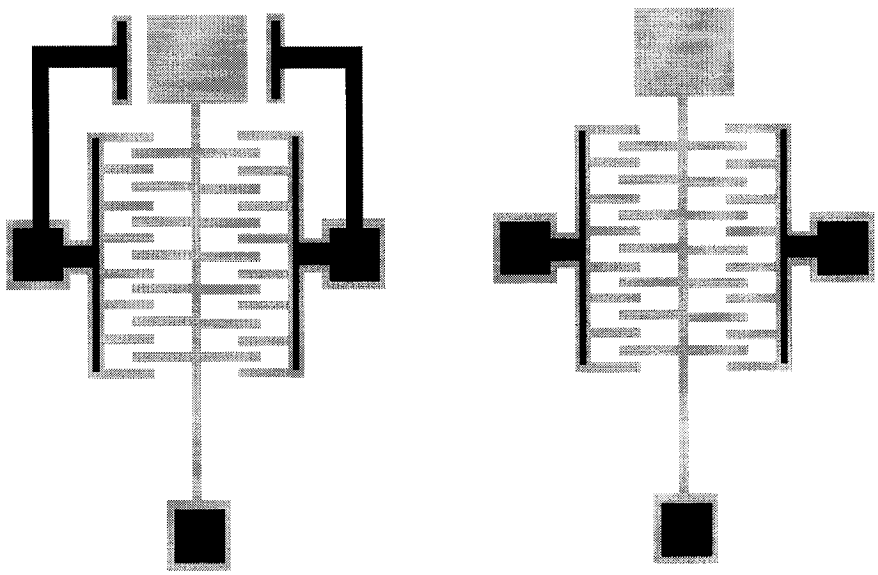

(a) (b)

Figure B-5.(a) Structure design with parallel plates, (b) Structure design without parallel plates.

Table B.1 The simulated data from device with parallel plates

Voltage (V)	Displacement (μm)	Force (Newton)
25	0.2618	3.3187e-008
40	0.6703	8.4960e-008
60	1.5082	1.9116e-007
80	2.6812	3.3984e-007
90	3.3934	4.3011e-007
120	6.0327	7.6464e-007

Table B.2 The simulated data of device without parallel plates

Voltage (V)	Displacement (μm)	Force (Newton)
25	0.0078	9.8333e-10
40	0.0199	2.5173e-9
60	0.0447	5.6640e-9
80	0.0794	1.0069e-8
90	0.1005	1.2744e-8
120	0.1787	2.2656e-8

The design (combined with comb drive structure and parallel plates) demonstrated relatively bigger displacement than the design with only comb drive structure.

B.2 Experimental Measurements

As we have introduced in chapter 2 for MUMPs® technology process: After the final, unreleased structure is finished, the wafer are diced, shipped to the users for sacrificial release and test. The release is performed by immersing the chip in a bath of 49% HF (room temperature) for 1.5-2 minutes. This is followed by several minutes in DI water and then alcohol to reduce stiction followed by at least 10 minutes in an oven at 110°C.

However, after etching the sacrificial oxide layer in Lab, we observed that the fixed electrodes and shutter blade are not in the same plane. The movable cantilever beams are lower than fixed electrodes. The residual stress after releasing the sacrificial oxide layer and weight of whole structure itself may causes this problem.

Two devices using only parallel plates fabricated by POLY1 layer in Figure B-6 are presented to investigate the effect.

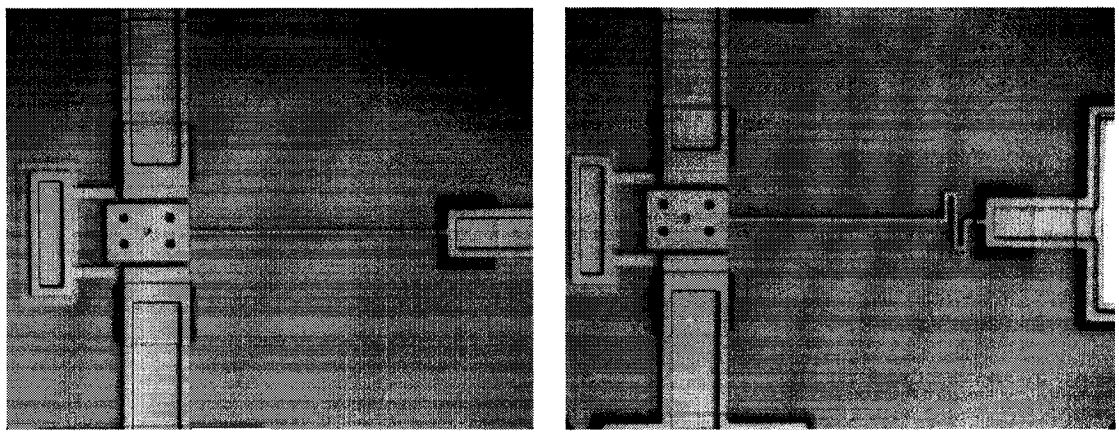

(a) (b)

Figure B-6. (a) Design of conventional cantilever beam with normal direction of aligned plates, (b) Design of spring cantilever beam with normal direction of aligned plates.

The vertical difference between the fixed electrodes and movable cantilever beams of these two designs are given in Table B.3.

Table B.3 Vertical distance between fixed electrodes plane and movable cantilever beams

Design of conventional cantilever beam	Design of spring cantilever beam
Cantilever beam lower than fixed electrodes by 0.8 μm	Cantilever beam lower than fixed electrodes by 0.1-0.2 μm

The static behaviors of electrostatic actuated micro-switches were tested by probe station in our Lab. First, the standard comb-drive resonator in Figure B-7 was tested. When 90 volts is applied between the stationary fingers and movable fingers, the static displacement can be seen about 6 μm.

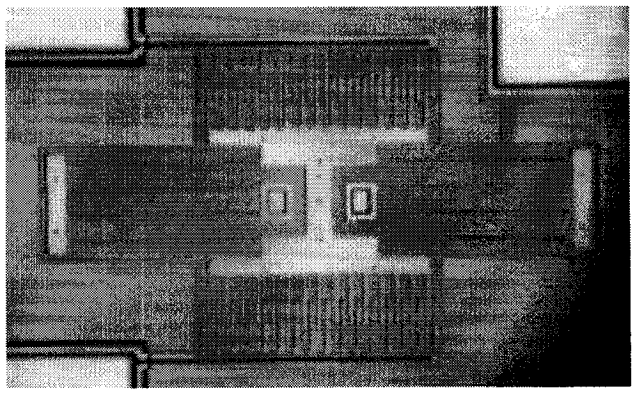

Figure B-7. Micrograph of standard comb drive structure.

Then, the comb-drive based micro-switch in Figure B-4 was tested on the probe station. The displacements of this device are only about 1μm at 120 volts input voltage at the electrodes. The experiment results are much smaller than that of the simulation values. The possible reason is same as that of the devices of the micro-switches based on parallel plate. The Figure B-8 maybe visually illustrates the reasons.

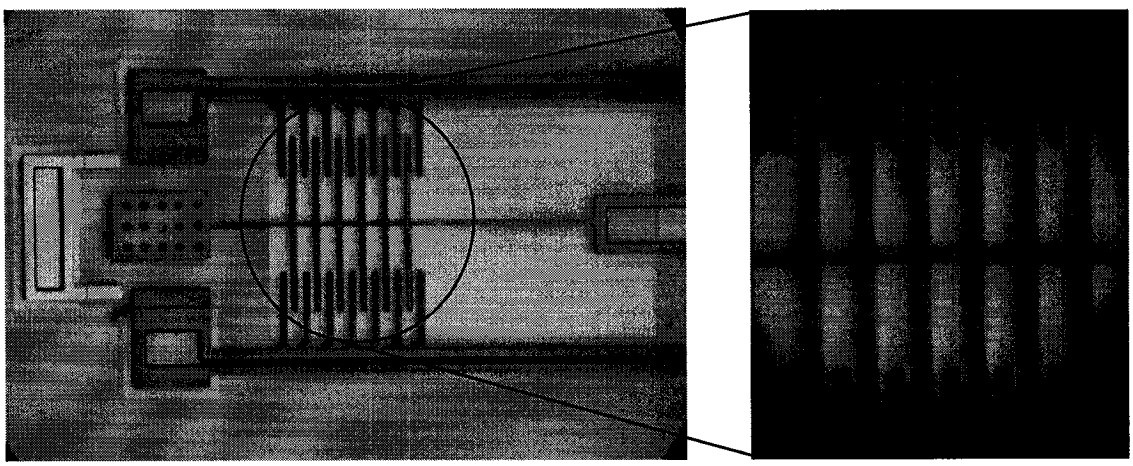

Figure B-8. Comb-drive based micro-switch and its magnification micrograph.

From magnification view of picture, we can see that the stationary set of comb fingers and the movable set of fingers are not in the same horizontal plane. The movable fingers

are lower than the fixed fingers about 1.5 μm. So the electrostatic force generated by each engaged pair of fingers is much smaller than that of which we expected from analysis. The comb-drive structure device is very sensitive to fingers misalignment and thickness of fingers pairs. Hence, it will only allow a very small displacement.

Reference:

[1] K. E. Peterson, "Silicon as a mechanical material," Proceedings of IEEE, 70, pp. 420-457, 1982.

[2] R. T. Howe and R. S. Muller, "Polycrystalline silicon micromechanical beams," Spring meeting of the electrochemical society, Montreal, Canada, Extended abstracts 82-1. May 9-14, 1982.

[3] R. T. Howe and R. S. Muller, "Resonant microbridge vapor sensor," IEEE Transactions on Electron Devices, Vol. 33, pp. 499—507. 1986.

[4] Richard S. Muller, "MEMS: Quo vadis in century xxi?," Microelectronic engineering, Vol. 53, pp.47—54, 2000.

[5] G. Perregaux et al. "High-speed micro-electromechanical light modulation arrays," Transducers 97 Digest of Technical Papers, Chicago, Vol. 1, pp.71-74, June 16-19, 1997.

[6] Robert Anderson J. Jason Yao, Sang Tae Park and Je.rey DeNatale, "A low power/low voltage electrostatic actuator for RF MEMS application," Solid-state sensor and actuator workshop Hilton Head Island, SC, pp. 246—249, 2000.

[7] S.P. Timoshenko and J.N. Goodier, *Theory of elasticity*, McGraw-Hill, New York, 2nd edition, 1951.

[8] John H. Comtois and Victor M. Bright, "Applications for surface-micromachined polysilicon thermal actuators and arrays," Sensors and actuators, A. Vol. 58, pp. 19-25, 1997.

[9] B Romanowicz Ph Lerch, C Kara Slimane and Ph Renaud, "Modelization and characterization of asymmetrical thermal micro-actuators," Journal of Micromechanics and Microengineering, Vol. 6, pp. 134-137, 1996.

[10] Qing-An Huang and Neville Ka Shek Lee, "Analytical modeling and optimazation for a laterally-driven polysilicon," Microsystems Technologies, Vol. 5, pp.133-137, 1999.

[11] Jun Li and G.K. Ananthasuresh, "Microfabrication and Characterization of Electro-Thermal-Compliant Micro Devices," Proceedings of the 2000 ASME Design Technical Conferences, Baltimore, MD, Sep.10-13, 2000.

[12] Chi Shiang Pan and Wensyang Hsu, "An electro-thermally and laterally driven polysilicon microactuator," Journal of Micromechanics and Microengineering, Vol. 7, pp.7-13, 1997.

[13] Qing-An Huang and Neville Ka Shek Lee, "Analysis and design of polysilicon thermal flexure actuator," Journal of Micromechanics and Microengineering, Vol. 9, pp.64-70, 1999.

[14] Tze-Wei Yeow, K. L. Eddie Law, and Andrew Goldenberg, "MEMS Optical Switches," IEEE Communications Magazine, pp.158-163. November, 2001.

[15] Jun Li and G. K. Ananthasuresh, "A Quality study on the excimer laser micromachining of Electro-Thermal-Compliant micro devices," Journal of Micromechanics and Microengineering, Vol.11, pp. 38-47, 2001.

[16] V. A. Aksyuk et al., "Lucent microstar micromirror array technology for large optical crossconnects," Proceedings of. SPIE, Vol. 4178, 2000.

[17] R.A. Miller et al., "An electromagnetic MEMS 2x2 fiber optic bypass switch," 1997 International Conference on Solid-State Sensors and Actuators (TRANSDUCER '97), Chicago, IL, pp. 89-92, June 16–19, 1997.

[18] L. Latorre, Y. Bertrand, P. Hazard, F. Pressecq and P. Nouet, "Modeling and design optimization of a CMOS compatible MEMS," Technical Proceedings of the International Conference on Modeling and Simulation of Microsystems MSM 99, pp.620-623, 1999.

[19] Cronos Integrated Microsystems, A JDS Uniphase Company "MUMPs Design Handbook Revison 7.0,"

[20] S. Iyer, Y. Zhou and T. Mukherjee, "Analytical modeling of cross-axis coupling in micromechanical springs," Technical Proceedings of the International Conference on Modeling and Simulation of Microsystems MSM 99, pp.632-635, 1999.

[21] David M. Burns and Victor M. Bright, "Design and performance of a double hot arm polysilicon thermal actuator," Proceedings of SPIE, Vol. 3224, pp. 296-306, 1997.

[22] Jun Li, M. Kahrizi, L.M. Landsberger, "In-plane electrothermally actuated optical switches," Technical Digest of SPIE at Opto-Canada, Ottawa, Canada, pp. 482-484, May 9-10, 2002.

[23] Pan CS, Hsu W, "An electro-thermally and laterally driven polysilicon microactuator," Journal of Micromechanics and Microengineering, Vol.7, pp.7–13,1997.

[24] Lerch P; Slimane CK; Romanowicz B; Renaud P, "Modelization and characterization of asymmetrical thermal microactuators," Journal of Micromechanics and Microengineering, Vol.6: pp.134–137, 1996.

[25] Dong Yan, *Mechanical Design and Modeling of MEMS Thermal Actuators for RF Applications,* Master's thesis at University of waterloo, 2002

[26] Lin L and Chiao M, "Electrothermal response of lineshape microstructures," Sensors and Actuators, A 55 pp.35–41, 1996.

[27] David G. Elms, *Linear Elastic Analysis*, B. T. Batsford Ltd, London, 1970.

[28] Kennedy J B and Madugula M K S. *Elastic Analysis of Structures* (New York: Harper and Row). (1990) Chapter. 7, 9.

[29] Sergey Edward Lyshevski. *Nano-and microelectromechanical systems.* (CRC Press) 2001. Chapter.2.

[30] L. M. Landsberger, "ELEC6251 COURSE PACK," 2002.

[31] Kuntao Ye and Fred R. Beyette Jr., "Characterization of a monolithic silicon MEMS technology in standard CMOS process," SPIE Conference on Optoelectronic Information Processing, Denver CO, August 2001

[32] Erno Hilbrand Klaassen, *Micromachined instrumentation systems,* Ph.D DISSERTATION, 1996

[33] O. Tabata, "Anisotropic etching of silicon in TMAH solutions," Sensors and Materials, Vol.13, No.5, pp.271-283, 2001

[34] M. Paranjape, A. Pandy, S. Brida, L. Landsberger, M. Kahrizi, M.Zen, "a Dual-doped TMAH silicon etchant for MEMS applications," The Journal of Vacuum Science and Technology A, Vol.18. Issue 2, pp.738-742, March, 2000.

[35] T. Zhou, *CMOS cantilever microresonator,* Master's thesis at University of Alberta, 2000

[36] Ryan Hickey, Dan Sameoto, Ted Hubbard and Marek Kujath, "Time and frequency response of two-arm micromachined thermal actuators," Journal of micromechanics and microengineering, Vol.13, pp.40-46, 2003.

[37] J.W. Judy, T. Tamagawa, D.L. Polla, "Surface micromachined linear thermal microactuator," 1990 IEEE International Electron Devices Meeting, pp. 629–632, 1990.

[38] J. Ji, J. Chaney, M. Kaviany, P.L. Bergstrom, K.D. Wise, "Microactuation based on thermally driven phase-change," IEEE International Conference on Solid-State Sensors and Actuators, pp. 1037–1040, 1991.

[39] Y. Fukuta, D. Collard, T. Akiyama, E.H. Yang, H. Fujita, "Microactuated self-assembling of 3D polysilicon structures with reshaping technology," Proceedings of the 1997 IEEE 10th Annual International Workshop on MEMS, pp. 477–481, 1997.

[40] Q. Wu, K.M. Lee, C.C. Liu, "Development of chemical sensors using microfabrication and micromachining techniques," Proceedings of the Fourth International Meeting on Chemical Sensors B13 (1–3) (1993) 1–6

[41] C.L. Tsai, A.K. Henning, "Surface micromachined turbines," Proceedings of Ninth IEEE International Conference on Solid-State Sensors and Actuators, pp.829–832, 1997.

[42] Kwok Siong Teh, Liwei Lin, "Time-dependent buckling phenomena of polysilicon micro beams," Microelectronics Journal 30, pp.1169–1172, 1999.

[43] Oleg Grudin, R. Marinescu, Leslie. M. Lansberger, D. Cheeke, and Mojtaba Kahrizi, "CMOS-compatible high-temperature micro-heater: microstructure release and testing," Canadian Journal of Electrical & Computer Engineering, Vol.25 No.1, pp. 29-33, January 2000.

[44] A.D. McConnell, S. Uma, and K.E. Goodson, "Thermal conductivity of doped polysilicon layers," Journal of Microelectromechanical Systems, Vol.10, pp.360-369, 2001

[45] C.Hill and S. Jones, "Recrystallization of Poly-Si," January 1988 EMIS Datareview RN=17892

[46] Fouad Fanous, *Introductory problems in structural analysis online notes* for Structural Analysis-I Course, 2000.

[47] Jaecklin V P, Linder C, de Rooij N F, Moret J M and Vuilleumier R, "Optical microshutters and torsional micromirrors for light modulator arrays," Proceedings of IEEE Micro Electro Mechanical System. Fort Lauderdale, FL, pp. 124–131, 1993.

[48] Tabata O, Asahi N, Fujitsuka N, Kimura M and Sugiyama S, "Electrostatic driven optical chopper using SOI," Proc. 7th Conf. Solid-State Sensors and actuators, Transducers '93, Yokohama, Japan, pp. 124–131, 1993.

[49] Chen P Y and Muller R S, "Microchopper-modulated IR microlamp," Proceedings of IEEE Solid-State Sensor and Actuators Workshop, Hilton Head Island, SC, pp.239-242, 1994.

[50] J.D. Grade, H. Jerman, and T.W. Kenny, "A large-deflection electrostatic actuator for optical switching applications," Technical Digest 2000, Solid State Sensor and Actuator Workshop, Hilton Head, SC, pp. 97-100, June 2000.

[51] W.J. Wang and R.M. Lin, "Simulation and realization of free space optical switch architecture based on MEMS vertical mirrors," Technical Proceedings of the International Conference on Modeling and Simulation of Microsystems NanoTech 2002 - MSM 2002 pp.226 – 229, 2002.